Elastic J/ψ Photoproduction and the Detection and Triggering of Muons at Low $W_{\gamma p}$ using the H1 Detector

Kirstee Louise Hewitt

Thesis submitted for the degree of
Doctor of Philosophy

School of Physics and Space Research
Faculty of Science
University of Birmingham

March 1998

Synopsis

The electron-proton colliding beam facility HERA consists of two independent accelerators designed to store 820 GeV protons and 27.5 GeV electrons. The two beams circulate in opposite directions in an underground tunnel, 6.3 km in length. At two interaction points the beams are collided head on and some of the highest energy ep collisions ever attained are observed. The H1 detector is situated at one of these interaction points and observes the reaction products from these collisions.

This report firstly discusses briefly the physics potential that HERA has to offer and follows this by a description of the H1 detector at HERA. Particular emphasis is made on the subdetectors which can be found in the 'forward direction' (the direction of the proton beam) which is defined by the angular region $7° < \theta < 25°$. The detailed studies presented here concentrate on the detection and triggering of muons within this region with the aim to calculate the elastic cross-section for the production of J/ψ mesons.

Muons are detected in the forward region by the Forward Tracking Detector (FTD), the instrumented iron (which surrounds the whole of the H1 experiment), and the Forward Muon Detector (FMD). Analyses have been completed on the correlation of the momenta measured in the FTD, CTD and the FMD for 1995 and 1996 data and significant differences have been found which can be attributed to problems associated with vertex fitted FTD tracks. Additionally, a preliminary determination of the efficiency and acceptance of the Forward Muon Trigger (FMT) and FMD have been made. These are both important steps towards analysing forward muon producing processes and ultimately other forward processes.

Cross-section measurements for the $\gamma p \to J\psi p$ process have been made by de-

tecting the products of the J/ψ decaying to $\mu^+\mu^-$. The measurements give an indication of the $W_{\gamma p}$ dependence of the cross-section extended to $W_{\gamma p}$ values lower than measured previously by H1.

Between October 1994 and December 1997, this work was supported financially by The University of Birmingham.

This thesis is dedicated to my parents.

Acknowledgements

I would like to thank all the people who have helped me to complete this Phd. I would like to thank Dr Ian Kenyon my supervisor, Professor John Dowell and Dr John Garvey for their help. A special 'Thank you!' also goes to Dr Lee West who displayed huge amounts of patience on many occasions.

As I spent a considerable amount of my time at DESY in Hamburg there are a number of characters to be thanked over in Germany. My red-headed partner in crime has to be Rachel West....thank you for being there so often. The infamous Dr Paul Sutton...I hope you carry on the good work. The 'slight' Mark Smith..we had an excellent laugh. A very special mention goes to the DESY ladies: Molly, Vicky, Jane, and Sarah (and of course Rach)...it was brilliant getting to know you all and indulging ourselves in all those 'girls evenings'. A thank you also goes to the DESY men: Eram, Andy, Julian, Chris (big and small), Dave M., Stuart, Theo, Hugh, Mike, Paul T., Brian, Paul B., Tim and Ben for cheering up the DESY canteen.

A big thank you goes to all my fellow physicists in Birmingham :James, Mark V., and Steve O. (watch out for Chris D..a man who knows how to consume beer). Thank you Dr Paul N. for reading my theory chapter..definitely publishable material and thanks to Mike T., Paul Norman, Sean, Brian, Adam, Alun, Dave L., and Dave E. for cheering up the Birmingham coffee room (while I wasn't in it).

I would also like to mention and thank all my friends who may (blissfully) have had no idea about what I have been studying but have had to suffer moments of intense dullness when I have tried to explain to them what a J/ψ is...sorry about that. A special thanks goes to Sarah and Russ, Max, Greg and Katey and my incredibly loving and understanding parents who I have dedicated this thesis to...how

many years of torment has it been now?

Finally, after three years I have become particularly bad at pub quizzes (isn't that true Dr Monks!?) and I feel it is now time to stop drinking out of plastic beer glasses.

A big thank you also goes to anyone I have forgot to mention...

Contents

1 Physics at Hera **1**

1.1 Lepton-Proton Scattering at HERA 2

1.2 Deep-Inelastic Scattering 3

1.3 Photoproduction 5

1.3.1 Hard Scattering Processes 7

1.4 Diffractive Production Mechanisms 9

1.5 Heavy Flavour Production 12

1.5.1 The J/ψ Meson 13

1.5.2 J/ψ Photoproduction 13

1.5.3 The Vector Meson Dominance Model 15

1.5.4 The Colour Dipole Model 17

1.5.5 Diffractive J/ψ Production 18

1.5.6 Peturbative QCD J/ψ Production 18

1.5.7 Results 19

2 The H1 Detector **21**

2.1 The HERA accelerator 21

2.2 The H1 Detector 21

2.3 The H1 Tracking Detectors 25

2.3.1 The Central Tracking Detector 25

2.3.2 The Forward Tracking Detector (FTD) 27

2.3.3 The Proportional Chambers 29

2.4 The Calorimeters of H1 31

2.4.1 The Liquid Argon Calorimeter 31
2.4.2 SPACAL 32
2.4.3 The PLUG Calorimeter 33
2.4.4 The Tail Catcher 34
2.5 The Muon System 34
2.5.1 The Instrumented Iron 34
2.5.2 The Forward Muon Detector 35
2.6 The 'Down Stream' Forward Detectors 38
2.7 Luminosity Monitoring 40
2.8 Triggering 42

3 Track Reconstruction and Triggering 44
3.1 Forward Track Reconstruction 44
3.2 Instrumented Iron Track Reconstruction 46
3.3 FMD Track Reconstruction 48
3.3.1 Pair Finding 48
3.3.2 Track Segment Reconstruction 48
3.3.3 Pre- and Post-toroid Track Segment Linking 50
3.4 Forward Muon Trigger 53
3.4.1 The Design Philosophy of the FMT 53

4 Event Selection 58
4.1 Event Classification 58
4.1.1 Inner Track Cuts 59
4.1.2 Outer Track Cuts 60
4.2 Track Selection 61
4.2.1 Removal of 'Bad' Inner Tracks 61
4.2.2 Inner Track Hypothesis Removal 66
4.3 Muon Track Linking 67
4.3.1 Muon Link Hypothesis Removal and the Selection of 'Best' Links 67

5 Momentum Correlation Studies **68**

5.1 Correlation Methods. 69

5.2 Data Samples 69

5.3 Momentum Correlations. 70

5.4 False Links 72

5.5 The Dependence of False Links on the Number of FTD and FMD Hits 80

5.6 The Momentum Residual (Δp) between the FTD and the FMD measurements. 83

5.6.1 Momentum Correlations between the FTD and the CTD and the FTD and the FMD. 86

5.6.2 Wrong Sign Linking 93

5.6.3 Charge Ambiguities 94

5.7 Momentum Correction Factors 102

5.8 Conclusion 115

6 Detector and Trigger Efficiency Studies **117**

6.1 The Forward Muon Detector Track Reconstruction and Trigger Efficiency 118

6.1.1 The FMD Track Reconstruction Efficiency 119

6.1.2 The FMD Track Linking Efficiency 124

6.1.3 The Forward Muon Trigger Efficiency and Acceptance 124

6.2 The Forward Iron End-Cap Track Reconstruction and Trigger Efficiency 126

6.3 The Inner Track Reconstruction and Triggering Efficiencies 130

6.3.1 The FTD and CTD Track Reconstruction Efficiencies 131

6.3.2 The Z-Vertex Trigger Elements 132

6.3.3 Central Track Trigger Elements 134

6.3.4 The Topological Trigger Element 135

6.3.5 Summary of the Inner-Track Trigger Efficiencies 136

7 Elastic J/ψ Photoproduction at Low $W_{\gamma p}$ **137**

7.1 Preliminary Elastic Event Sample 138

7.1.1 Event Types. 140
7.2 Monte Carlo Generators 144
7.2.1 The DIFFVM Generator 144
7.2.2 The LPAIR Generator 146
7.3 Monte Carlo Simulation 146
7.4 The Cross-Section Measurement 147
7.4.1 Determination of the Number of Elastic Events 147
7.4.2 The Acceptance ($\mathcal{A}$) 151
7.5 Systematic Errors 154
7.6 Results 157
7.6.1 Conclusions 160

List of Figures

1.1 A schematic representation of DIS. 3

1.2 Plot showing the generated values versus the reconstructed values for $W_{\gamma p}$ using the Jacquet-Blondel method. 6

1.3 Example hard photoproduction *resolved* processes. 8

1.4 A hard photoproduction 'direct' process. 9

1.5 A Chew-Frautschi plot of the ρ Regge Trajectory, $\alpha_\rho(t)$. 10

1.6 Schematic diagram illustrating the s-channel and t-channel. 11

1.7 Schematic diagram showing the incident photon fluctuating into a virtual J/ψ^* which is then 'kicked on the mass shell' by interacting with a pomeron, $\mathbb{P}$. 15

1.8 Schematic diagrams showing (a) the elastic J/ψ production mechanism and (b) the dissociative J/ψ production mechanism. 18

1.9 Diagram illustrating diffractive production of J/ψ as as described by the Ryskin Model. 19

1.10 The cross-sections $\sigma(\gamma p \to J/\psi p)$ measured at HERA and in fixed target experiments ($W_{\gamma p} < 30\,\mathrm{GeV}$). 20

2.1 The layout of the HERA accelerator situated at DESY, Hamburg . . 22

2.2 A 3D view of the H1 detector. 24

2.3 A side view of the H1 tracking detectors. 26

2.4 A side view of the CTD. 27

2.5 The design structure of a Planar Drift Chamber. 28

2.6 The design structure of a Radial Drift Chamber. 29

2.7 The Calorimetry System of the H1 Detector. 33
2.8 A cross-sectional view through the instrumented iron. 35
2.9 A cross-sectional view of the forward muon system. 36
2.10 A θ octant layer. 37
2.11 A ϕ octant layer. 37
2.12 An example of an event showing an elastic J/ψ decay. 39
2.13 The design structure of a Proton Remnant Tagger. 40
2.14 A schematic diagram illustrating the layout of the H1 Luminosity System. 41

3.1 Figure showing the track reconstruction efficiency of the FTD as a function of the total number of tracks reconstructed by the FTD. . . 46
3.2 The momentum resolution ($\frac{\sigma_p}{p}$) as measured by the Instrumented Iron. 47
3.3 A cross-sectional view through cells found in the FMD. 49
3.4 A cross-sectional view of the pre-toroid layers which are part of the FMD illustrating the segment finding procedure. 50
3.5 A cross-sectional view of the pre-toroid layers found in the FMD illustrating the track finding procedure. 51
3.6 A L5 histogram illustrating the number of hits typically detected by the FMD. 52
3.7 A block diagram of the FMT. 55
3.8 An 8×8 $r\phi$ bit map of a θ layer of the FMD. 56

4.1 Distributions for the CTD variables forming part of the track selection criteria. 64
4.2 Distributions for the FTD variables forming part of the track selection criteria. 65
4.3 Distributions for the combined track variables forming part of the track selection criteria. 66

5.1 The momentum measured by the FTD versus the CTD and FMD momentum. 71

5.2 The energy loss of a muon passing through the FMD toroid. 72
5.3 Correlation plot showing the momentum measurement made by versus the momentum measurement made by FMD. 73
5.4 An example event that can be found in region (1). 74
5.5 An example event that can be found in region (2). 76
5.6 An example event that can be found region (3). 77
5.7 An example event that can be found region (3). 78
5.8 An example event that can be found region (4). 79
5.9 The momentum measured by the FMD versus the momentum measured by the FTD as a function of FTD planar drift chamber hits. . . 81
5.10 The ratio of the number of false links divided by the total number of links shown as a function of FTD planar drift chamber hits and the total number of hits detected by the pre-toroid layers of the FMD. . . 82
5.11 The ratio of the number of false links divided by the total number of links shown as a function of FTD planar drift chamber hits and the total number of hits detected by the pre-toroid layers of the FMD. . . 83
5.12 The momentum residual (Δp) for data calculated using the momentum measured by the FTD and momentum measured by the FMD. . 84
5.13 The momentum residual (Δp) for Monte Carlo calculated using the momentum measured by the FTD and momentum measured by the FMD. 85
5.14 Correlation plot showing the momentum measurement made by the CTD versus the momentum measurement made by the FTD. 88
5.15 The value of ϕ as measured by the CTD. 89
5.16 Distributions showing $|p_{FTD}|$-$|p_{CTD}|$ as a function of the momentum measured by the CTD. 90
5.17 Distributions showing $|p_{FTD}|$-$|p_{FMD}|$ as a function of the momentum measured by the FMD. 91

5.18 The mean values of the Breit-Wigner fits applied to the distributions plotted in figures 5.16 and 5.17 are plotted against the momentum measured by the CTD or FMD for 1995 data. 92
5.19 Correlation plot showing how muon tracks with different charges have been incorrectly linked. 93
5.20 Distributions showing $|p_{FTD}|$-$|p_{CTD}|$ as a function of the momentum measured by the CTD for positively charged tracks. 95
5.21 Distributions showing $|p_{FTD}|$-$|p_{CTD}|$ as a function of the momentum measured by the CTD for negatively charged tracks. 96
5.22 Distributions showing $|p_{FTD}|$-$|p_{FMD}|$ as a function of the momentum measured by the FMD for positively charged tracks. 97
5.23 Distributions showing $|p_{FTD}|$-$|p_{FMD}|$ as a function of the momentum measured by the FMD for negatively charged tracks. 98
5.24 The mean values of the Breit-Wigner fits applied to the distributions plotted in figures 5.20 and 5.22 and figures 5.21 and 5.23 have been plotted against the momentum measured by the CTD or FMD for different sign tracks for 1995 data. 99
5.25 The mean values of the Breit-Wigner fits applied to the distributions ($|p_{FTD}|$-$|p_{CTD}|$ or $|p_{FTD}|$-$|p_{FMD}|$) plotted against the momentum measured by the CTD or FMD for 1996 data. 100
5.26 The mean values of the Breit-Wigner fits applied to the distributions $|p_{FTD}|$-$|p_{CTD}|$ and $|p_{FTD}|$-$|p_{FMD}|$ plotted against the momentum measured by the CTD or FMD for different sign tracks for 1996 data. . . 101
5.27 Figure showing the momentum measured by the FTD for muon tracks tracks resulting from the decay of a J/ψ meson before and after the momentum is corrected. 103
5.28 Correction factors for 1995 data for positively charged tracks. 104
5.29 Correction factors for 1995 data for negatively charged tracks. 105
5.30 Correction factors for 1996 data for positively charged tracks. 106
5.31 Correction factors for 1996 data for negatively charged tracks. 107

5.32 The reconstructed invariant mass of J/ψ mesons corresponding to the two event samples, before and after the momentum measured by the FTD has been corrected. 111
5.33 The reconstructed invariant mass of J/ψ mesons corresponding to the one forward going muon event sample for 1995 data after the momentum measured by the FTD has been corrected. The same resonance is shown using the momentum measured by the FMD. . . . 113
5.34 The reconstructed invariant mass of J/ψ mesons corresponding to the two forward going muons event sample for 1995 data after the momentum measured by the FTD has been corrected. The same resonance is shown using the momentum measured by the FMD. . . . 114

6.1 Plot showing the track reconstruction efficiency of the FMD as a function of $\theta_{\rm FTD}$ and $\rm p_{FTD}$. 120
6.2 Hit-map distributions of Class 24 muon tracks illustrating the 'Maltese Cross Effect'. 122
6.3 Plot showing the linking and track reconstruction efficiency of the FMD as a function of $\theta_{\rm FTD}$ and $\rm p_{FTD}$. 123
6.4 Plot showing the efficiency of the FMT (telement 0) as a function of $\theta_{\rm FTD}$ and of $\rm p_{FTD}$ 125
6.5 The design structure of a the forward iron end-cap. 127
6.6 Figure showing the efficiency of the track reconstruction of the forward iron end-cap. 128
6.7 Figure showing the efficiency of the forward iron end-cap trigger element Mu_FIEC. 129
6.8 Figure showing the efficiency of the z-vertex trigger element $zVtx\_small$ for each event sample. 133
6.9 Figure showing the efficiency of the z-vertex trigger element $zVtx\_Cls$ as a function of the momentum and the polar angle for the forward going track. 134

6.10 Figure showing the efficiency of the topological trigger element $Topo\_BR$ as a function of the momentum and the polar angle for the forward going track. 135

7.1 Plots showing the generated values and the reconstructed values for z. 139
7.2 The acceptance as a function of $W_{\gamma p}$ for the two event samples. . . . 141
7.3 Example events which are typical of the elastic event categories. . . . 142
7.4 The reconstructed invariant mass distributions for the elastic decay channel $J/\psi \to \mu^+\mu^-$. 143
7.5 Schematic diagram showing the VDM process responsible for the production of J/ψ via a colourless object called the pomeron ($\mathbb{P}$). 145
7.6 Schematic diagram showing the QED process responsible for the production of $\mu^+\mu^-$ pairs. 146
7.7 Figure comparing the renormalised LPAIR Monte Carlo with the data for differing event samples. 149
7.8 The cross-sections $\sigma(\gamma p \to J/\psi X)$ measured at HERA for combined 1995 and 1995 data. 151
7.9 Comparison between Monte Carlo and data distributions for the one forward going muon sample. 152
7.10 Comparison between Monte Carlo and data distributions for the two forward going muons sample. 153
7.11 The elastic J/ψ photoproduction cross-section shown as a function of $W_{\gamma p}$. 162

List of Tables

1.1 Properties of the J/ψ Meson. 13

3.1 The four trigger elements of the FMT that correspond to fully validated tracks. 57

5.1 The fit parameters from the double Gaussian fit made to the distributions shown in plots (a), figures 5.12 and 5.13. 87

5.2 The fit parameters from the double Gaussian fit made to the distributions shown in plots (a), figures 5.12 and 5.13. 87

5.3 Coefficients obtained from fitting n (n=0,3) degree polynomials to the distributions shown in figures 5.28, 5.29, 5.30 and 5.31. 109

5.4 Coefficients obtained from fitting n (n=0,3) degree polynomials to the distributions shown in figures 5.28, 5.29, 5.30 and 5.31. 110

5.5 The values of the mean and width of the J/ψ resonances plotted in figure 5.32 before and after the correction factors have been applied. 112

5.6 The values of the mean and width of the J/ψ resonances plotted in figure 5.32 before and after the correction factors have been applied. 115

6.1 Inner track trigger element efficiencies. 136

7.1 Subtriggers used for one forward going muon sample. 140

7.2 Subtriggers used for two forward going muons sample. 140

7.3 Table giving the values of the backgrounds contributing to the elastic samples for both event types. 150

7.4 Table giving the values of the acceptance for triggering and reconstructing the elastic J/ψ events for both event samples. 154
7.5 Table listing the four possible event categories described by the FMD and the FMT and the efficiency for obtaining the event category. . . . 155
7.6 Systematic errors for the two data samples. 158
7.7 A summary of the elastic J/ψ photoproduction cross-sections for the $W_{\gamma p}$ ranges measured in this analysis. 159

Chapter 1

Physics at Hera

HERA is the first ever ep collider. It accelerates and stores 820 GeV protons and 27.5 GeV electrons (or positrons), which when collided give an approximate center of mass energy of 300 GeV. The corresponding four momentum transfer squared (q^2 or $-Q^2$) can almost reach 10^5 GeV^2, which is at least two orders of magnitude larger than ever before[1].

The most significant evidence for the dynamical structure of the proton [1] comes from deep inelastic lepton-proton scattering (DIS). The proton is made up from point-like constituents (partons). It consists of three valence quarks and a large number of sea quarks and gluons each carrying a fraction of the total proton momentum which is defined as the Bjorken x variable (equation 1.3). Information about the structure of the proton can be obtained by probing the proton with a photon probe of virtuality, Q^2. The resolving power of the probe increases as Q^2 increases. Structure functions are defined which quantify the density of partons as a function of x. These structure functions have been measured for the first time at HERA in the kinematic region of very small x.

There is also potential to study the weak charged current (the exchange of $W^{\pm}$ bosons) at high momentum transfer [2]; the momentum distributions for heavy quarks and other heavy flavour physics; photoproduction [3]; and possible produc-

[1] Before HERA was operational the maximum Q^2 value reach was approximately 300 GeV^2 and the minimum x value reach was approximately 10^{-2}.

tion of exotic particles such as leptoquarks [4].

This chapter presents the kinematics and the theoretical basis and motivation for measuring the cross-section for elastic photoproduction of J/ψ mesons. A brief overview of DIS, photoproduction and diffractive processes are also given.

1.1 Lepton-Proton Scattering at HERA

Over most of the kinematic range at HERA the electron(positron)-proton scattering is dominated by the neutral current process :

$$e(k) + p(P) \longrightarrow e(k') + X$$

where X represents the final hadronic state and the bracketed quantities are the particle four momenta. In figure 1.1 the mechanism of a DIS ep interaction is illustrated. The virtuality of the exchange boson, Q^2, is defined as

$$Q^2 \equiv -q^2 = -(k - k^{'})^2 \tag{1.1}$$

where q is the four momentum transferred. The exchange can either be of a quasi-real photon ($Q^2 \approx 0$), a virtual photon ($Q^2 > 0$) or of a Z° boson. For charged current interactions, in which the $W^\pm$ boson is exchanged, the interaction is of the general form

$$e + p \longrightarrow \nu_e + X.$$

Interactions which involve the exchange of a Z° or $W^\pm$ become significant at high values of Q^2. This is because the propagator term responsible for the exchange has the form

$$\propto \frac{1}{Q^2 + M^2} \tag{1.2}$$

where M is the mass of the exchanged vector boson. At low values of Q^2 ($\ll M^2$) the cross-section is dominated by the exchange of a photon and it is only at $Q^2 \approx M^2$ that the contribution due to the exchange of Z° or $W^\pm$ becomes significant. For $1.2^2 \lesssim Q^2 \lesssim 100\,\mathrm{GeV}^2$, electrons are detected in the H1 electromagnetic calorimeter,

[2]This is the lowest Q^2 accessible using the Spacal. The BEMC, which was used prior to 1995 could measure a minimum Q^2 of approximately $4.0\,\mathrm{GeV/c}^2$.

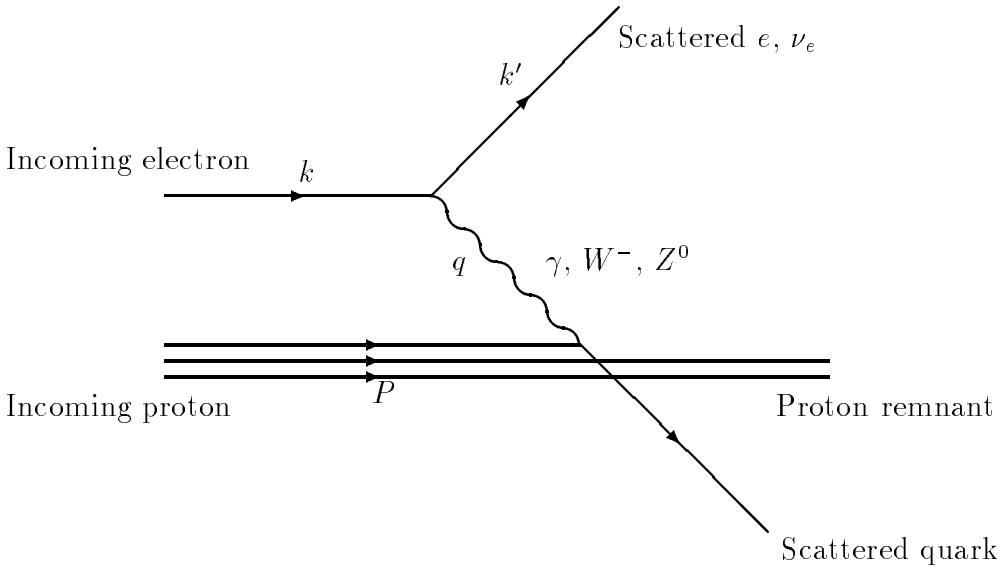

Figure 1.1: *A schematic representation of DIS.*

Spacal, while the LAr covers a higher Q^2 region (equation 1.10 defines the relation between θ and Q^2). Interactions in which the momentum transfer is $Q^2 \approx 0$ are mediated by the exchange of a quasi-real photon and are referred to as 'photoproduction' interactions.

1.2 Deep-Inelastic Scattering

In a typical DIS event, where the scattered lepton is detected in the calorimeter, the event kinematics can be reconstructed from the initial and final state electron energies, E_e and $E_{e'}$, and the electron scattering angle, θ. It is most convenient to work with the Lorentz invariant variables Q^2 and the Bjorken scaling variable x. The definition for Q^2 has already been given by equation 1.1. The variable x is defined as [5] :

$$x \equiv \frac{Q^2}{(2P.q)}. \tag{1.3}$$

Further useful variables are :

$$y \equiv \frac{(P.q)}{(P.k)} \tag{1.4}$$

and

$$W^2 \equiv (q+P)^2 \simeq \frac{Q^2(1-x)}{x}, \tag{1.5}$$

where W is the total hadronic invariant mass and also the center of mass energy of the $\gamma^* p$ system (referred to in photoproduction as $W_{\gamma p}$). The variable y is the fraction of energy that the incident lepton transfers to the proton when measured in the rest frame of the incident proton.

The variable x is most easily interpreted in a reference frame in which the target proton is approaching infinite momentum, i.e. $P^2 \gg M^2$ (where M is the mass of the proton) [6, 7]. In such a frame, the momenta of the constituents will be almost collinear with the proton momentum, so that to a very good approximation the target can be viewed as a stream of partons, n, each carrying a fraction x of the proton momentum. These fractions are normalized to give :

$$\sum_i \int dx_i \, x \, f_i(x) = 1 \tag{1.6}$$

where $f_i(x)\, dx_i$ is the probability that partons of flavour i carry a fraction between x_i and $x_i + dx_i$ of the proton's momentum P. In the infinite momentum frame, relativitistic time dilation lengthens the characteristic time constant in which the partons within the proton interact with one another relative to the time constant with which the photon probe interacts with the parton. This means that each parton can be approximated to a free particle.

The center of mass energy squared, s, is defined by :

$$s \equiv (k+P)^2. \tag{1.7}$$

When the center of mass energy is high enough that all the beam masses can be neglected,

$$s \simeq 4 E_e E_p \tag{1.8}$$

where E_e is the electron beam energy and E_p the proton beam energy. In the same approximation the variables Q^2, x and y are related by the equation :

$$Q^2 \approx sxy \quad (s \gg M^2) \tag{1.9}$$

It can also be shown that the variables y and Q^2 can be expressed in terms of the final state scattering angle, θ, and the final state energy, $E_{e'}$, of the scattered lepton by

$$Q^2 = 4E_e E_{e'} \cos^2\left(\frac{\theta}{2}\right). \tag{1.10}$$

and

$$y = 1 - \frac{E_{e'}}{E_e} \sin^2\left(\frac{\theta}{2}\right). \tag{1.11}$$

1.3 Photoproduction

The major part of the total cross section at HERA is close to $Q^2 = 0$ (photoproduction) because the flux of virtual photons from the electron has the form $\sim \frac{1}{Q^2}$ and hence peaks as $Q^2 \to 0$. Such events open up a wide range of QCD studies including examples of both perturbative and non-perturbative physics. Since photoproduction events have such a high rate, they also contribute a major background to other physics processes. Early physics publications using HERA data have fully exploited such events. It is sometimes possible in a fraction of events to tag the recoil electron in the electron tagger of the luminosity measurement system and measure the small values of θ_e. For these tagged photoproduction events $Q^2 < 0.01\,\mathrm{GeV}^2$ and y (and $W_{\gamma p}$) are determined directly from the relation 1.11. For untagged photoproduction events the Jacquet-Blondel method [8] is used to reconstruct y from information on the final hadronic state :

$$y_{JB} = \sum_i \frac{(E_i - p_{i,z})}{2E_e} \tag{1.12}$$

where E_i is the total energy of the final state hadrons and $p_{i,z}$ is the projection of the total hadronic momentum in the direction of the initial proton beam. The variable $W_{\gamma p}$ can then be obtained from the reconstructed y_{JB} and the beam energies :

$$W^2_{\gamma p} \simeq 4E_e E_p\, y_{JB} (\simeq s\, y_{JB}) \tag{1.13}$$

Figure 1.2 shows a comparison of the generated values against the reconstructed values for $W_{\gamma p}$. The Monte Carlo generator used is the DIFFVM generator [65] which

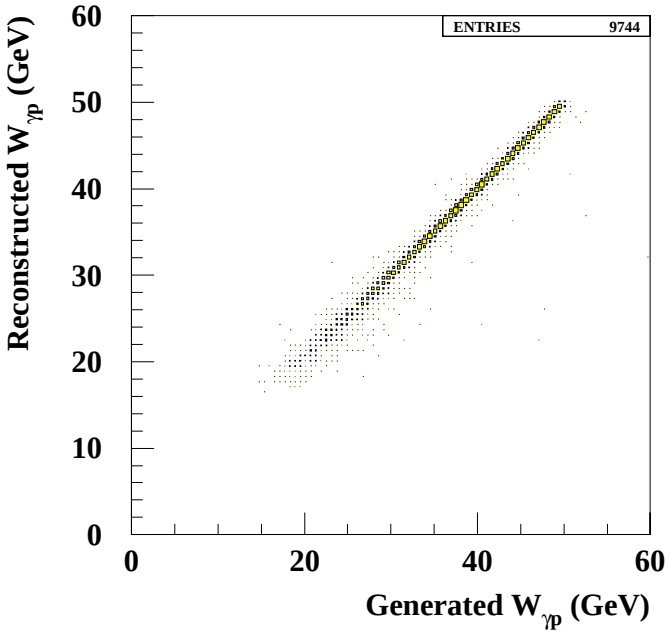

Figure 1.2: *Plot showing the generated value versus the reconstructed value for $W_{\gamma p}$ using the Jacquet-Blondel method. The events describe the elastic process $\gamma p \to J/\psi p$ with $J/\psi \to \mu^+\mu^-$ using the DIFFVM generator as described in chapter 7.*

models the elastic process $\gamma p \to J/\psi p$ with the subsequent decay $J/\psi \to \mu^+\mu^-$ and which will be described later in chapter 7.

Cross-sections for photoproduction are cross-sections for real or nearly real photons. At HERA, the incident electron beam is the source of photons and using the Weizsäcker Williams approximation [9] the cross-section for low Q^2 ep-scattering events can be related to the photoproduction cross-section by :

$$\sigma(ep \to J/\psi X) = \int_{y_{min}}^{y_{max}} dy \int_{Q^2_{min}}^{Q^2_{max}} dQ^2 \, \mathcal{F}_{\gamma/e}(y, Q^2) \, \sigma(\gamma p \to J/\psi X). \qquad (1.14)$$

The ep cross-section is measured for the interval of $Q^2_{min} \leq Q^2 \leq Q^2_{max}$[3] and $y_{min} \leq y \leq y_{max}$, where :

$$Q^2_{min} = m_e^2 \frac{y^2}{1-y} \text{ and } \quad \mathrm{Q^2_{max}} = 1.2\,\mathrm{GeV}^2 \qquad (1.15)$$

[3]The value of Q^2_{max} is determined by the acceptance of the detector which detects the scattered electron in the backward direction (see chapter). Between 1994 and 1995 this detector changed and hence the value of Q^2_{max} changed from $4.0\,GeV$ to $1.2\,GeV$.

The flux of transverse[4] photons is given by the expression [10] :

$$\mathcal{F}_{\gamma/e}(y,Q^2) = \frac{\alpha_{em}}{2\pi}\frac{1}{yQ^2}\left(1+(1-y)^2-\frac{2m_e^2y^2}{Q^2}\right). \tag{1.16}$$

It can be seen from this expression that the photon flux decreases rapidly as Q^2 and y increase. The photoproduction cross-section, $\sigma(\gamma p \to J/\psi X)$, has only a weak dependence on Q^2 and y and is therefore approximately constant over the Q^2 and y integration interval. Thus, the expressions given by 1.14 and 1.16 yield to a good approximation :

$$\sigma(\gamma p \to J/\psi X) = \frac{\sigma(ep \to eJ/\psi X)}{\Phi_{\gamma/e}}. \tag{1.17}$$

The 'flux factor',$\Phi_{\gamma/e}$, is the photon flux integrated over Q^2 and y :

$$\Phi_{\gamma/e} \propto \int_{y_{min}}^{y_{max}} dy \int_{Q^2_{min}}^{Q^2_{max}} dQ^2 \; \mathcal{F}_{\gamma/e}(y,Q^2)\,\frac{\sigma(\gamma p \to J/\psi X)}{(1+\frac{Q^2}{M_V^2})^2} \tag{1.18}$$

where M_V is the mass of the vector meson.

1.3.1 Hard Scattering Processes

High p_T^2 ($\gtrsim 1\,\mathrm{GeV}^2/\mathrm{c}^4$) particles or a jet in the final state are signatures of 'hard' photoproduction processes. The value of p_T^2 sets a scale that enables the processes to be calculated perturbatively. Hard photoproduction interactions are often subdivided into *resolved* and *direct* processes [11, 12] which are illustrated by figures 1.3 and 1.4 respectively.

Resolved Photon Contributions

These are γp scattering processes which are sensitive to the hadronic structure of the photon. The photon can be resolved into partons[5] and subsequently one of the constituent partons (a quark or gluon) takes part in a hard scattering. At high p_T^2

[4]The longitudinal photon flux amounts to approximately 0.45% and 0.48% of the transverse flux for the $W_{\gamma p}$ ranges 20< $W_{\gamma p}$ <27 GeV and 25< $W_{\gamma p}$ <40 GeV respectively and can therefore be neglected in further calculations

[5]As described for example by the VMD model (section 1.5.3).

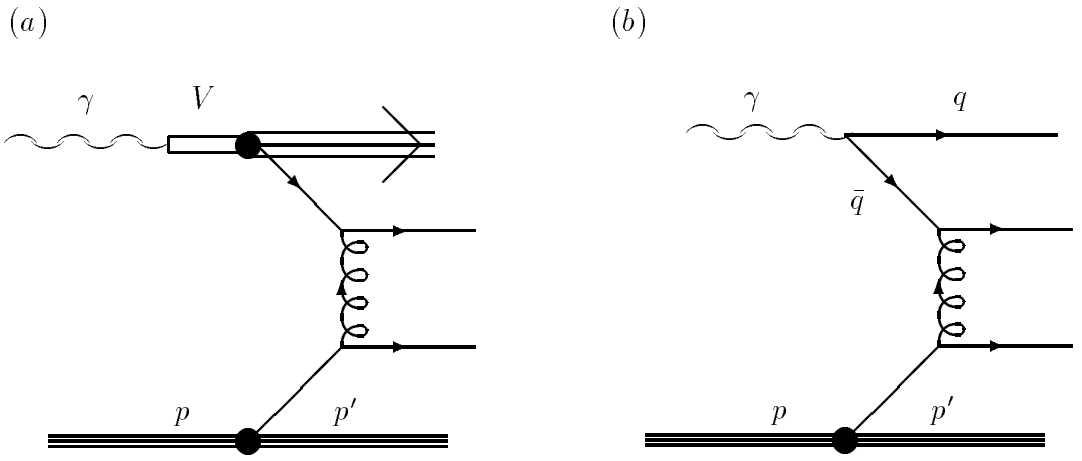

Figure 1.3: *Example hard photoproduction resolved processes. Diagram (a) shows the process whereby the photon has been resolved into a complicated hadronic structure as described by the VDM model in section 1.5.3 and diagram (b) shows the anomalous process where the photon is resolved into a simple $q\bar{q}$-pair.*

($\gtrsim$50 GeV^2/c^4) there is a dominant contribution from the 'anomalous' process which corresponds to the coupling of a photon with a non QCD-developed $q\bar{q}$-pair. This high p_T^2 sets a scale where the strong coupling constant is small, hence further QCD development of the $q\bar{q}$-pair is suppressed.

In resolved processes the spectator partons in the photon and the proton fragment into two low p_T remnants moving close to the collision axis. The photon remnant will travel in roughly the direction of the incident photon (which at HERA coincides with the electron direction). The fraction of the photon momentum carried by the interacting parton x_γ in a photon has the value $x_\gamma < 1$ for resolved processes.

Direct Photon Processes

Direct interactions are where the photon couples directly with partons in the nucleon through processes such as photon-gluon fusion and QCD Compton Scattering. The entire photon energy goes into the hard partonic final state ($x_\gamma = 1$) and a typical event topology is that of two high-p_T jets. The remnant from the proton has low

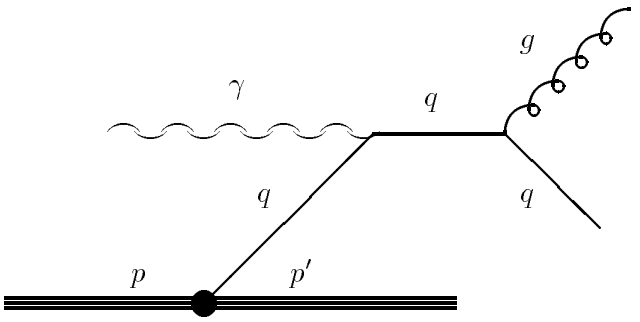

Figure 1.4: *A hard photoproduction 'direct' process.*

transverse energy and typically disappears undetected down the beam pipe.

1.4 Diffractive Production Mechanisms

The basic properties of diffractive processes [13] were established in the 1960's and 1970's through hadron-hadron scattering experiments. These properties which are typical of such soft, peripheral interactions were found to be best explained by the Regge approach [14]. The fundamental result of Regge theory is to parameterize the cross-section as a function of the energy of the system.

In Regge theory the asymptotic behaviour of the energy dependences of total, elastic, and diffractive dissociation cross-sections is determined by the properties of 'Regge trajectories' :

$$\alpha(t) = \alpha(0) + \alpha' t \tag{1.19}$$

This trajectory is a linear parameterisation which can be fitted to the plot of angular momentum versus the mass-squared of the reggeized particle (Chew-Frautschi plot). If the angular momentum versus the four-momentum squared is plotted for all recorded mesons then a series of linear trajectories with approximately unit slope are observed. An example of the trajectory for which the lowest lying state is the ρ meson is shown in figure 1.5.

Positive values of M^2 correspond to the s-channel where states produced as resonances are met at integral values of angular momentum. Negative values of M^2

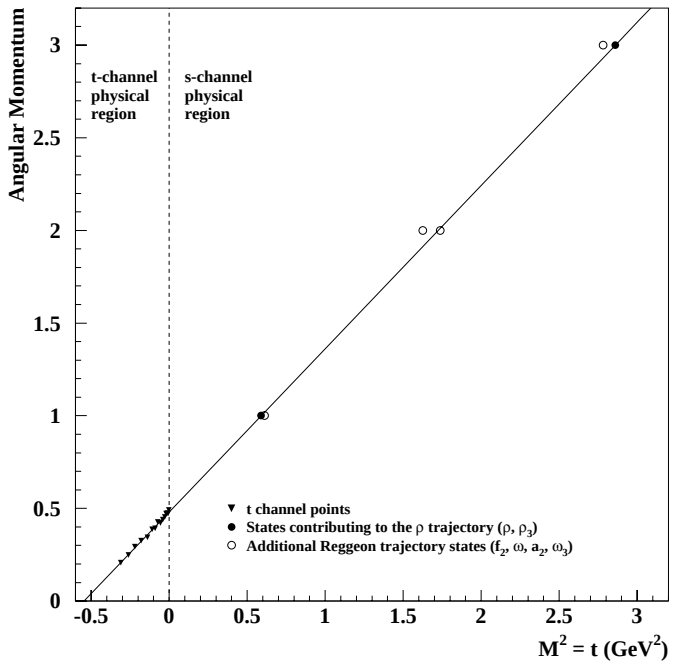

Figure 1.5: *A Chew-Frautschi plot of the ρ Regge Trajectory, $\alpha_\rho(t)$.*

correspond to t-channel exchanges. To briefly explain the definitions of s and t, figure 1.6 shows the two-body scattering process, $AB \to CD$, where (a) illustrates the s-channel exchange process and (b) the related t-channel process. For photoproduction the center of mass energy is $W^2_{\gamma p}$ (defined by equation 1.5) and the negative quantity t is the square of the 4-momentum transfer at the proton vertex.

Regge theory thus makes the prediction that the $W_{\gamma p}$ dependence of the total cross section depends on the nature of the exchange particle dominating the elastic amplitude. The total cross-section can be related to the imaginary part of the forward ($t = 0$) scattering amplitude of the elastic process by the optical theorem. It was demonstrated by Donnachie and Landshoff [15] that the energy dependence of measured total hadronic cross-section can be described as follows :

$$\sigma_{tot} = As^{\lambda_1} + Bs^{-\lambda_2} \tag{1.20}$$

where the universal values of the indices are :

$$\lambda_1 \approx 0.0808, \quad \lambda_2 \approx 0.4525 \tag{1.21}$$

and are independent of the type of colliding particles[6]. The energy dependence of

[6]The parameters, A and B, are dependent on the colliding particles.

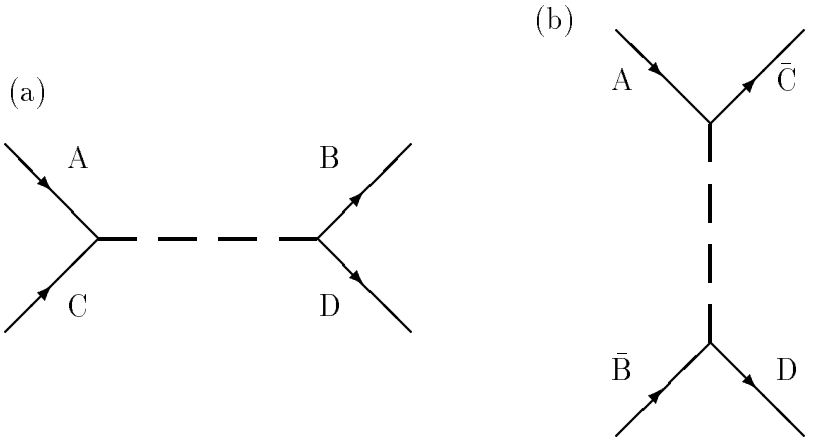

Figure 1.6: *Schematic diagram illustrating the s-channel and t-channel.*

the cross section as given by equation 1.20 is related to the intercept of a Regge trajectory :

$$\alpha(0) = 1 + \lambda_i \quad (i = 1, 2). \tag{1.22}$$

At low energies the total cross-section dependence on the center of mass energy (s) is approximately $s^{-0.5}$. This is attributable to mesons lying on trajectories with intercepts of approximately 0.5 (ρ, ω, a_2, and f_2). It was found that at high energies the total and elastic cross-sections vary only slowly with energy. By fitting to the data [15] the value of $\alpha(0)$ is found to be approximately 1.08 which is considerably higher than all meson trajectories ($\alpha(0) \lesssim 0.5$). The conclusion is that the dominant exchange at high energies is due to a trajectory with intercept ≈ 1.08 which is named the 'pomeron'. As yet the structure of the pomeron is not well known. However, first measurements of the behaviour of this exchange object have been made in diffractive photoproduction at HERA [16]. There are no recorded s-channel resonances lying on the same trajectory.

Elastic processes occurring at HERA energies are therefore expected to be dominated by the exchange of a pomeron. The cross-section dependence on $W_{\gamma p}$ at fixed t for an elastic scattering process such as exclusive vector meson production is :

$$\frac{d\sigma}{dt} \propto \left(\frac{W_{\gamma p}^2}{W_0^2}\right)^{2(\alpha_{\mathbb{P}}(t)-1)} \tag{1.23}$$

Data have shown that at fixed $W_{\gamma p}$ the t dependence of the cross-section is well

approximated by an exponential. The behaviour may be approximated to e^{bt}, where $b = 2b_A + 2b_B$ and where the parameters b_A and b_B are the slopes of the form factors for the particles A and B.

Including the full t-dependence in equation 1.23 gives the following result :

$$\frac{d\sigma}{dt} \propto \left(\frac{W_{\gamma p}^2}{W_0^2}\right)^{2(\alpha_{I\!P}(0)-1)} e^{b't}, \tag{1.24}$$

where b' is given by :

$$b' = 2b_A + 2b_B + 2\alpha'_{I\!P} \ln\left(\frac{\mathrm{W}_{\gamma \mathrm{p}}^2}{\mathrm{W}_0^2}\right). \tag{1.25}$$

The total elastic vector meson cross-section can be calculated by integrating this expression over t :

$$\frac{d\sigma_{\gamma p}}{dt} \propto \left(\frac{W_{\gamma p}^2}{W_0^2}\right)^{2(\alpha_{I\!P}(0)-1)} e^{b't} \equiv \left(\frac{W_{\gamma p}^2}{W_0^2}\right)^{2\lambda_2} e^{b't} \tag{1.26}$$

$$\sigma_{\gamma p} \propto \int_{-\infty}^{t_{min}\approx 0} \left(\frac{W_{\gamma p}^2}{W_0^2}\right)^{2\lambda_2} e^{b't}\, dt \tag{1.27}$$

$$\sigma_{\gamma p} \propto \left(\frac{W_{\gamma p}^2}{W_0^2}\right)^{2\lambda_2} \left[\frac{1}{b'}\, e^{b't}\right]_{-\infty}^{0} \tag{1.28}$$

Hence,

$$\sigma(\gamma p \to V p) \propto \frac{1}{b'} \left(\frac{W_{\gamma p}^2}{W_0^2}\right)^{2\lambda_2} \tag{1.29}$$

where $b' = 2b_A + 2b_B + 2\alpha'_{I\!P} \ln\left(\frac{\mathrm{W}_{\gamma \mathrm{p}}^2}{\mathrm{W}_0^2}\right)$.

The overall t-slope, b', at fixed $W_{\gamma p}$ has an energy dependence which results directly from the non-zero value of $\alpha'_{I\!P}$. Hence the b' parameter, should increase with energy and the slope of the t distribution increases as $W_{\gamma p}$ increases. The effect is known as *shrinkage* [13].

1.5 Heavy Flavour Production

Charm is produced in ep collisions at HERA almost exclusively in $c\bar{c}$ pairs[7]. This gives rise to 'open charm' states which are detected after hadronization into charmed

[7]Charm is also produced via b-decay

Charmonium Bound State	Mass (MeV)	Decay Modes	Branching Ratio (%)
J/ψ	3096.88	hadrons	86.0 ± 2.0
		e^+e^-	5.99 ± 0.25
		$\mu^+\mu^-$	5.97 ± 0.25

Table 1.1: Properties of the J/ψ Meson.

mesons such as D^* or D^0 and 'hidden charm' states which are bound $c\bar{c}$ such as J/ψ and ψ'. The production of J/ψ mesons will be discussed in the next section.

1.5.1 The J/ψ Meson

The J/ψ is a bound state of $c\bar{c}$. Such states are known collectively as 'charmonium' states and are analogous to positronium, the bound state of the electron and positron. Some properties of the J/ψ meson are given in table 1.5.1.

The J/ψ was first observed in experiments, at Brookhaven National Laboratory (BNL) [17] and Stanford Linear Accelerator Center (SLAC) [18] in 1974. The BNL experiment was a fixed target experiment which directed a proton beam onto a beryllium target. The SLAC experiment employed the SPEAR electron-positron storage ring.

The discovery of the charmonium states was of particular interest because it was the first direct experimental evidence for a new quark beyond u, d and s quarks. The high mass of the charm quark provides a hard scale in the case of J/ψ photoproduction and thus justifies a perturbative approach.

1.5.2 J/ψ Photoproduction

There have been several mechanisms suggested to describe the photoproduction of J/ψ mesons. In general the processes can be described by the equation :

$$\gamma + p \rightarrow J/\psi + X$$

The elastic (or exclusive) process is the case in which $X = p$. The inelastic case is all the other possible final states where $X \neq p$. These processes can be distinguished by the variable z which is called the 'elasticity' :

$$z \equiv \frac{P.P_{J/\psi}}{P.q}. \tag{1.30}$$

This is the fraction of the photon energy carried by the J/ψ when both are measured in the proton rest frame. For an elastic event the J/ψ takes most of the incoming γ energy (E_γ) so the energy flow into the proton system is limited making it less likely to dissociate. Hence for elastic events :

$$z \equiv \frac{E_{J/\psi}}{E_\gamma} \approx 1.$$

It is also possible that for the case where the proton has gained a small amount of the photon energy that it may dissociate and its products will travel down the beam pipe being undetected in the main detectors. These events, although strictly speaking inelastic, will also have an elasticity value close to unity and will be considered as background in the following studies. The elasticity of proton dissociation events can also be expressed in terms of the invariant mass of the final state M_x produced at the proton vertex :

$$z \approx 1 - \frac{M_x^2}{W_{\gamma p}^2}. \tag{1.31}$$

For elastic events, the squared four-momentum transfer at the proton vertex is :

$$t = (p - p')^2 \tag{1.32}$$

where for photoproduced events :

$$t \approx -p_T^2 \tag{1.33}$$

and p_T is the transverse momentum of the J/ψ meson with respect to the beam axis. Elastic and other diffractive J/ψ processes generally have low values of t as the final state proton momentum is close to the initial state momentum. Proton dissociation processes have on average larger t values than elastic processes as momentum transfer is necessary to fragment the proton.

1.5.3 The Vector Meson Dominance Model

In section 1.3.1 hard photoproduction mechanisms were described, however the photoproduction processes that make the dominant contribution to the cross section are 'soft'. These are processes for which there is an absence of the production of particles with large p_T. From these soft, low energy γp interactions it was observed that the the photon behaviour was similar to that of strongly interacting hadrons. The properties of such interactions are well described by the Vector Dominance Model (VDM) [19, 20]. In this model the photon is acting like a source of quarks and gluons and the process is therefore analogous to hadron-hadron scattering.

An example of VDM process where the incoming photon fluctuates into a virtual J/ψ vector meson can be seen in figure 1.7. The meson is seen to be 'kicked on mass shell' by the interaction with a target proton via a colourless exchange object named the pomeron which was discussed section 1.4.

Photon fluctuations into virtual two-lepton states are well understood within QED, however, it can also fluctuate into a quark-antiquark pair $q\bar{q}$. If the lifetime of the virtual state exceeds $\approx 10^{-25}$ sec (corresponding to an energy or momentum scale of 1 GeV/c) the $q\bar{q}$ pair will have sufficient time to evolve into a hadronic state. If the lifetime is greater than the time of the interaction with the proton then this hadronic state will interact with the proton, resulting in a hadronic interaction.

The uncertainty principle predicts that the photon can fluctuate into a pair

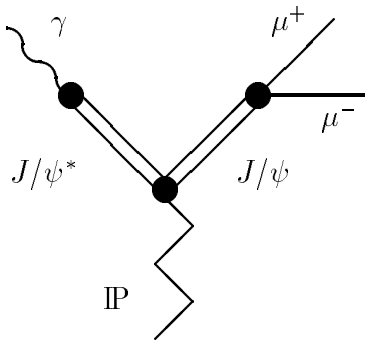

Figure 1.7: *Schematic diagram showing the incident photon fluctuating into a virtual J/ψ^* which is then 'kicked on the mass shell' by interacting with a pomeron,* $\mathbb{P}$.

of charged particles for a time interval of Δt [21]. To determine Δt, assume a real photon ($Q^2 \approx 0$) with energy E_γ interacts with a proton which is at rest. The energy difference ΔE at the vertex where the photon fluctuates into a $q\bar{q}$ pair having the same momentum as that of the photon and a mass of $m_{q\bar{q}}$ is :

$$\Delta E = (E_\gamma^2 + m_{q\bar{q}}^2)^{\frac{1}{2}} - E_\gamma \tag{1.34}$$

The VDM assumes that the fluctuation of the photon is into vector mesons, $m_{q\bar{q}} \simeq m_V$, where m_V is the vector meson mass. For high energy photons, $E_\gamma \gg m_V$, ΔE may be approximated such that :

$$\Delta E \;=\; (1 + \frac{m_V^2}{E_\gamma^2})^{\frac{1}{2}}\, E_\gamma - E_\gamma \;\approx\; (1 + \frac{m_V^2}{2E_\gamma^2})\, E_\gamma - E_\gamma \;=\; \frac{m_V^2}{2E_\gamma}. \tag{1.35}$$

Since, by the uncertainty principle, $\Delta t \sim \frac{\hbar}{\Delta E}$, and setting $\hbar \sim 1$,

$$\Delta t = \frac{2E_\gamma}{m_V^2}. \tag{1.36}$$

When considering a virtual photon ($Q^2 > 0$), the fluctuation time is given by :

$$\Delta t = \frac{2E_\gamma}{Q^2 + m_V^2}. \tag{1.37}$$

This shows that as Q^2 increases, the fluctuation time decreases and the photon behaves more like a point-like object.

Likening photon-hadron interactions to hadron-hadron interactions means that the physical photon may be described by the following state vector :

$$|\gamma\rangle = A|\gamma_A\rangle + B|\gamma_B\rangle \tag{1.38}$$

where $|\gamma_B\rangle$ is the 'bare' photon state component which only interacts electromagnetically and $|\gamma_A\rangle$ is the hadronic state component which can undergo strong interactions. The state $|\gamma_A\rangle$ must have the same quantum numbers as the photon, namely $J^{PC} = 1^{--}$ and $Q = B = S = 0$ as has been experimentally proven in study of quasi-elastic photon interactions [22]. The simplest VDM model states that the hadronic state component constitutes ρ°, ω and ϕ states such that :

$$|\gamma_A\rangle = A_{\rho^\circ}|\rho^\circ\rangle + A_\omega|\omega\rangle + A_\phi|\phi\rangle \tag{1.39}$$

The inclusion of heavier vector mesons is referred to as the generalized vector dominance model (GVDM) [23].

1.5.4 The Colour Dipole Model

An alternative model to the VDM model is that of the Colour Dipole Model [24] which also describes the diffractive photoproduction of vector mesons. For the case of the J/ψ meson, the photon fluctuates into a $c\bar{c}$-pair which then behaves as a colour dipole when interacting with the proton. The interaction is mediated by the exchange of a colourless object and the $c\bar{c}$-pair then combine into the final state vector meson. The interaction between the $c\bar{c}$ pair and the proton takes place over a much shorter time-scale than the fluctuation of the photon to the $c\bar{c}$ pair or the formation of the final state vector meson, thus allowing the expression to be factorised :

$$T(\gamma p \rightarrow J/\psi p) = T(\gamma \rightarrow c\bar{c})\, T(pc\bar{c} \rightarrow pc\bar{c})\, T(c\bar{c} \rightarrow J/\psi). \tag{1.40}$$

The interaction cross-section for the dipole with the proton vanishes as the transverse separation between the $c\bar{c}$-pair tends to zero and is constant (saturates) at large values of r. The amplitude for the process where the $c\bar{c}$-pair turns into a vector meson is related to the overlap integral of their transverse wavefunction and the radial wavefunction of the vector meson :

$$\int |\Psi_{c\bar{c}}(r)\Psi_V(r)|^2 \; dr. \tag{1.41}$$

The process is said to 'scan' the vector meson wavefunction at a transverse separation of the $c\bar{c}$-pair known as the scanning radius and which is given by :

$$r_s = \frac{A}{\sqrt{Q^2 + M_V^2}} \tag{1.42}$$

and where A is a constant estimated to have a value of approximately 6 [24].

The $\gamma p \rightarrow J/\psi p$ cross-section as described by the Colour Dipole Model may be approximated as being proportional to the amplitude squared of the vector meson wavefunction defined at r_s. This differs from the VDM Model which assumes that in essence that the cross-section is proportional to the $c\bar{c}$ wavefunction at the origin.

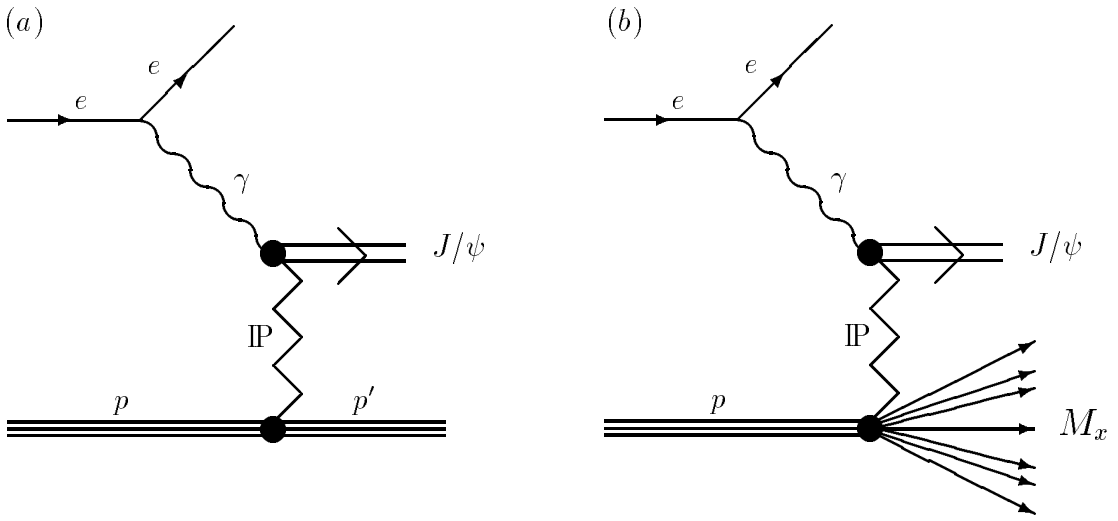

Figure 1.8: *Schematic diagrams showing (a) the elastic J/ψ production mechanism and (b) the dissociative J/ψ production mechanism. The colourless exchange object known as the pomeron has is indicated by* $\mathbb{P}$.

1.5.5 Diffractive J/ψ Production

Elastic J/ψ processes generally have associated low t values, suggesting a long range interaction such as pomeron exchange (see section 1.4). The VDM model described in section 1.5.3 relates the $\gamma p \to J/\psi p$ process to the $J/\psi p \to J/\psi p$ elastic scattering process. The latter process is a soft hadron-hadron collision which can be described through Regge theory by the exchange of the composite colourless object called the pomeron ($\mathbb{P}$) as described in section 1.4. Figure 1.8 shows the the diffractive mechanisms associated with 'quasi-elastic' J/ψ production. The term quasi-elastic is used to describe both elastic and dissociative events which heavily dominate the region $z > 0.95$.

1.5.6 Peturbative QCD J/ψ Production

Due to the hard scale of the process given by $M^2_{J/\psi}/4$, perturbative QCD methods should be applicable to J/ψ production and such models are often discussed in terms of what is known as the 'hard' pomeron. This is a model inspired by Ryskin [25, 26]

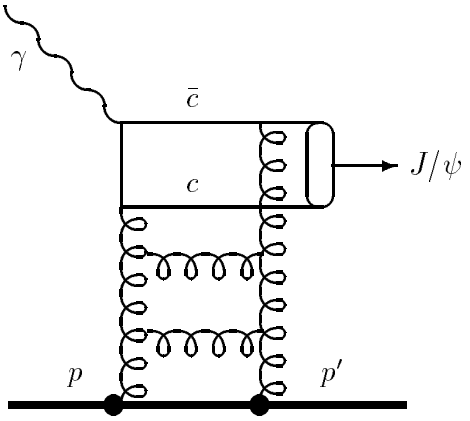

Figure 1.9: *Diagram illustrating diffractive production of J/ψ as described by the Ryskin Model.*

and suggests that the interaction between the proton and the $c\bar{c}$ pair arising from the photon is mediated by the exchange of a gluon ladder. This process is illustrated in figure 1.9. All non-perturbative effects are included in the gluon distribution of the proton and the value of which when squared is said to be proportional to the elastic cross section :

$$\sigma(\gamma p \to J/\psi p) \propto [xg(x)]^2 \tag{1.43}$$

with $x = M^2_{J/\psi}/W^2 \sim 10^{-3}$. The production of J/ψ mesons may therefore be sensitive to the gluon density of the proton. The energy dependence of the cross-section predicted by the Ryskin model differs from that of the Donnachie and Landshoff approach and is driven by the low-x behaviour of the gluon density within the proton. The gluon density is seen to increase sharply at low-x and the elastic J/ψ cross section correspondingly rises rapidly.

1.5.7 Results

As displayed in figure 1.10, results from HERA show a sharp rise of $\sigma(\gamma p \to J/\psi p)$ with energy $W_{\gamma p}$. The fit $\sigma(\gamma p \to J/\psi p) \sim W^{\delta}_{\gamma p}$ gives $\delta = 0.60 \pm 0.12$[8] (the solid line in figure 1.10). This is in strong contradiction with the soft pomeron exchange which

[8]Where $\delta = 4\lambda_2$.

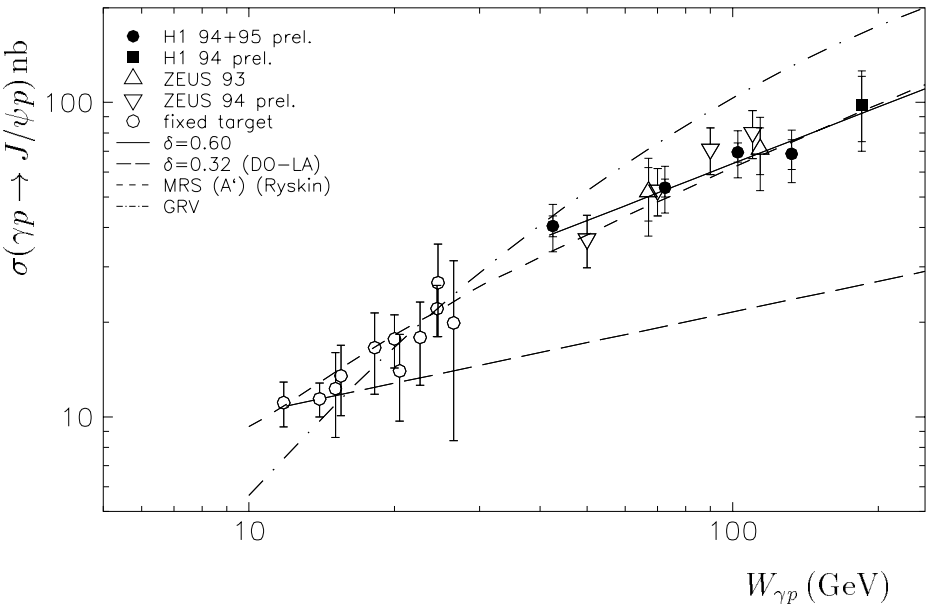

Figure 1.10: *The cross-sections $\sigma(\gamma p \to J/\psi p)$ measured at HERA (H1 [63] and Zeus [64]) and by fixed target experiments ($W_{\gamma p} < 30$ GeV). The prediction describing the nature of the exchange object as a 'soft' pomeron ($\delta = 0.32$) has been plotted. The 'hard' pomeron Ryskin model ($\delta = 0.6$) has also been plotted.*

predicts $0.22 \gtrsim \delta \gtrsim 0.32$ (the dashed line normalized to the fixed target data). The results are however in agreement with the hard pomeron concept with an intercept $\alpha_{I\!P}(0) \approx 1.2$, which corresponds to $\delta \approx 0.8$. The gluon ladder exchange model (diagram 1.9) and the Next to Leading Order (NLO) QCD modification [27] give a reasonable description of the data when the MRS(A′) parametrization of the gluon distribution in the proton [28] is used. The GRV parametrization [29] of the gluon distribution in the proton gives a slightly different prediction for $\sigma(\gamma p \to J/\psi p)$ and this has also been shown in figure 1.10. The sensitivity to the gluon distribution is illustrated by comparing the MRS and GRV parameterisations.

Chapter 2

The H1 Detector

2.1 The HERA accelerator

The electron-proton colliding beam facility HERA (**H**adron **E**lektron **R**ing **A**nlage) consists of two independent accelerators designed to accelerate and store 820 GeV protons and 27.5 GeV electrons (or positrons). The layout of the HERA accelerator can be seen in figure 2.1. Each of the electron and proton beams potentially consists of 210 bunches and have bunch crossing interval of 96 ns. These counter rotating beams are collided head on at two interaction points, the North and the South Halls, positioned around its 6.3 km circumference. The major detectors, H1 and ZEUS are located at these points respectively. The HERMES experiment is located at the East Hall and only uses the electron beam and the HERA-B experiment is located at the West Hall and only uses the proton beam. The design luminosity was set at 1.5×10^{31} cm^{-2} s^{-1} and in 1995 and 1996 average luminosity values of 2.3×10^{31} cm^{-2} s^{-1} and 2.64×10^{31} cm^{-2} s^{-1} were achieved.

2.2 The H1 Detector

The H1 detector is asymmetric in design because of the different requirements for detecting the hadronic fragments from the proton and recoil electron. Instrumentation for hadron detection is enhanced in the forward direction. The possible reactions

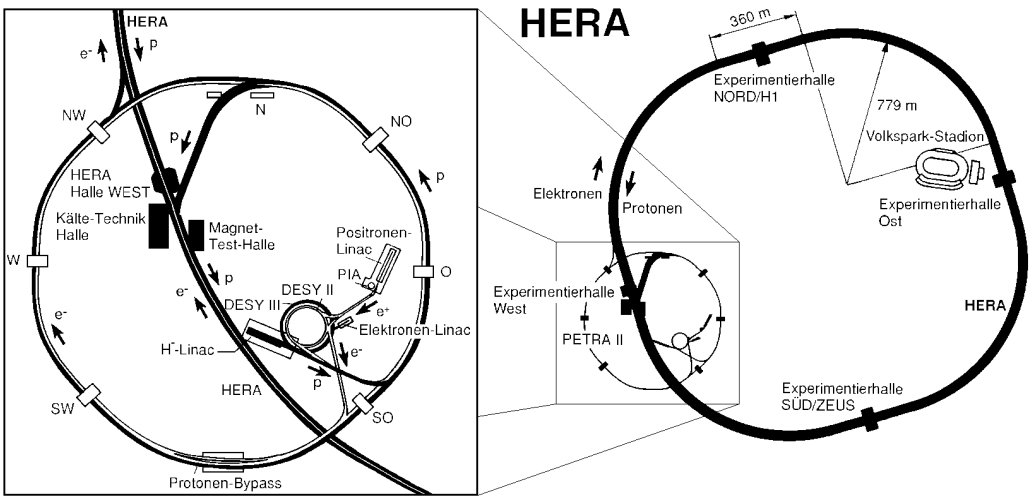

Figure 2.1: *The layout of the HERA accelerator situated at DESY, Hamburg. The H1 detector is located at the North Hall (Halle Nord).*

described in chapter 1 illustrate that the H1 detector is required to have good particle tracking and momentum measurement, calorimetry of high granularity, good energy resolution for jets and single electrons and good hermiticity to permit measurement of missing transverse energy. Only with these properties is it possible for the detector to record with adequate precision states that may contain several leptons accompanied by quark and gluon jets. Measurements of deep inelastic scattering processes make heavy demands on the calorimeter, particularly in measuring electron energies. In addition, charmed hadron spectroscopy, charmed quark tagging, electron identification and charged particle reconstruction within jets require a high-resolution, large solid angle tracking system. The efficiency of all these subdetectors can only be fully exploited with a sophisticated triggering system which has to be able to overcome the adverse background conditions which are associated with an electron-proton collider.

The layout of the H1 detector can be seen in figure 2.2. A right handed Cartesian coordinate system (x, y, z) and a spherical polar coordinate system (r, θ, ϕ) are used interchangeably. The direction of the proton beam is often referred to as the 'forward direction' (positive z-values relative to the center of the interaction region and $\theta =$

0), and vice versa to that of the electron beam as the ' backward region' (negative z and $\theta = \pi$).

The main components of the H1 detector are as follows:

- A tracking system consisting of the central and forward tracking detectors (CTD and FTD) which detect charged particles in the central region ($20° < \theta < 155°$) and the forward region ($7° < \theta < 25°$). These detectors consist of drift chambers interspersed with multi-wire proportional chambers to give fast signals for triggers using charged particles originating from the event vertex.

- A liquid argon calorimeter (LAr) which is designed to measure hadronic and electromagnetic energy flow. This surrounds the inner tracking system and is supplemented by the Spacal calorimeter in the backward direction. There is also a plug calorimeter which provides calorimetry close to the forward direction ($0.7° < \theta < 3.3°$).

- A superconducting coil and cryostat outside the hadronic calorimeter providing an almost uniform magnetic field of 1.15 Tesla over the central region and parallel to the HERA beams. This enables momenta values to be determined from the curvature of the tracks of charged particles.

- A set of iron plates surrounding all the major components of the H1 detector ($4° < \theta < 176°$). This iron return yoke of the magnet is instrumented to allow measurement of residual hadronic energy that penetrates beyond the liquid argon calorimeter and also to provide muon identification, triggering and tracking.

- A forward muon detector (FMD) which provides identification and the track reconstruction of muons in the angular range $3° < \theta < 18°$. It consists of a series of drift chambers positioned either side of a toroidal magnet which allows the momentum measurement of the track to be determined independently.

- Two electromagnetic calorimeters are situated downstream in the electron beam direction which tag electrons and photons for the purpose of luminosity

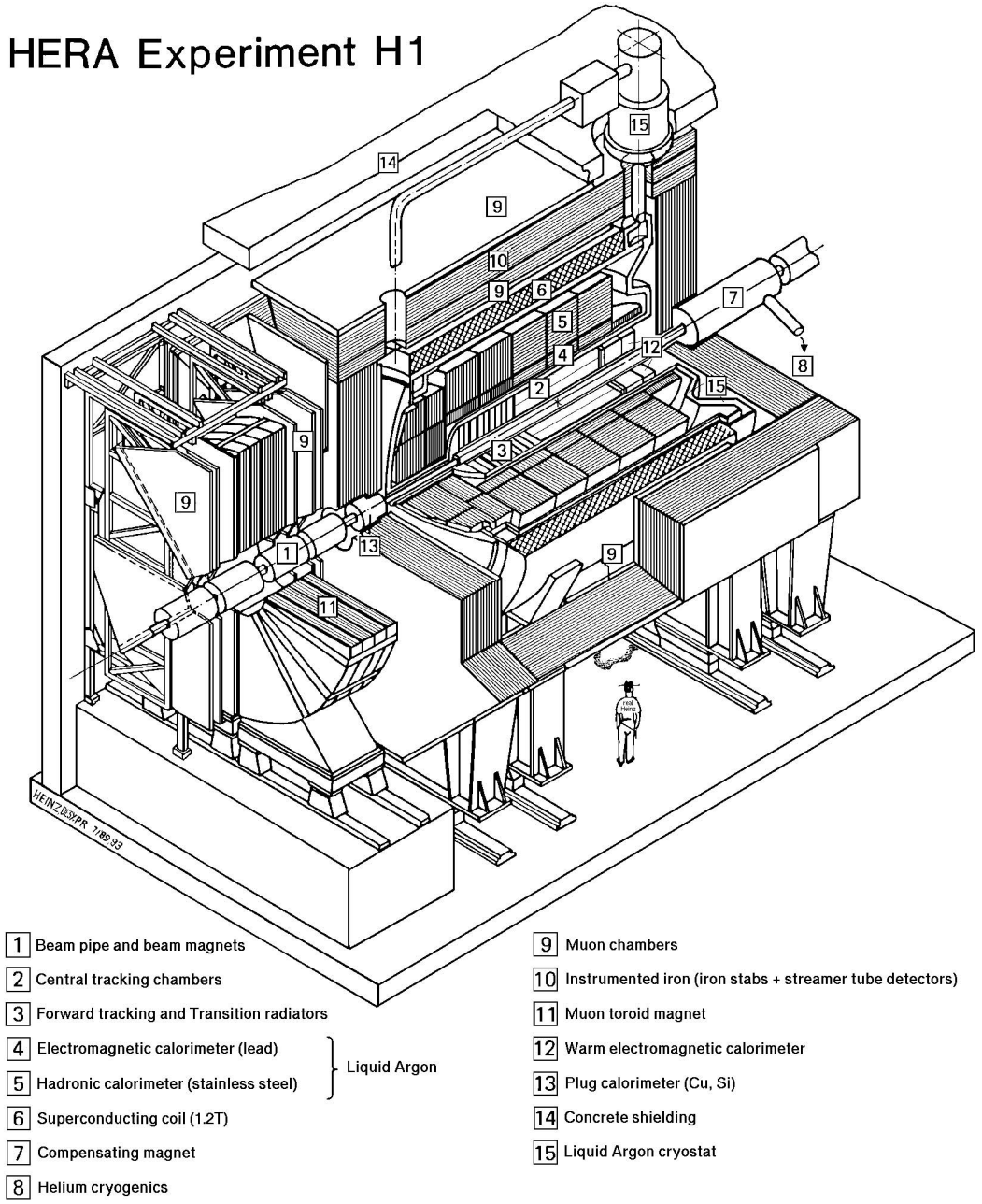

Figure 2.2: *A 3D view of the H1 detector.*

determination. They also detect a fraction of the scattered electrons from the photoproduction processes.

The rest of this chapter will be used to discuss in greater detail the aspects of the H1 Detector already mentioned above. Emphasis will be placed on the components which are of particular relevance to this study. A more extensive description of the H1 detector can be found in [30].

2.3 The H1 Tracking Detectors

The tracking system of H1 has been designed to reconstruct the tracks in jets with high particle densities and to measure the momentum and angles of scattered isolated charged particles to a precision of $\frac{\sigma_p}{p^2} \approx 3\times\ 10^{-3}$ GeV^{-1} and $\sigma_\theta \approx 1$ mr. Due to the large proton beam energy many charged hadrons are produced at a very low angles with respect to the incident proton beam direction. By contrast the recoil electrons are spread mainly over the backward and central region. Therefore there are two separate tracking detectors, the CTD and the FTD, the former with cylindrical chambers, the latter with radial and planar chambers perpendicular to the beam axis. Each is optimised for tracking and triggering in its angular region. The track momentum may be determined from the signals recorded in the drift chambers of the CTD and FTD while the multi-wire proportional chambers (MWPC's) provide triggering information. The particle identification may be improved by measuring the specific energy loss $\frac{dE}{dx}$ in the CTD drift chambers. A diagram illustrating a side view of the relative positions of the FTD and the CTD can be seen in figure 2.3.

2.3.1 The Central Tracking Detector

The CTD is made up of two large concentric drift chambers called the CJC1 and CJC2 (collectively the CJC). A side view of the CTD can be seen in figure 2.4. The CJC is a JADE [31] type jet chamber and has an inner radius of 200 mm, an outer radius of 795 mm and a length of 2640 mm centered about the nominal interaction point. The chambers have wires strung parallel to the beam axis (z-direction) with

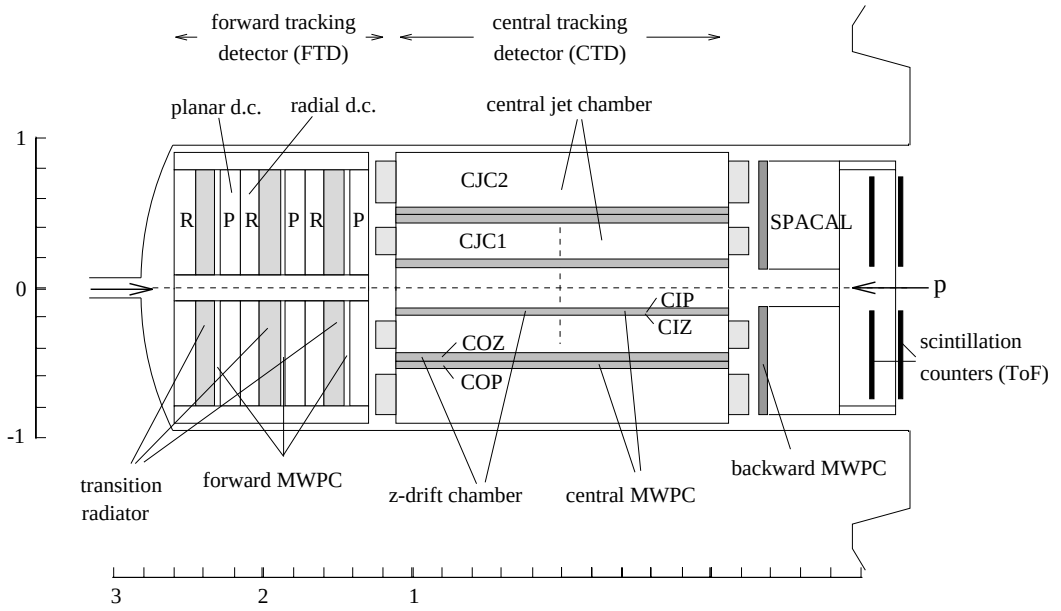

Figure 2.3: *A side view of the H1 tracking detectors illustrating the relative positions of the CTD and the FTD.*

the drift cells inclined with respect to the radial direction by approximately 30°. The effect of tilting is to improve the track resolution and also to remove detector 'holes'. This is particularly important for high momentum tracks ($p_T > 100\,\mathrm{MeV}$) which originate almost perpendicular to beam axis and would remain undetected if the cells were parallel to the radial direction. The ionization electrons produced by the primary particles drift in a direction which is almost perpendicular to the track. Left-right ambiguities in the drift direction are solved by linking together track segments from other cells. The $r\phi$ measurement of the CTD [32] has a resolution of $170\,\mu$m and, by comparing signals read out at both wire ends, a resolution of one percent of the wire length in z can be achieved (equivalently 22 mm).

Complementing the CJC measurement of charged track positions in z in the central chambers are made with the central inner and the central outer drift chambers (CIZ and COZ respectively). The CIZ chamber fits between the CJC1 and the beam pipe, while the COZ fits between CJC1 and CJC2. As seen in figure 2.4 the sense wires are strung tangentially to provide information on the z position of the track. These two chambers measure track elements with typically $300\,\mu$m resolution in z

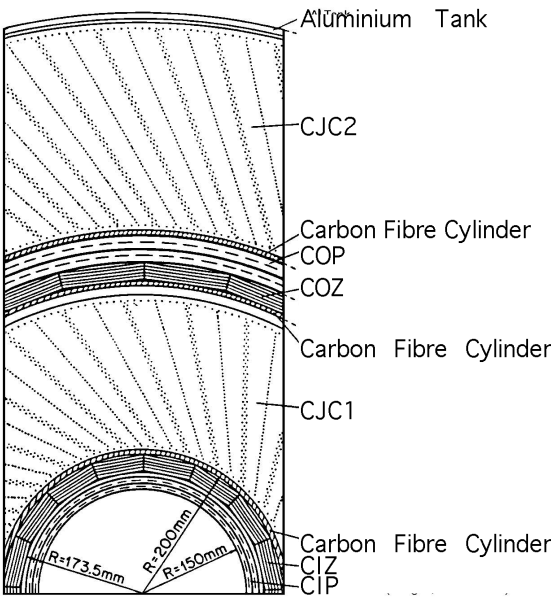

Figure 2.4: *A side view of the CTD. The 30° tilt of the drift cells can be seen for both the CJC1 and CJC2.*

and 1 to 2% of 2π in ϕ. Linking these track elements to those obtained from the CJC with accurate $r\phi$ and moderate z information gives the final accuracy on both the longitudinal as well as the transverse momentum components.

2.3.2 The Forward Tracking Detector (FTD)

The design objectives for the FTD was to provide an accurate measurement of the momentum of charged particles travelling within the angular range $5° < \theta < 30°$. The design momentum resolution for tracks with $p > 10\,\mathrm{GeV/c}$ and constrained by a point at the primary vertex is $\frac{\sigma_p}{p^2} < 0.003\ (\mathrm{GeV/c})^{-1}$, while the design track angular resolution is $\sigma_{\phi,\theta} < 1\,\mathrm{mrad}$ [42].

The detector consists of three identical sub-units known as 'Supermodules'. Each Supermodule, proceeding in the direction of the incoming proton, consists firstly of three layers of Planar drift chambers followed by a MWPC, then a transistion radiator material and finally a Radial drift chamber.

The Planar drift chambers are positioned at approximately 1.4, 1.8 and 2.2 m from the interaction point. Each module consists of 12 planes of wires and each

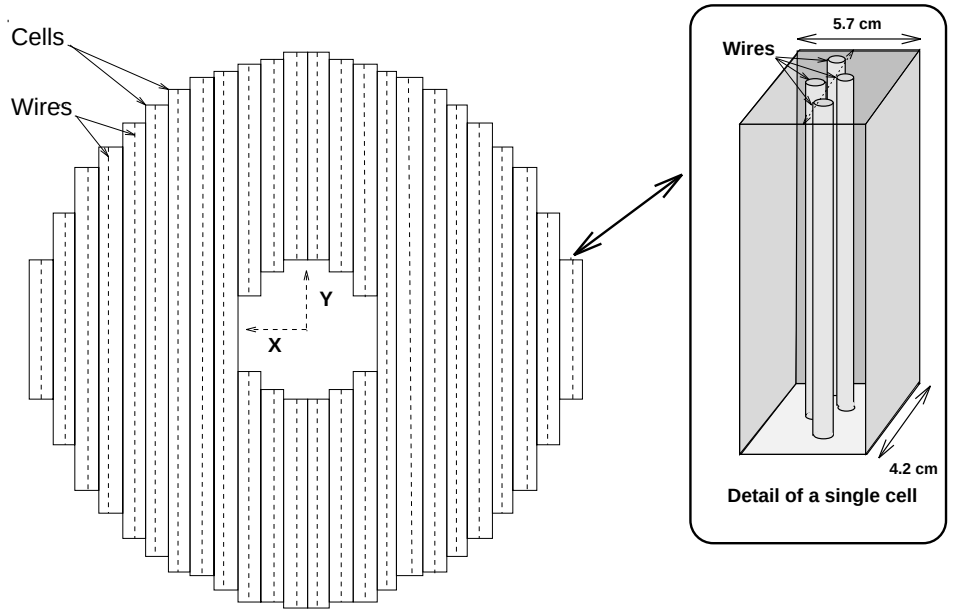

Figure 2.5: *The design structure of a Planar Drift Chamber, illustrating the structure of an individual cell.*

plane contains 32 parallel sense wires. These sense wires are only read out at one end and hence there is no knowledge of track position along the direction of the wire. The layers within a Planar chamber module are oriented at $0°, +60°$ and $-60°$ to the vertical, enabling the trajectory of a particle passing through the detector to be reconstructed well in both the radial and azimuthal directions. The structure of a Planar drift chamber is illustrated in figure 2.5. The Radial drift chambers are positioned at approximately 1.7, 2.1 and 2.5 m from the interaction point and consist of 48 wedge shaped segments. Each segment subtends 7.5° in ϕ and is equipped with 12 sense wires stacked in z. The Radial drift chambers are designed to make an accurate measurement of the azimuthal angle, together with a moderate measurement of the radial coordinate using charge divisions. The structure of a Radial drift chambers is illustrated in figure 2.6.

The resolutions are found to be 150-170 μm for single point spatial resolution and greater than 2 mm for double track resolution. The resolution achieved for the

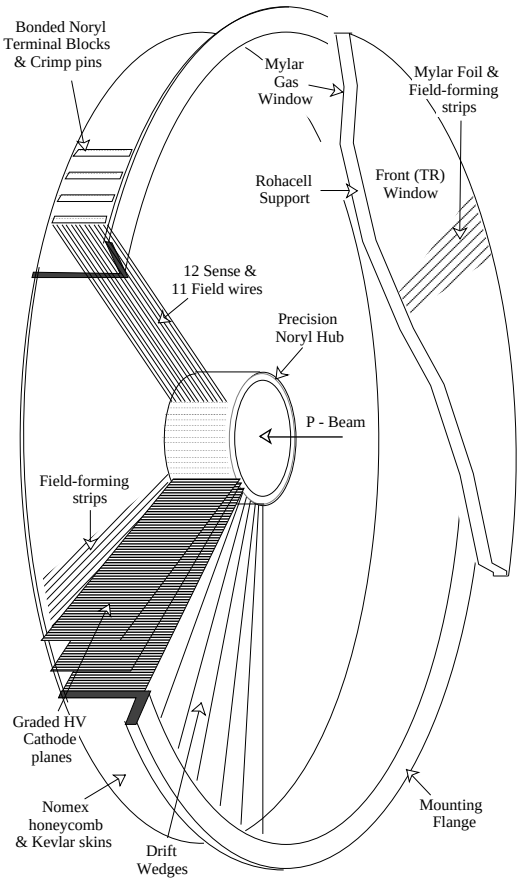

Figure 2.6: *The design structure of a Radial Drift Chamber.*

Radial drift chamber is 150-200 μm.

2.3.3 The Proportional Chambers

The multiwire proportional chambers cover the angular range $5° < \theta < 175°$. Six independent planes can be found in the forward direction and four in the central and backward direction. The three main functions of these chambers are :

- A fast timing signal is delivered which has a time resolution which is better than the separation between two succeeding HERA bunch crossings.
- To provide reasonably accurate charged particle space points for track reconstruction at the L1 trigger.

- Improve track reconstruction in the backward direction by providing an additional track element.

The different MWPC's are described as follows.

The Forward Proportional Chambers (FWPC)

The FWPC are found interspaced between the drift chambers of the FTD (described in section 2.3.2). The FWPC was designed to cope with the high particle multiplicities that can be found in the forward direction of the H1 detector. The volume and density of the material used to build the chambers was minimised to prevent secondary interactions and detection was increased close to the beam pipe.

Tracks crossing all three or at least two of the FWPC modules lie in the angular range $6.6° \leq \theta \leq 18°$ or $5.1° \leq \theta \leq 21.6°$ respectively. The timing resolution for such tracks have been measured to be 20 ns and 47 ns respectively. These values are well within the resolution required to separate two successive HERA bunch crossings.

The Central Proportional Chambers

Mounted adjacent to and inside the CIZ and the COZ (described in section 2.3.1) respectively are two multiwire proportional chambers called the CIP and the COP. The inner chamber (CIP) provides the greatest angular coverage as it is closest to the interaction region. The CIP and COP were constructed from low mass materials to reduce secondary particle interactions which may degrade the track reconstruction of the surrounding CJC drift chambers.

These chambers consist of a double layer of anode wires and are used to trigger on tracks coming from the vertex. Other information such as calorimeter and muon information may be validated using the chambers. The timing resolution for both chambers is approximately 21 ns.

The Backward Proportional Chambers (BWPC)

In the backward direction the reconstruction of the scattered electron in low Q^2 DIS events calls for an accurate track direction measurement. The Backward MWPC has

four anode wire planes orientated at 45° to each other which provide measurement of track segments. The Backward MWPC completes the trigger system for the tracking detector and also provides an additional space point for small angle tracks pointing in the backward direction. When requiring three out of four planes to be hit in coincidence with the BEMC an efficiency of 98 % is obtained.

2.4 The Calorimeters of H1

The task of the calorimeters is to measure the energy of all hadronic and electromagnetic particles emerging from the interaction point. The calorimeter modules have a sandwich construction with separate layers of absorbing material between sensitive detector regions. A particle passing through the calorimeter will interact with the material of the absorber, generating secondary particles which will themselves generate further particles. This continues such that a 'cascade' or 'shower' develops. The calorimeter then samples the development of a shower initiated by the incident particle. The total ionisation measured in the sensitive detector regions is closely proportional to the energy of the incident particle.

Detection and measurement of electrons together with very good performance in the measurement of jets with high energy particles requires the calorimeter to be inside the large coil providing the magnetic field. This minimises both the amount of dead material in front of the electromagnetic calorimeter and the overall size and weight of the calorimeter. A diagram illustrating the calorimetry system of H1 can be seen in figure 2.7.

2.4.1 The Liquid Argon Calorimeter

Liquid argon was chosen on the basis of the following advantages :

- The stability and ease of calibration.
- The fine granularity for $\frac{e}{\pi}$ separation and energy flow measurements.
- The homogeneity of response.

The liquid argon calorimeter (LAr) [33] covers the approximate polar angular range $4° < \theta < 154°$. It is segmented into a hadronic part and an electromagnetic part and is divided along the beam pipe into eight self supporting 'wheels'. Each of the six barrel wheels are segmented in ϕ into eight identical stacks or octants. The two forward wheels differ from the barrel wheels as they are assembled as two half rings.

The detection of electromagnetic particles relies on them generating showers in the material making up the electromagnetic part of the calorimeter. These showers develop through bremsstrahlung resulting from the charged particles (e^+, e^-) and pair production by photons. The absorber material in the electromagnetic part is lead and is between 20 and 30 radiation lengths $(X_\circ)$[1] thick.

The hadronic part of the calorimeter is similar in construction to the electromagnetic part, however the physical processes that cause the propagation of a hadron shower are considerably different. About half the incident hadron energy is passed on to additional fast secondaries and the remainder is consumed in multiparticle production of slow pions and other processes. The longitudinal development of hadronic showers is quantified by the nuclear absorption (or interaction) length, λ. The absorber material in the hadronic part of the calorimeter is over 5 to 8 interaction lengths (λ) and is made of 16 mm thick stainless steel plates with additional 3 mm steel in the read-out elements.

Studies have shown that the energy resolution $(\frac{\sigma_E}{E})$ of the LAC is approximately $\frac{12\%}{\sqrt{E}}$ (E in GeV) for the electromagnetic section and approximately $\frac{50\%}{\sqrt{E}}$ for the hadronic section (plus constant terms of 1 % and 2 % respectively).

2.4.2 SPACAL

The Spacal (**SPA**ghetti **CAL**orimeter) is the current calorimeter covering the backward region. The main task of this new calorimeter is to provide precise measurement of the scattered electron energy at low Q^2 and to improve the quality of hadronic energy measurements close to the electron beam direction. The electromag-

[1] $X_\circ$ is defined as the thickness of medium which reduces the mean energy of a beam of electrons by a factor of e.

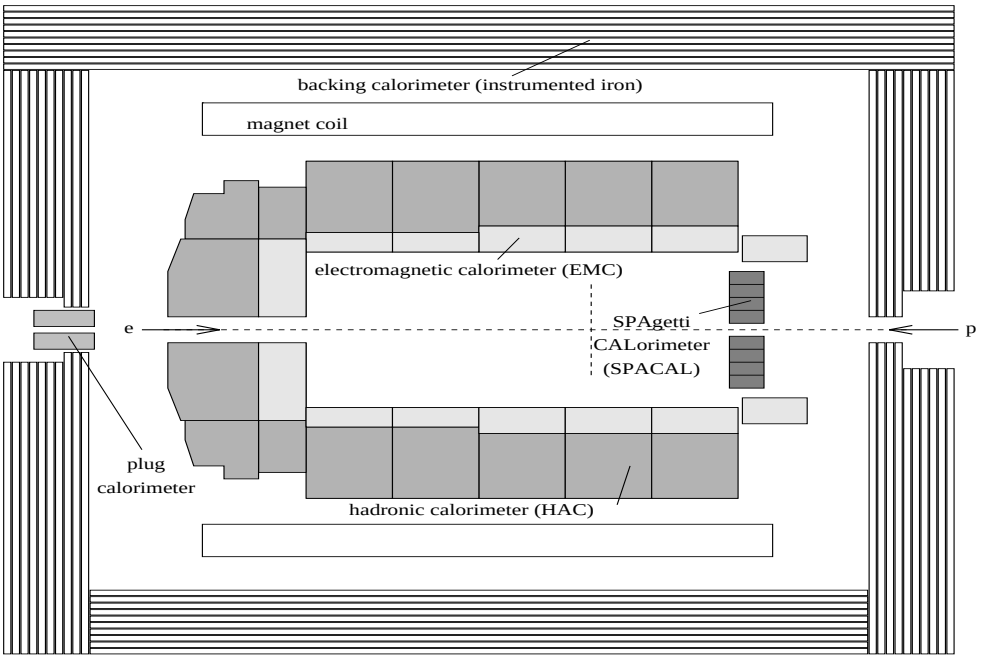

Figure 2.7: *The Calorimetry System of the H1 Detector.*

netic and hadronic sections have increased the angular ranges of particle detection to $\theta \leq 177.5°$ and $\theta \leq 178°$ respectively. Both of these sections consist of scintillating fibres inserted into a lead matrix. The absorber material in the electromagnetic part is approximately 27 radiation lengths thick and the absorber material in the hadronic part is approximately 1 interaction length thick.

Test beam studies have shown that the electromagnetic section has an energy resolution of approximately $\frac{7\,\%}{\sqrt{E}}$ (constant term of 1 %) [34] and the hadronic section has an energy resolution of approximately $\frac{56\,\%}{\sqrt{E}}$ for hadrons and $\frac{13\,\%}{\sqrt{E}}$ for electrons [35] (plus constant terms of 3 % and 3.6 % respectively).

2.4.3 The PLUG Calorimeter

The major aim of the PLUG calorimeter is to minimise the missing part of the total transverse momentum due to hadrons emitted at small angles to the proton direction. The PLUG signal is also useful to detect the presence of energy flow in the very forward region of the H1 detector ($0.6° < \theta < 3.5°$). The detector

itself consists of nine layers of copper absorber plates interleaved with eight layers of silicon detectors, and has a resolution of approximately $\frac{150\,\%}{\sqrt{E}}$ [36].

2.4.4 The Tail Catcher

The instrumented iron (which will be described in detail in section 2.5.1) consists of sixteen limited streamer tubes (LST) layers. Eleven of these tubes are equipped with readout electrodes which enable measurement of the leakage of hadronic energy from the LAr and Spacal. The energy resolution is estimated from test measurements at CERN [37] to be $\frac{100\,\%}{\sqrt{E}}$.

2.5 The Muon System

Two detectors form the H1 muon system. Firstly the instrumented iron of the return yoke of the magnet which detects muons emitted over a wide angular range ($6^\circ \geq \theta \geq 172^\circ$) and secondly the forward muon detector (FMD) which is situated in the forward direction after the forward iron end-cap (see figure 2.2). The FMD provides an independent momentum measurement and can be used in conjunction with the FTD. Muon identification provides information that is particularly useful for heavy flavour physics and the search for new and exotic particles.

2.5.1 The Instrumented Iron

The iron return yoke surrounding the major detector components of H1 is instrumented with limited streamer tubes. When closed, the iron yoke consists of flat end-caps terminating an octagonal barrel. Measurements made in the barrel region are defined by spherical polar coordinates (r, θ, ϕ) whereas the coordinates used in the end-caps are Cartesian (x, y, z).

A cross-sectional view through the instrumented iron is shown in figure 2.8. The iron yoke is segmented into 10 iron plates of 7.5 cm thickness and instrumented with 16 layers of LST. Five of these layers are equipped with strips perpendicular to the wire direction to measure the coordinate along the wire and the other 11 with

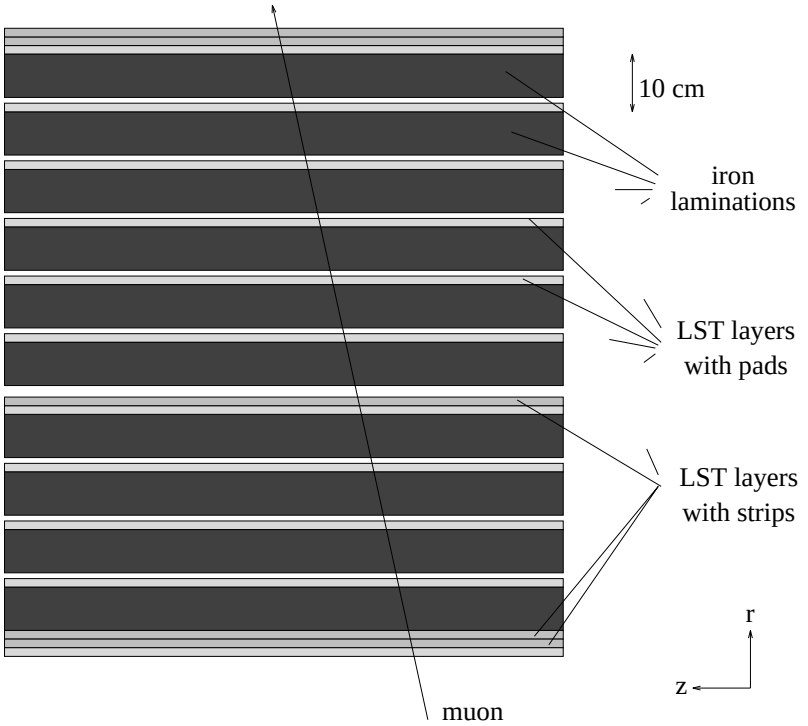

Figure 2.8: *A cross-sectional view through the instrumented iron, illustrating the 10 iron plates and 16 layers of limited streamer tubes (LST).*

large rectangular pads for a coarse energy measurement. Using the wire signals the position of a passing muon can be determined with a resolution of about 3-4 mm and the strips give a resolution of about 10-15 mm in the perpendicular direction. The pads provide a space-point with an accuracy of about 10 cm.

2.5.2 The Forward Muon Detector

The FMD [38] measures high energy muons in the angular range of approximately $6° \leq \theta \leq 18°$. The detector consists of six drift chamber planes mounted with three either side of a toroidal magnet. The toroidal magnet consists of eight solid iron modules built into mobile half-toroids for reasons of access. The inner radius of the toroid is 0.65 m, the outer radius 2.9 m, and the length between the flat faces 1.2 m. The field varies with radius, from 1.75 T at the inner radius to 1.5 T at the outer radius.

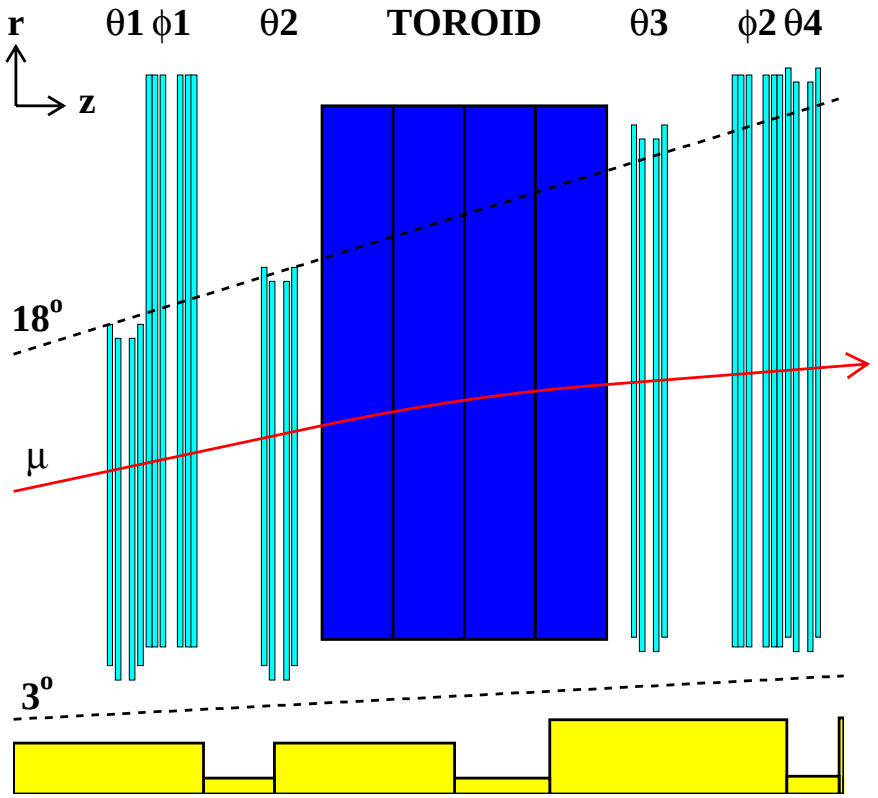

Figure 2.9: *A cross-sectional view of the forward muon system. The trajectory of a muon which has traversed the toroid is indicated by the solid line. The geometric acceptance at* 3° *and* 18° *is indicated by the dashed lines.*

The drift chamber planes cover a region which is about 4 m in diameter for the first detector plane and increases to cover a region 6 m in diameter for the last. These planes are all divided into octants supporting individual drift cells mounted on aluminium frames. The orientation of the drift cells is such that four of the planes measure the polar angle (the θ layers) and by measuring the track bending through the toroid the momentum of the particle can be determined. The remaining two planes measure the azimuthal angle (the ϕ layers). A diagram showing the positioning of the ϕ and θ layers of the FMD can be seen in figure 2.9. The individual octants from a θ and ϕ layer are illustrated in figures 2.10 and 2.11. Each θ and ϕ plane consists of a double layer of drift cells which are staggered by half a cell width. This arrangement enables the resolution of left-right ambiguities and the determi-

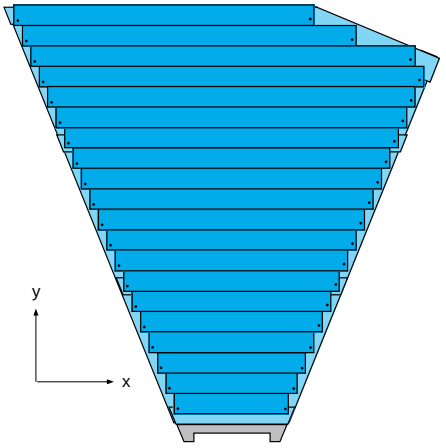

Figure 2.10: *A θ octant layer illustrating how the cells are mounted with the sense wires strung transversely in the xy plane.*

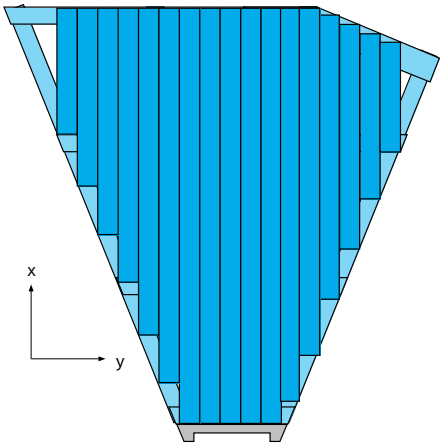

Figure 2.11: *A ϕ octant layer illustrating how the cells are mounted with the sense wires strung parallel to each other, and with the central wire strung radially outwards from z-axis.*

nation of 't-zero' which is the global timing offset for the detector. The momentum resolution ($\frac{\sigma_p}{p}$) is limited by the energy loss and multiple Coulomb scattering in the magnet iron. It is 22% at 5 GeV/c and deteriorates as the momentum increases.

All drift cells contain a central sense wire which at one end is connected to an adjacent cell by a 330 Ω resistor and at the other to a preamplifier. A determination of the track position in the xy plane transverse to the sense wire is made from the measurement of the drift time and a determination of the position along the wire by a charge division measurement. The charge division measurement along the wire is approximately accurate to 1% of the length of the sense wire.

The choice of gas filling for the drift chambers was based on several requirements. The gas used in the chambers should be fast enough for the pulse to arrive in time for the trigger and also non-inflammable for safety reasons. The gas mixture that is currently used in the chambers is 92.5%Argon, 5% Carbon Dioxide and 2.5% methane. The average field in a cell is approximately 0.48 kV cm^{-1} and causes the electrons to drift towards the central sense wire at a constant velocity. The central sense wire is kept at a higher voltage (4.2 kV) which induces amplification of the signal by the ionization avalanche around the wire. The resulting field is uniform over most of the cell so providing a constant drift velocity. Figure 2.5.2 shows a typical elastic J/ψ decay into a $\mu^+\mu^-$ pair where the muons are travelling forward with sufficient energy such that they have been reconstructed by the FMD.

2.6 The 'Down Stream' Forward Detectors

Several detectors are situated downstream (proton direction) in the beam pipe. The principal use of the detectors is to detect the final state or remnant of the proton. Two such systems that are designed for this are the Proton Remnant Tagger (PRT) and the Forward Proton Spectrometer (FPS).

The PRT surrounds the beam pipe at z=26 m and is comprised of layers of scintillator sandwiched between layers of lead shielding and read out by photo-multipliers. A diagram of the PRT can be seen in figure 2.13. The PRT detects

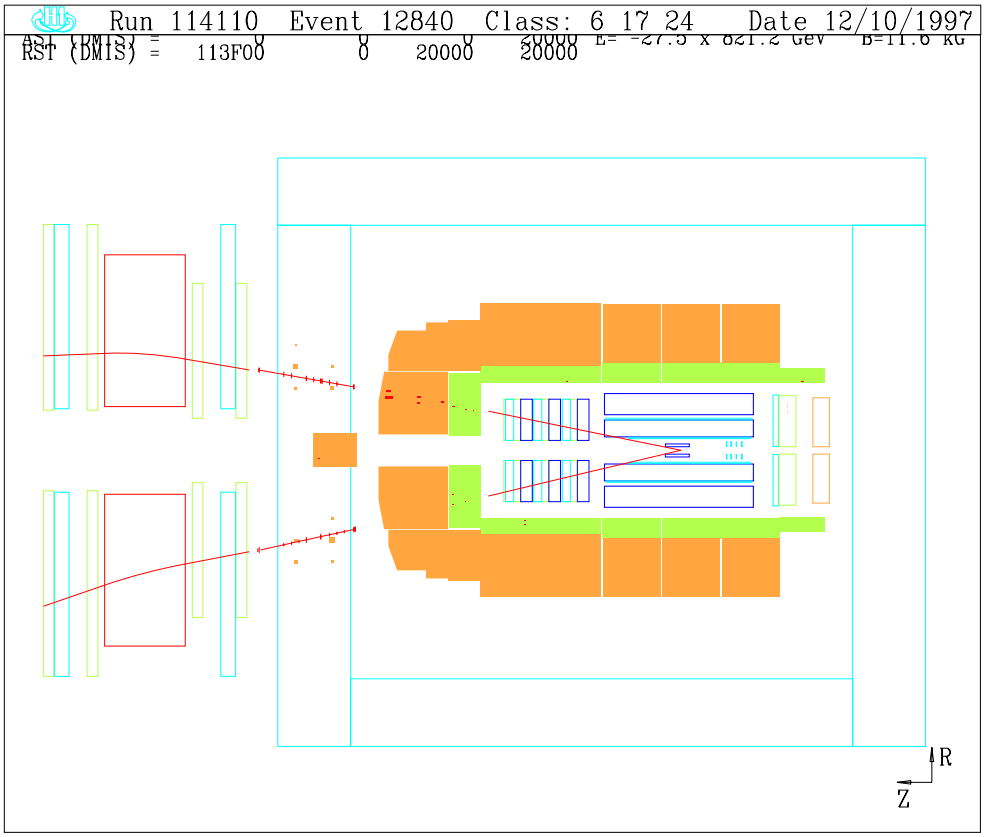

Figure 2.12: *An example of an event showing an elastic J/ψ decay to two muons which have both been detected and reconstructed by the FMD and forward iron end-cap. Energy deposition due to the muon can also be seen in the LAr.*

particles which originate from the fragmentation of the proton in the angular range $0.04° < \theta < 0.3°$. This detector is utilised when selecting elastic events through the event selection described in chapter 7.

The two stations of the FPS [39] are situated at z=81 m and z=90 m and are equipped with scintillating-fibre hodoscopes which provide space points on proton tracks. These points can be used to determine the curvature of the track and hence calculate the momentum of the proton.

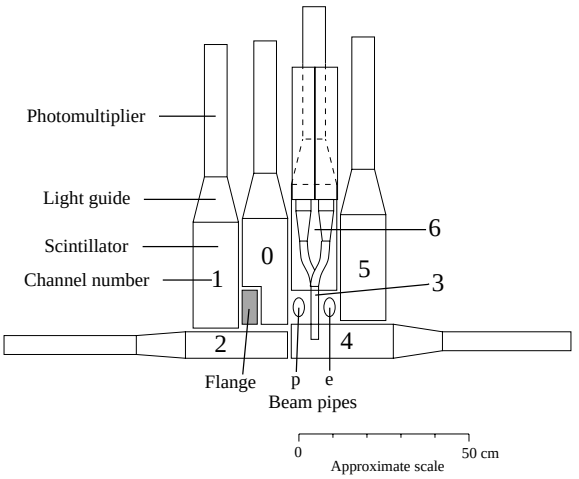

Figure 2.13: *The design structure of a Proton Remnant Tagger.*

2.7 Luminosity Monitoring

The luminosity system is designed to make off-line a fast relative luminosity measurement with a statistical precision of approximately 2% s^{-1} during nominal beam conditions [40]. It serves as a monitor to inform HERA of the electron beam condition and also determines an online luminosity measurement with an accuracy of approximately 5% s^{-1}. Is is also possible using the electron tagger (ET) to measure the energy of electrons scattered at small angles and together with the photon detector (PD) to detect Bethe-Heitler pairs required for luminosity measurements. The layout of the H1 luminosity system can be seen in figure 2.14.

The rate of the Bethe-Heitler reaction :

$$ep \longrightarrow ep\gamma \tag{2.1}$$

is precisely calculable in QED making it ideal for the determination of the luminosity. The luminosity is given by

$$Lumi = \frac{R_{tot} - (\frac{I_{tot}}{I_0})R_0}{\sigma_{vis}} \tag{2.2}$$

where R_{tot} is the total rate of the bremsstrahlung events, R_0 is the rate for the electron pilot bunches[2], I_{tot} and I_0 are the electron beam currents corresponding

[2]Electron pilot bunches are bunches which do not have a corresponding proton bunch when

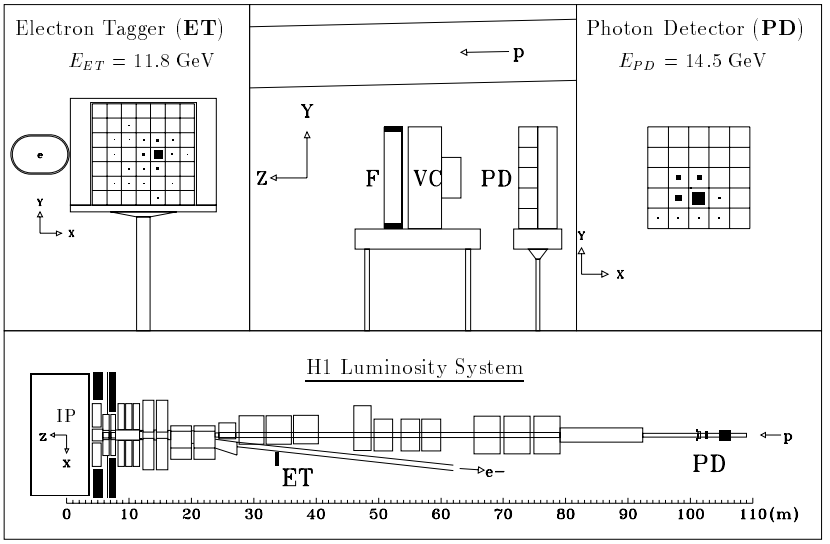

Figure 2.14: *A schematic diagram illustrating the layout of the H1 Luminosity System.*

to these rates and σ_{vis} is the visible part of the Bethe-Heitler cross-section with acceptance and trigger efficiency included. The on-line luminosity measurement makes use of electron and photon information detected in coincidence and a further off-line measurement is made using only the photon information to minimise the overall statistical error.

Further details of the determination of the luminosity at H1 can be found in [40]. Since the angular distributions for both the electrons and the photons from Bethe-Heitler events are strongly peaked along the direction of the electron beam the ET and the PD are positioned close to the beam pipe. The PD is situated at $z = -102.9\,\mathrm{m}$ and is protected from from the high synchrotron radiation flux by a water Čerenkov veto counter (VC) and a lead filter (F). The ET is situated at $z = -33.4\,\mathrm{m}$ and has an angular acceptance of $0 < \theta < 5\,\mathrm{mrad}$ accepting photoproduction events ($Q^2 < 0.01\,\mathrm{GeV}^2$) with electron energies such that $0.2 < \frac{E_{e'}}{E_e} < 0.8$.

Bremsstrahlung from the residual gas in the beam pipe ($eA \to eA\gamma$) is the main source of background and is expected to be 10% of the total $ep \to ep\gamma$ rate. It may

reaching the interaction region. They prove useful when estimating the amount of background resulting from the electron bunches.

be subtracted using data from electron pilot bunches.

2.8 Triggering

The high bunch crossing rates coupled with high beam background rates lead to the requirement of a sophisticated data acquisition system and trigger. Background event rates are several orders of magnitude higher than the 'interesting' physics event rate so it is important that these events are identified separately. The most important background processes are as follows :

- proton beam-gas interactions ;
- proton beam-wall interaction ;
- cosmic muons passing through the interaction point during beam crossings ;
- background tracks caused by beam halo muons and low energy photons or electrons from synchrotron radiation.

The data event selection is divided into five levels, the first four involving four levels of triggering of increasing sophistication : L1, L2, L3[3] and L4. The fifth level, L5, is where the full reconstruction of the data occurs and this will be described in detail in chapter 3.

The triggers at L1 [41] examine the information from the various subdetectors of H1 and select events satisfying any one of a number of pre-set combinations of conditions. These conditions are know as 'subtriggers' which are logical expressions with 'trigger elements' as arguments. Trigger elements are the digital information that are sent from the individual subdetector triggers to the Central Trigger. There are 128 different subtriggers available at L1 which are mainly designed to trigger on specific types of physics event. There are also subtriggers known as 'monitor triggers' which collect experimental data needed for example to measure the efficiency of a

[3]During 1995 running the L2 and the L3 processing systems were not in use. The L1 acceptance rate therefore had to meet the central data acquisition limitation of 50 Hz.

given detector. 'Cosmic triggers' collect cosmic ray events which may be used for calibration purposes.

The first selection procedure at L1 provides a decision for every bunch crossing. The event will be kept if any of the subtrigger conditions are satisfied. It is impossible to collect and process all the information needed to provide an efficient trigger decision between bunch crossings (96 ns) therefore, in order to make full use of the HERA luminosity, the L1 trigger operates in 'pipeline mode'. Pipelining is a method by which the information from up to 35 bunch crossings can be simultaneously stored so that the allowed processing time is extended. The 'latency' of the trigger, which is the delay between the time of the actual bunch crossing and when the L1 decision is produced, determines the number of steps in the pipeline. The detector is effectively disabled from the time when L1 decides to keep the event and the output has been sent to the central data acquisition. This period of disablement is known as the 'dead time' and is typically 1-2 ms per event. It is sometimes found that a subtrigger fires at a very high rate giving a large dead time and it must therefore be subjected to a prescale factor. This factor defines how often a particular subtrigger condition must be met before it contributes to the read out of an event. Physics triggers are generally not prescaled, however, monitor triggers which typically have high triggering rates have high prescale factors applied to them. A further requirement of the L1 trigger is that it must be able to carry out the procedure referred to as t-zero extraction. This means that it must be able to associate each selected interaction with an unique bunch crossing.

The L2 and L3 triggers are more sophisticated than L1. Decisions are made at these levels to reject unwanted events by a more refined analysis of trigger information. Analysis of a rejected event takes approximately 20 μs for L2 and 100 μs for L3. All the detector output from accepted events is passed on to the central data acquisition system so that the L4 decision can be made. L4 consists of a farm of computers with an overall processing capability currently of about 100 events per second.

Chapter 3

Track Reconstruction and Triggering

In order to devise a selection of tracks suitable for analysis purposes it is necessary to understand important aspects of the track reconstruction in the relevant subdetectors. The majority of the analysis described in succeeding chapters makes use primarily of the forward detectors covering the angular range $3° < \theta < 20°$, hence this chapter will describe the track reconstruction within the FTD, the FMD and the instrumented iron. Particular attention has been paid to the FMD reconstruction for which the track reconstruction efficiency has been determined in chapter 6.

It also is essential that the triggering of muons in the above angular range is well understood. The Forward Muon Trigger (FMT) will also be described in detail and the determination of its efficiency is also described in chapter 6.

3.1 Forward Track Reconstruction

The track reconstruction for the FTD is described in detail in [42]. As described in chapter 1, the Planar Supermodule consist of chambers mounted in three orientations, each of which is four wire planes deep in z (see figure 2.5). Readout is from one end of each wire only so that the positions along the wire are unmeasured. The path of the track through the chamber is approximately straight and hence

the information from the drift distances to the sense wires can be used to define a plane. Two orientations are required to define a line track segment, however, there are serious hodoscope ambiguities when several tracks are present and a third orientation is needed to eliminate these as far as possible. Successful reconstruction with a planar track segment that consists of at least three hits from each orientation (i.e. at least nine hits per planar track segment) is referred to as a 'primary' segment. Attempts are made to find additional track segments by relaxing the requirement on the number of hits to form what are called *secondary* and *tertiary* segments. Secondary segments have three hits in two orientations with only one or two hits in the third. Tertiary segments only have two hits in two of the three orientations.

Primary segments are obviously more reliable than secondary segments which are in turn more reliable than tertiary segments. Even if unattached to other segments the primary and secondary segments are treated as tracks, however, tertiary segments are only used to form a track when the track contains in addition either a primary, or a secondary planar segment. Forward track selection is based on the number of planar track segments and whether they are primary, secondary or tertiary.

Radial track segments are formed from at least six hits. Triplets of adjacent hits within a wedge are reconstructed and line segments produced by joining triplets which have shared hits with the same drift sign and for which the resulting group of hits lies on a straight line extrapolated between the first and last digitisation. Only the line segments with the largest number of hits is retained and multi hypotheses are rejected according to the χ^2 value obtained from a straight line fit to the combined triplets. This procedure only finds hits belonging to a track segment that lies entirely within one wedge and to extend the segment into nearby wedges the line segment must be extrapolated in ϕ. Planar tracks are favoured over radial so that radial segments are only retained if they can be verified by at least one planar track segment.

For events with high multiplicity in the forward direction both the efficiency of the track reconstruction and the track quality are seen to deteriorate. This can be

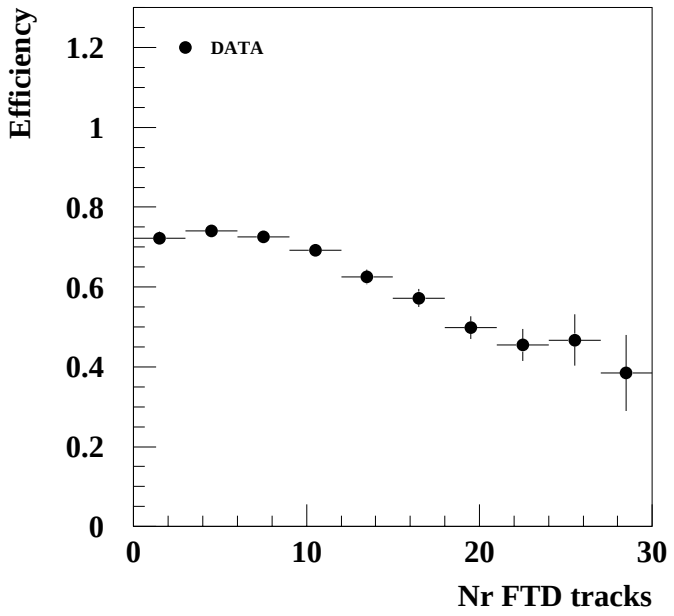

Figure 3.1: *Figure showing the track reconstruction efficiency of the FTD as a function of the total number of tracks reconstructed by the FTD for data.*

seen in figure 3.1 [43] which shows the track reconstruction efficiency of the FTD as a function of the total number of tracks found in the FTD for 1995 data passing the same selection criteria described in section 6.3.1. The deterioration in the efficiency is because a large fraction of the planar track segments that are reconstructed are due to false combinations of the three orientations. Rejection of these has been achieved by requiring that there are at least two linked planar track segments reconstructed. Low multiplicity events do not need such a requirement because the planar track segments are typically of a higher quality [42].

3.2 Instrumented Iron Track Reconstruction

The instrumented iron track reconstruction makes use of all the information available from the 16 wire, 5 strip and 11 pad layers (see figure 2.8). The spatial resolution is better for the wires (3-4 mm) so pattern recognition begins with them. The wires give a measurement defined as the 'wire plane' which is reconstructed from a maximum of 16 hits. The track segments are parameterized by straight lines, hence if curved

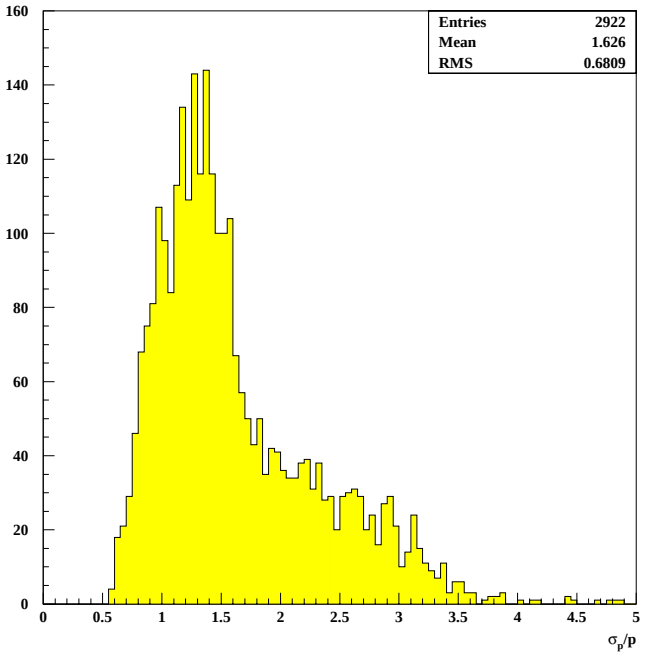

Figure 3.2: *The momentum resolution* ($\frac{\sigma_p}{p}$) *as measured by the Instrumented Iron.*

track candidates are to be reconstructed several track segments must be connected. The pattern recognition then selects track segments in the strip layers which give a measurement defined as the 'strip plane' which is perpendicular to the wire plane and can be reconstructed from a maximum of 3 hits. Track segments in the wires and strips are then combined to give a three dimensional track and any ambiguities are resolved by using the pad information. At least three wire layers are required to reconstruct a track. The fitting routine performs a least square fit simultaneously to wires and strips, using an average value for the magnetic field inside each of the iron plates. The energy loss in one plate averages 80 MeV and is accounted for by an iteration procedure.

In the barrel region, muons with energies below 2 GeV stop within the iron and in the forward direction end-cap the effective threshold is 2.5 GeV. The momentum of the muon causing the track can be estimated by using the field in the return yoke iron and the curvature of the track. However, it is not always possible to calculate the momentum of the track in the iron. Figure 3.2 shows a plot of the momentum resolution of the instrumented iron. The resolution is approximately 160% which

indicates how poor the momentum determination within the iron is. For this reason, the main use of the track reconstruction in the iron is to identify a reconstructed track in the FTD or CTD as a muon.

3.3 FMD Track Reconstruction

The FMD track reconstruction identifies the trajectory of muons and then associates a momentum value to each of them. Track reconstruction is a three step procedure [44] :

1. pairs are formed in a θ or ϕ layer using the hits found in each of the double planes of each octant ;

2. pairs in the θ_1 and θ_2 (θ_3 and θ_4) layers are linked to form track segments, before (after) the toroid. Information from the ϕ_1 and ϕ_2 layers is added at this stage ;

3. pre- and post- toroid track segments are linked together to form a track. The reconstructed momentum of the track is determined from the bending in the toroid.

3.3.1 Pair Finding

A cross section of cells mounted on an octant frame can be seen in figure 3.3. The cells of each plane are displaced from each other by half a cell width. This staggering of the cells helps to resolve the 'left-right' ambiguity in the drift coordinate for a pair of hits. An angular cut of $\pm 45°$ is made in the drift coordinate to select pairs and to remove ambiguities as shown in figure 3.3. Unpaired single hits are also kept and both they and the segments are considered in the track segment reconstruction.

3.3.2 Track Segment Reconstruction

The previously found pairs (and single hits) are now linked to make track segments between the two θ layers (see figure 2.9) either θ_1 and θ_2 or θ_3 and θ_4. Pre-toroid

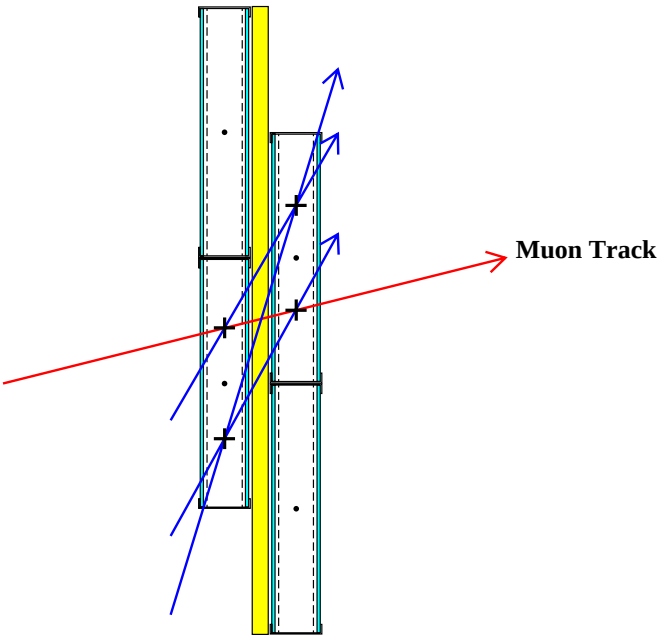

Figure 3.3: *A cross-sectional view through cells found in the FMD. Possible pair configurations have been shown by the arrows which link hits in each cell.*

track segment reconstruction[1] begins by choosing a pair of hits (or a single hit) in an octant of layer θ_1 and any pair of hits (or a single hit) in the same octant of layer θ_2. A minimum requirement of one pair is made when reconstructing the track segment. A straight line fit is made and a χ^2 value determined by using both the drift and charge division information. Track segments are only kept if $\chi^2/\mathrm{NDF} < 100$ in both x and y, where NDF stands for the number of degrees of freedom. Figure 3.4 shows a track segment that has been reconstructed.

If a pair of hits or single hit in the ϕ layer is found to be associated with a track segment of the θ layers then the previously defined track segment is refitted to give a new χ^2/NDF value. Again this is subjected to the same χ^2/NDF cut. A track segment is fully reconstructed when the fit is made to all the points that have been found in each of the two θ chambers and the intermediate ϕ chambers.

[1]Post-toroid track segment reconstruction is identical except that θ_3 and θ_4 are treated in place of θ_2 and θ_1.

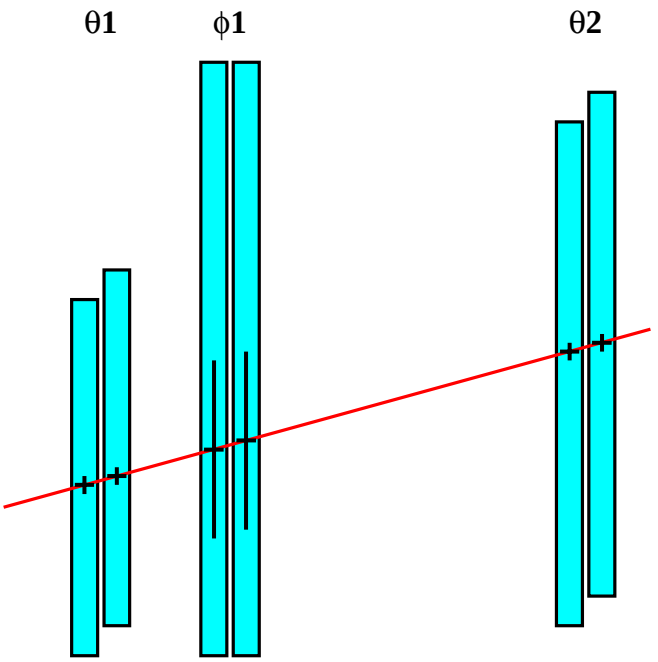

Figure 3.4: *A cross-sectional view of the pre-toroid layers which are part of the FMD. The segment finding procedure is shown which involves linking pairs (or hits) found in the θ layers. A pair (or hit) has also been found in the intermediate ϕ layer thus providing additional track information.*

3.3.3 Pre- and Post-toroid Track Segment Linking

A full muon track is obtained by linking together a pre-toroid track segment and a post-toroid track segment. A first step is to extrapolate the track segments to the central plane of the toroid. The difference in both r and θ at this plane between each pre-toroid and each post-toroid extrapolated track segment is determined. Only extrapolated track segments that have agreement with $\delta\phi < 30°$ and $\delta r < 20\,\text{cm}$ at the center plane of the toroid are retained for the full track linking.

Each track segment is assigned 52 possible momentum values and for every value an extrapolation through the toroid is made. Figure 3.5 illustrates how the track segment may be extrapolated through the toroid. In following the path of the muon

through the toroid the energy loss and bending of the muon trajectory due to the magnetic field are taken into account. The post-toroid track segments are then fitted to every exit point of the extrapolated track segments and a χ^2 value is determined for each pair of segments. A plot of χ^2 as a function of momentum is built up and the momentum value with the smallest associated χ^2 is taken as an estimate of the momentum of the muon on entering the toroid. If there is no momentum value with a χ^2 below a pre-set threshold then the pair of track segments are not linked.

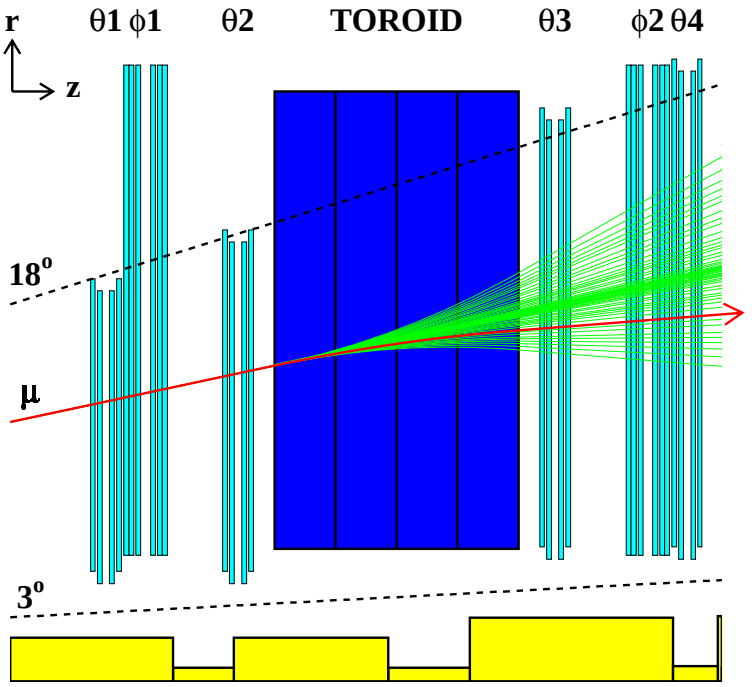

Figure 3.5: *A cross-sectional view of the pre-toroid layers found in the FMD. The track finding procedure involves extrapolating the pre-toroid track segment through the toroid and linking it with a post-toroid track segment. The extrapolation hypotheses for a muon track have been shown.*

Further improvement is made to the value determined for the momentum by fitting a quadratic function to the minimum in the χ^2 distribution versus the momentum. The fit uses the smallest χ^2 value and the two adjacent χ^2 values. The minimum of this function is the momentum which is finally taken and the second derivative at the minimum is used to make an estimate of the uncertainty of the

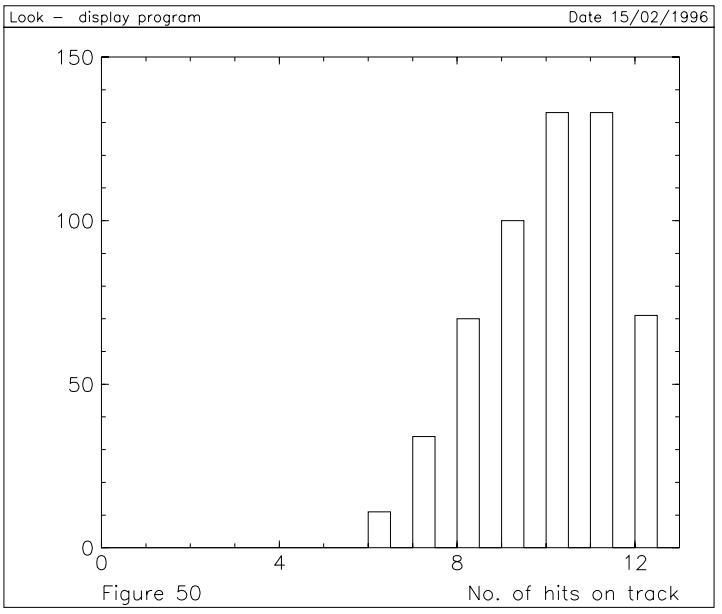

Figure 3.6: *A L5 histogram illustrating the number of hits typically detected by the FMD.*

reconstructed momentum.

A muon quality parameter is also defined which is dependent on the type of minimum that is found. This parameter can have the values 1 to 5 which are set as follows :

1 = A minimum found where χ^2 is determined using available x, y[2], θ, ϕ information.

2 = A minimum found where χ^2 is determined using only θ and ϕ information.

3 = A minimum found where χ^2 is determined using only x and y information.

4 = A minimum found, however the track exits the toroid so the momentum measurement is unreliable.

5 = A minimum found at the lowest momentum value of the scan. This gives an inaccurate momentum measurement (no minimum), but the charge is normally correct.

[2]These coordinates refer to the internal FMD x, y coorodinates determined from charge division.

The above procedure is repeated for every pair of pre- and post-toroid track segments. If a single track segment is found to be part of two or more reconstructed tracks then only the track with the lowest muon quality value or lowest χ^2 value associated with it will be kept. The track segment will only be used in one fit (the best) and any other track fits which it is involved in are rejected.

A fully reconstructed track will have between 6 and 12 hits, where there are a maximum of two hits in each of the double layers. Figure 3.6 shows a L5 histogram of the distribution of the number of hits detected per track in the FMD.

3.4 Forward Muon Trigger

The events selected in chapter 7 are triggered by the subtriggers described in tables 7.1 and 7.2. Subtrigger 16 is partly constructed from the trigger element *FwdMu_Val_Any* and subtrigger 28 is constructed from the trigger element *FwdMu_Val_Multi*. These trigger elements correspond to the Forward Muon Trigger (FMT)[3]. The efficiency of these FMT trigger elements have been determined in chapter 6 so a description of the FMT to signal the presence of a muon candidate in the FMD is given in this section.

3.4.1 The Design Philosophy of the FMT

The aim of the FMT is to trigger on events with a forward muon. The main requirement is that a track which points back to the interaction vertex is detected in the FMD. The pointing requirement is imposed for pre-toroid track segments and also for post-toroid track segments separately. The pre-toroidal tracks have undergone multiple Coulomb scattering when passing through the LAr calorimeter and iron end-cap and the post-toroid tracks have undergone further such scattering in the toroidal iron. Hence, the accuracy at which the track points back to the vertex is degraded (more so for post-toroid tracks).

[3]As described later in table 3.1 the trigger element $FwdMu\_Val\_Any$ and $FwdMu\_Val\_Multi$ are defined as the trigger elements 0 and 3 of the FMT.

The inputs to the trigger come from the drift chambers in the θ layers of the FMD. These have a maximum drift length of 6 cm with a corresponding maximum drift time of 1.2 μs. As described in chapter 2, these cells have a staggered configuration (figure 3.3) making it possible to extract the time at which a particle traversed the chambers to better than one HERA bunch-crossing period of 96 ns.

Particles which have penetrated the iron end-cap and have entered the FMD will be mainly muons, many of which originate from heavy-quark production processes. However, some of these particles may not originate from the electron-proton collisions and constitute background processes which must be rejected. Typical sources of background events have been outlined in chapter 2. The requirement that a track must point back to the nominal interaction vertex removes a substantial fraction of such background tracks.

The logical steps taken by the FMT are shown in figure 3.7. A brief overview of these steps will be given here but a more detailed account can be found in [45]. The trigger only recognises tracks that travel in the same octant through all the θ layers. It does not recognise tracks which cross from one octant to another. The input information to the trigger are hits from the linked drift cells. These signals pass through three distinct modules during their processing by the FMT :

- the Discriminator Module (DM) ;
- the Road Finder Module (RFM) ;
- the Final Decision Module (FDM).

These modules are indicated by the shaded areas in figure 3.7.

The Discriminator Module

The DM detects hits due to charged tracks in the chain of analogue pulses that are sent from the drift cells. Hits are found by determining whether a pulse height rises above a programmable threshold value. These pulses are then digitised and synchronised to the internal H1 clock. Since the cells are coupled by a linking resistor

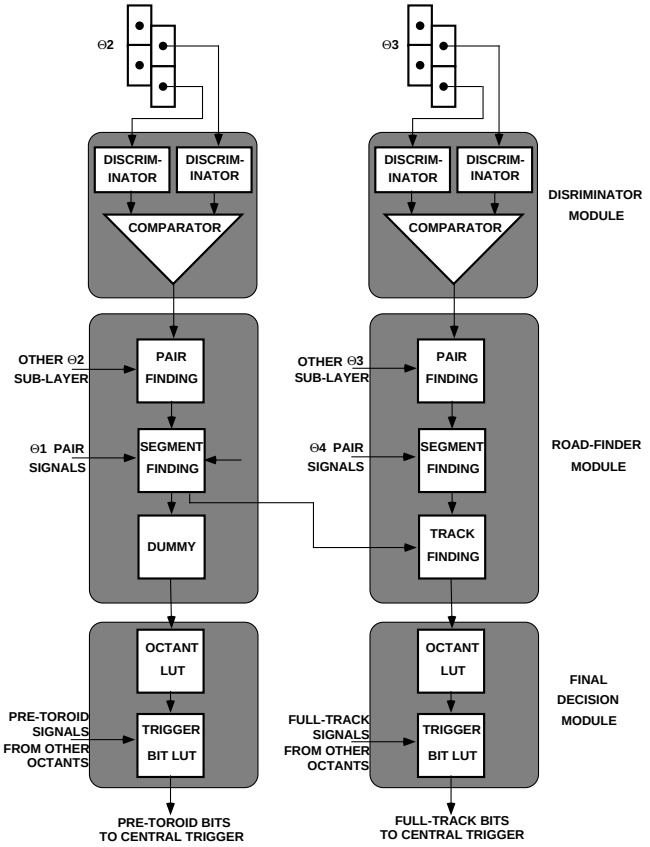

Figure 3.7: *A block diagram of the FMT illustrating the logical steps that are made when deciding on whether a muon has triggered the event.*

of 330Ω it is possible to identify which of the two linked cells was struck from pulse heights seen at the two ends. A comparator samples the amplitude of the pulses on the two wires and allocates the hit to the wire which has the bigger amplitude. After identifying a hit the discriminator is effectively disabled until the next bunch crossing so as to avoid double strobing from messy pulses. The final output of the DM's are 48 ns digital signals which correspond to hits. These provide input for the RFM's.

The Road Finder Module (RFM)

These modules have three main tasks :

1. the extraction of t-zero for pairs of wire signals ;

2. track finding in θ_1 and θ_2 or θ_3 and θ_4 ;

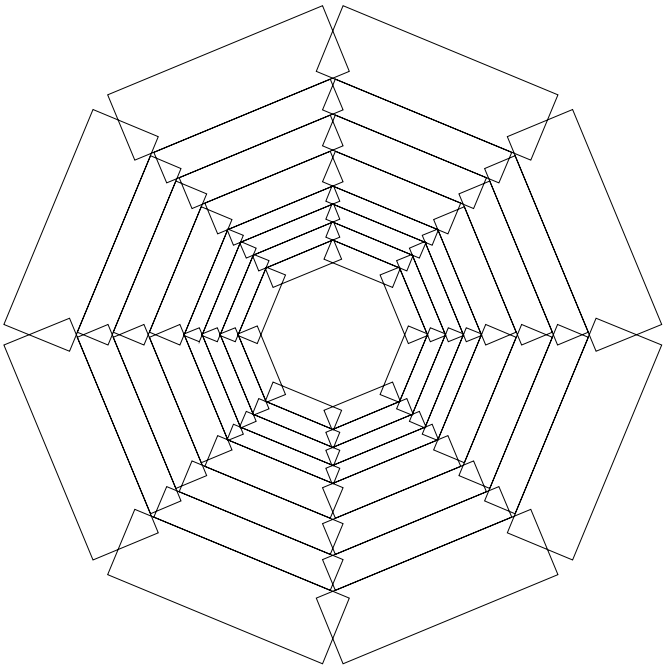

Figure 3.8: *An 8 × 8 rφ bit map of a θ layer of the FMD.*

3. correlating tracks pre- and post-toroid.

The t-zero value for each pair of cells is extracted by field programmable Application Specific Integrated Circuits (ASIC's) which are known as the t-zero chips. These chips look for pairs of hits (assuming that they point to the H1 vertex) and determine the position of the pair and the event bunch crossing that they originated from. The output from this gives the drift coordinate for the pair of signals, with a resolution of 2 mm.

After pairs of hits have been found, the next stage is to identify and associate pre- and post-toroid track segments. This association is made by a set of field programmable ASIC's known as the 'track finding' chips (4 chips per RFM). The segment finding procedure can be configured to require that at least three out of four hits per track segment or four hits per track segment. The output from the track finding chips is in the form of a 32 bit map of each octant which describes the position of the track in the drift chamber plane θ_2 for pre-toroid and in θ_3 for post-toroid tracks. This output then forms the input into a set of ASIC's known as

TRIGGER ELEMENT	DEFINITION
0	Any single muon validated tracks (pre- and post-toroid).
1	A dimuon pair found in opposite octants.
2	More than one validated track found in the same octant
3	More than one validated track found in different octants.

Table 3.1: *The four trigger elements that correspond to fully validated tracks. Trigger element 0 and 3 are important to the analysis described in chapter 7 and are defined as $FwdMu\_Val\_Any$ and $FwdMu\_Val\_Multi$ respectively.*

the *correlator* chips.

The correlator chips matches pre- and post-toroid track segments to find fully validated tracks. They can also introduce a momentum cut by correlating only pre- and post toroid track segments which, when traversing the toroid, have a track bending angle within a programmable preset value.

The output from the correlator chips in the RFM is essentially information (r and ϕ coordinates) about the positions of the validated tracks in the θ_2 layer of the FMD. The outputs to the FDM are the validated tracks as found by the correlators and the pre-toroid information retained from the track finding stage.

This output is in the form of two 8×8 $r\phi$ bit maps as shown in figure 3.8, one corresponding to pre-toroid tracks and one corresponding to validated tracks. The boxed regions represent one bit and each octant is separated into 8 bits.

The Final Decision Module (FDM)

The FDM processes the two 8×8 $r\phi$ bit maps according to the multiplicities and topologies of the tracks found in the FMD. The output consists of 4 bits each for pre-toroid and full tracks referred to as trigger elements. These eight trigger elements are then sent to the central trigger. At present the four trigger elements that correspond to full validated tracks are defined as shown in table 3.1.

Chapter 4

Event Selection

The previous chapter described in detail the track reconstruction performed by the FTD, the FMD and the instrumented iron. The next step is to select 'good' tracks which pass a set of track cuts that are described in this chapter. These cuts are designed to minimise background and to impose a track selection which is suitable for the dimuon analysis in chapter 7.

4.1 Event Classification

Reconstructed data events are stored on 'production output' tapes (POT's). The stored data include both events of interest and background events. An essential step is to classify each event so that those of interest can then be written to data summary tapes (DST's). There are 32 different event classes and the events in which a J/ψ meson decays into a muon pair are found in Class 24; the class which contains events with at least one good inclusive muon (or electron). Class 24 is defined by a track selection which is split into two categories depending on whether the electron or muon decay channel is to be analysed. The following sections describe the cuts used to define Class 24 events[1] which contain an identified muon.

[1]The inner track cuts are common to both event class category i.e. muons or electrons

4.1.1 Inner Track Cuts

Inner tracks are vertex fitted tracks reconstructed by the FTD or the CTD.

CTD Track Cuts

A 'good' quality CTD track is defined by the following cuts :

- $p \geq 0.8\,\mathrm{GeV/c}$.
- The minimum number of hits allowed to reconstruct a track = 10.
- $R^{start} \leq 30\,\mathrm{cm}$. This variable is the radius at the start of the track.
- $z_{\circ} \leq 40\,\mathrm{cm}$. This variable is the z value measured at the distance of closest approach to the vertex.
- The maximum fraction of unused hits per track = 0.3.

FTD Track Cuts

A 'good' quality FTD track is defined by the following cuts :

- $\chi^2_{vertex} \leq 20$. This variable indicates the compatibility of the track with the vertex. A large χ^2_{vertex} gives a low probability that the track originates from the vertex.
- $\chi^2_{track}/\mathrm{NDF} \leq 10$. This variable indicates whether the hits used to reconstruct the track actually belong to the track. The number of degrees of freedom (NDF) is also included because long tracks can be expected to have larger χ^2_{track} values hence dividing by NDF means that tracks of all lengths maybe compared.
- $p \geq 1.0\,\mathrm{GeV/c}$.
- Number of Planar Supermodules segments ≥ 1.

- For tracks in the angular region of $\theta \leq 20°$ the total sum of the number of Planar Supermodules + Radial Supermodules segments ≥ 2.
- $z_\circ \leq 40\,\mathrm{cm}$.
- $R_0 \leq 5.0\,\mathrm{cm}$. This is the radial distance of a non-vertex fitted track at the vertex.

4.1.2 Outer Track Cuts

Outer tracks are identified muon tracks reconstructed by the instrumented iron or FMD.

Iron Track Cuts

These cuts are dependent on whether the track is found in the iron barrel or the iron end-cap. The following cuts are made on the tracks in the barrel :

- The number of the first wire layer recording a hit ≤ 5.
- The number of layers with recorded hits ≥ 2.
- $z_\circ \leq 100\,\mathrm{cm}$.

The cuts made on the iron tracks in the end-cap region are as follows :

- The number of layers with recorded hits in the forward end-cap ≥ 6.
- The number of layers with recorded hits in the backward end-cap ≥ 3.
- The number of the first wire layer recording a hit ≤ 8.

A further cut, which is common to barrel and iron-cap iron tracks, is the requirement that the nearest point to the beam axis of the iron track, when extrapolated back to the vertex position, falls within a 100 cm region around the nominal vertex.

Calorimeter Muons

- If there is only one calorimeter muon detected the muon quality [48] ≥ 2.
- If there are two calorimeter muons detected the combined muon quality ≥ 5.

FMD Track Cuts

- The intersection of the pre-toroid track segment with the z axis in the rz plane must lie between -400 cm and 300 cm.
- The FMD muon quality ≤ 2.

4.2 Track Selection

Events that pass the Class 24 classification create a greatly reduced subsample of dimuon events which need to be analysed further. An additional track selection [47] is then applied to these events in order to collect a final sample which are reliably described and can hence be used for the analysis described in chapter 7. This track selection has two main objectives: the removal of 'bad' tracks and the removal of unwanted hypotheses.

Again the selections for 'inner tracks' and 'outer tracks' have been made separately.

4.2.1 Removal of 'Bad' Inner Tracks

A track may be reconstructed both in the CTD and in the FTD if it lies in the angular range $16° < \theta < 25°$. The reconstruction program uses these two track segments to give a better determined track trajectory which is known as a 'combined' track. A track is only accepted if it passes all the cuts specific to the track type. Combined tracks use FTD and CTD track segments so the track cuts applied are essentially an amalgamation of those for CTD and FTD tracks.

Central Track Cuts

- $20° \leq \theta \leq 160°$;
- $p_T \geq 150\,\mathrm{MeV/c}$;
- Track Length $\geq 10\,\mathrm{cm}$ ($\theta \leq 150°$) ;
- Track Length $\geq 5\,\mathrm{cm}$ ($\theta \geq 150°$) ;
- $R^{start} \leq 50\,\mathrm{cm}$;
- $|\,\mathrm{DCA}'\,| \leq 2\,\mathrm{cm}$;
- 'Double' Tracks removed.

Low momentum tracks suffer a large amount of multiple scattering in the material between the subdetectors, mainly coming from the end wall of the CJC. This leads to difficulties when fitting hits to reconstruct a track. Imposing a minimum p_T cut (or equivalently the p cut described for the Class 24 selection) removes these tracks. The central track selection also makes use of a variable called DCA′ which is the corrected 'distance of closest approach' (DCA). The DCA is the perpendicular distance between the track and the event vertex at the point of closest approach to the vertex. The DCA is measured using the nominal event vertex at the coordinates (0,0), however the corrected DCA (DCA′) uses the actual reconstructed vertex position in the xy plane. A radial track length is defined as R^{stop} - R^{start}, where R^{start} is the radius value at the start of the track and R^{stop} is the radius value at the end of the track. The track length obviously depends on polar angle. Tracks which have $\theta \geq 150°$ are relatively short because the angular acceptance of the CTD has a maximum of 160° and for these the track length requirement is reduced to 5 cm.

In some instances two tracks detected in the CTD are in fact two segments of the same physical track. This effect occurs for at least 12% of all events on DST [46] and to prevent double counting one of the tracks must be rejected. This is done by comparing p_T, θ and ϕ of the tracks and making sure that they lie in different radial

regions. Cuts are made on these variables to ensure that the best track of the two is kept.

Forward Track Cuts

- $p_T \geq 150\,\mathrm{MeV/c}$;
- $6^\circ \leq \theta \leq 25^\circ$;
- $\chi^2_{track}/\mathrm{NDF} \leq 10$;
- $\chi^2_{vertex} \leq 25$;
- $R_0 \leq 10\,\mathrm{cm}$;
- Number of Planar Segments (primary + secondary) ≥ 1 ;
- Number of Segments (planar + radial) ≥ 2 ;
- $\frac{\delta p}{p} \leq 1$

Forward tracks cuts make use of the $\chi^2_{\mathrm{track}}/\mathrm{NDF}$ of the track fit and the χ^2_{vertex} of the vertex fit. These variables were also used to make the Class 24 selection and have thus already been discussed in section 4.1.1. Since the momentum of a track is determined by the curvature of the track high momentum tracks will be almost 'straight', resulting in a large momentum error $\frac{\delta p}{p}$. This cut has been included to remove any tracks with badly defined momentum values.

Combined Track Cuts

- $p_T \geq 150\,\mathrm{MeV/c}$;
- $|\,\mathrm{DCA}'\,| \leq 5\,\mathrm{cm}$;

Distributions for the CTD, FTD and combined track variables are shown in figure 4.1, 4.2 and 4.3 for data and Monte Carlo. Class 24 events were chosen as an initial event selection (as is the procedure for this analysis) then further track cuts

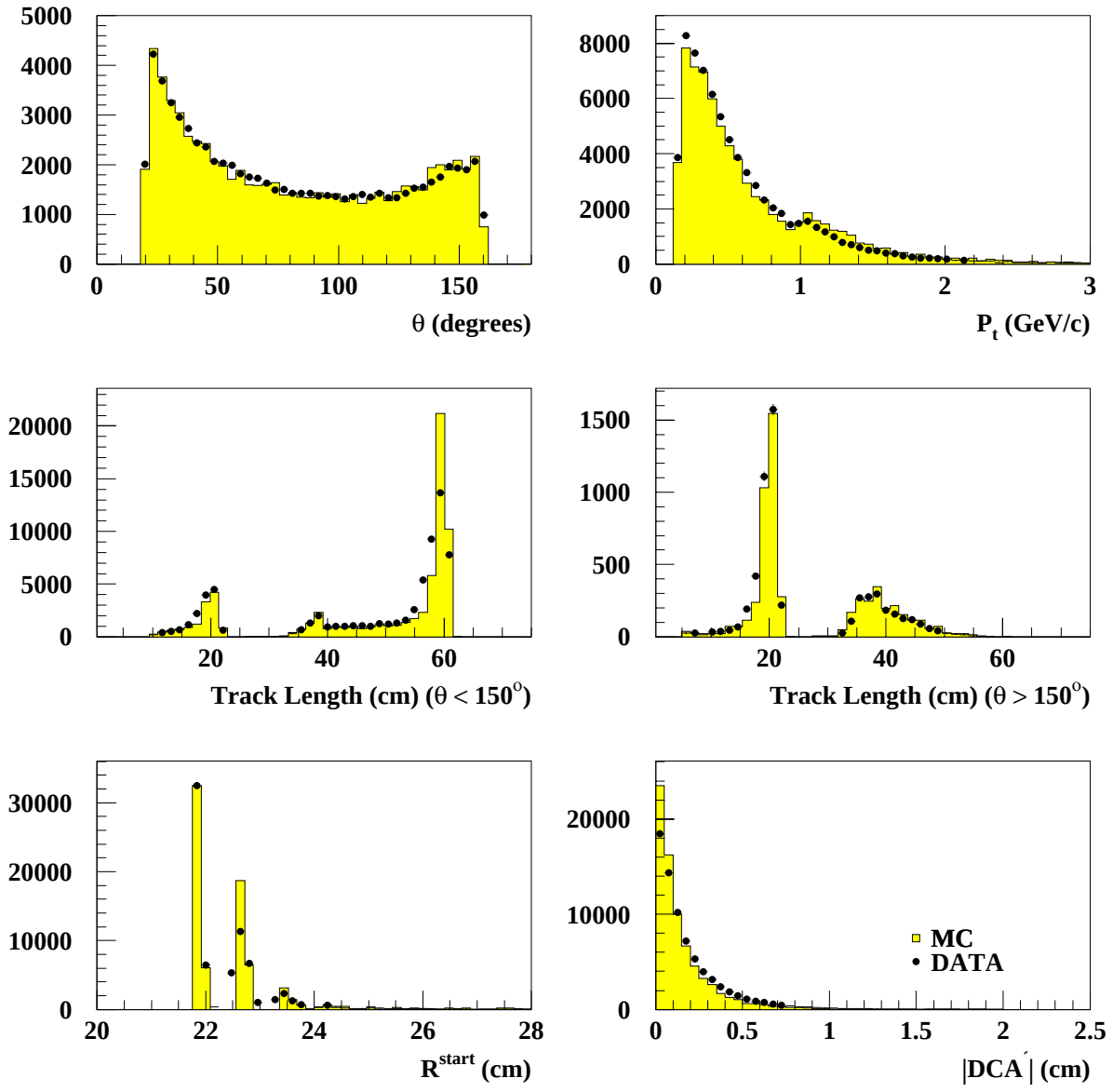

Figure 4.1: *Distributions for the CTD variables forming part of the track selection criteria as described in section 4.2. The shaded histograms are the Monte Carlo distributions and the closed point are the data distributions.*

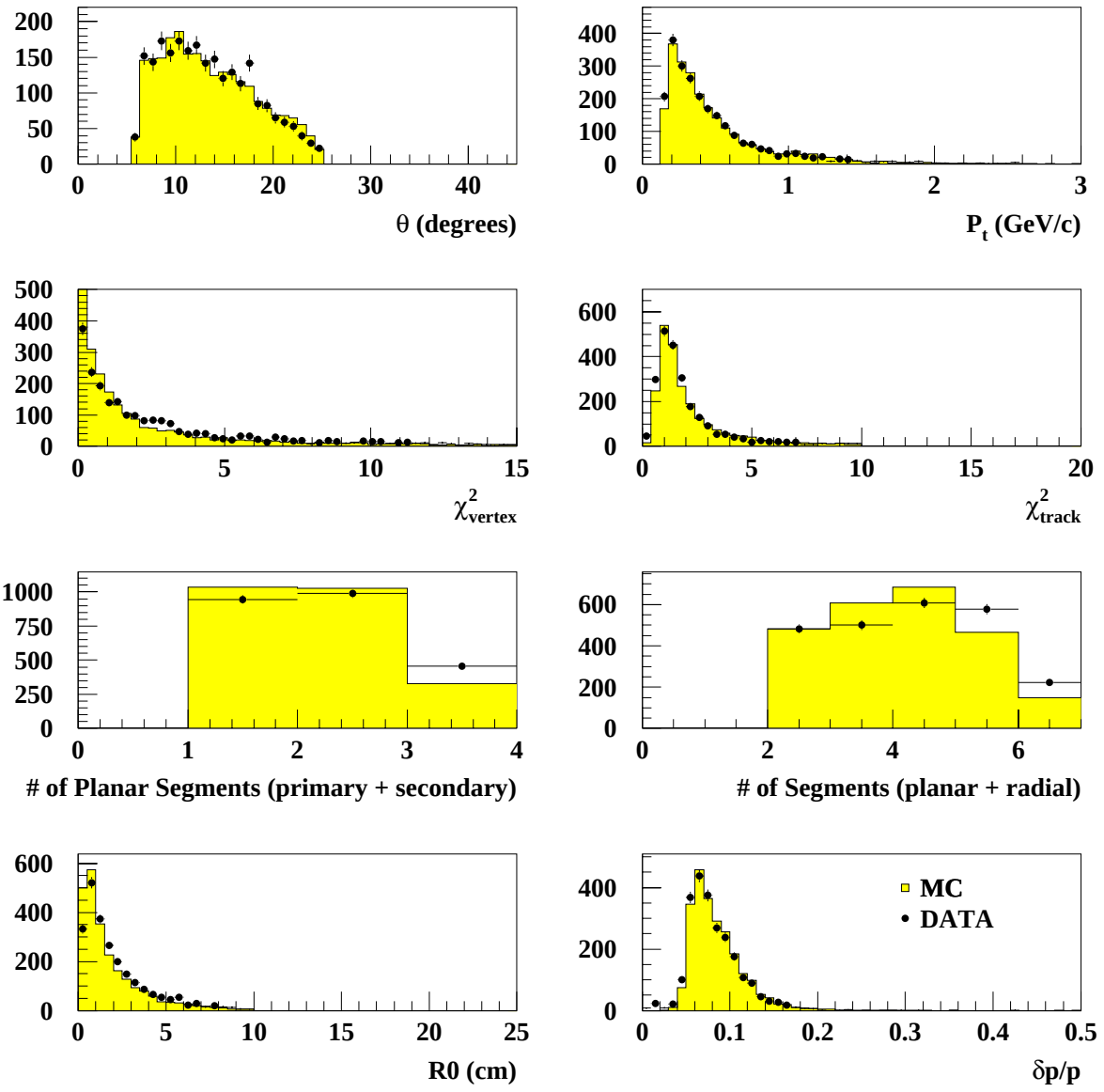

Figure 4.2: *Distributions for the FTD variables forming part of the track selection criteria as described in section 4.2. The shaded histograms are the Monte Carlo distributions and the closed point are the data distributions.*

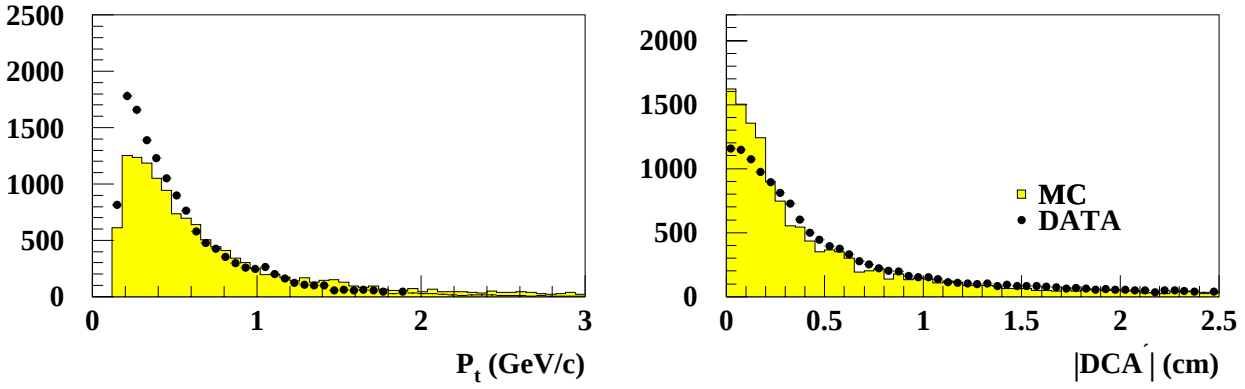

Figure 4.3: *Distributions for the combined track variables forming part of the track selection criteria as described in section 4.2. The shaded histograms are the Monte Carlo distributions and the closed point are the data distributions.*

were applied to this sample. The population of low p_T tracks is greater for data than for Monte Carlo in the case of the FTD and more especially the combined tracks. However, there is good agreement between the Monte Carlo and data for the other distributions.

4.2.2 Inner Track Hypothesis Removal

Multiple fit hypotheses arise because the same track can be linked to several vertices or a central track can exist with and without a forward track. In the case of a combined track, the tracking bank will consist of three entries corresponding to the forward, central and combined tracks which are hypotheses of the same physical track. In order to prevent double counting the best hypothesis must be chosen. Combined tracks containing information from both the forward and the central tracks are usually chosen [47] in preference to central tracks which are chosen in preference to forward tracks.

4.3 Muon Track Linking

A muon track identified by the instrumented iron, the LAr or the FMD may be linked to an inner track associating the muon track with a vertex. The instrumented iron, LAr and FMD track quality cuts made by this track selection are essentially the cuts that are defined by the Class 24 event selection described in section 4.1.

4.3.1 Muon Link Hypothesis Removal and the Selection of 'Best' Links

For high multiplicity events there are often several muon tracks detected by the outer detectors linked to several track hypotheses found in the inner dectectors. These hypotheses are stored and analysed to determine the best link. Removal of the invalid 'link' hypotheses is attempted in two ways :

1. A choice is made utilising the link probability. The link with the highest probability is chosen over all existing link hypotheses.

2. A choice is made utilising the momentum or transverse momentum (p_T) of the track. The errors associated with low momentum tracks are large as a result of Coulomb scattering [48]. The link is therefore not constrained as well as a link made using a high momentum track. For this method the events are weighted according to the types of link that are available. If a linked muon track exists which contains a link to an iron and a FMD muon then this will be taken in preference over a track linked to only one detector. However, if a group of linked muon track hypotheses exist which contain only one link a choice can be made as to which type of link will be taken in preference.

All analyses in the following chapters that have required linked muon tracks have utilised method (1). Previous studies [49] have shown that the different methods give comparable results.

Chapter 5

Momentum Correlation Studies

The following chapter presents results from studies of the correlation of the momenta of muon tracks reconstructed by the FTD and the FMD. A similar study has been made of the correlation between measurements made by the CTD and the FTD for both hadrons and muons. These correlation studies provide independent tests on the reliability of the momentum measurement made by the FTD for vertex fitted tracks , which is an essential prerequisite for the analysis discussed in chapter 6.

Muons resulting from elastic J/ψ decays offer certain clear advantages when investigating the performance of the H1 forward tracking detectors. Firstly, unlike electrons or charged hadrons, muons do not shower in the thick end-wall of the CTD or the many cell walls encountered when traversing the FTD. In addition muons resulting from the decay of J/ψ mesons have a well defined effective mass so that the position and width of the peak seen in the reconstructed di-muon effective mass spectrum provide a check on the detector performance. By contrast the pions from K^0_s decays do shower in the material mentioned previously and furthermore the separation of the pion tracks becomes less than the two track resolution of the FTD at K^0 momenta above approximately 10 GeV/c [50]. The muons resulting from J/ψ decays remain well separated to a much higher J/ψ momenta because of the bigger energy release in the J/ψ decay.

5.1 Correlation Methods.

Two correlation methods are employed which make independent comparisons between the momentum measured by the FTD for vertex fitted tracks with the momentum measured by the FMD or CTD for the same track.

Method (1)

This method uses 'combined' tracks which have been constructed from associated CTD and FTD track segments. All these tracks have passed the stringent track cuts for CTD and FTD tracks described in chapter 3 so that the combined tracks are well measured and form an possible sample for making comparisons of the momentum of the FTD track and the CTD track.

Method (2)

This method requires good FTD tracks that are linked to a FMD track (and or a forward end-cap iron track). When travelling from the FTD to the FMD a muon must pass through the LAr calorimeter and instrumented iron and on average loses 2.9 GeV [52]. In addition when passing through the toroid of the FMD the muon must have a minimum momentum of 2.25 GeV/c (see figure 5.2) if it is to be reconstructed. This means that by requiring a good FTD track linked to a FMD track the track can only have a momentum greater than 5.15 GeV/c.

5.2 Data Samples

The data samples used for this analysis are the following :

Data :

- 1995 and 1996 DST data with no class selection for combined tracks. Method (1) is applied to this data.

- 1995 and 1996 DST data in which Class 24 has been selected with the further selection that each event contains at least one muon. Method (2) is applied to this sample.

Monte Carlo :

- AROMA $c\bar{c}$ and $b\bar{b}$ events.
- LEPTO and DJANGO DIS events

The Monte Carlo files that contain events generated by LEPTO and DJANGO [53, 54] describe DIS events (the production mechanism for DIS events was described in section 1.2). The Monte Carlo file that contains events generated by AROMA [55] describe events that have been produced via boson-gluon fusion giving heavy flavour products (the decay products of which contain single muons). The correlation studies described below are not expected to show any model dependence therefore the analysis has been applied to the total Monte Carlo sample in order to improve statistics[1].

5.3 Momentum Correlations.

The correlations presented here are between the momentum measured by the FTD (p_{FTD}) and the momentum measured by either the CTD (p_{CTD}) for hadrons and muons or the FMD (p_{FMD}) for muon tracks only. The angular ranges of the CTD and the FMD ($20° < \theta < 155°$ and $3° < \theta < 18°$ respectively) together cover the angular range of the FTD ($7° < \theta < 25°$). However, there is little overlap between them, thus offering independent studies about the momentum measurement made by the FTD.

Figure 5.1 shows correlation plots for data ((a) and (b)) and Monte Carlo ((c) and (d)) which correspond to the two correlation methods. Plots (a) and (c) were

[1]Recent studies have shown that there is an inefficiency when linking CTD and FTD track segments to form combined tracks at low momentum [51]. This may also be present for high momentum tracks and may offer some explanation for some of the effects seen in section 5.6.1.

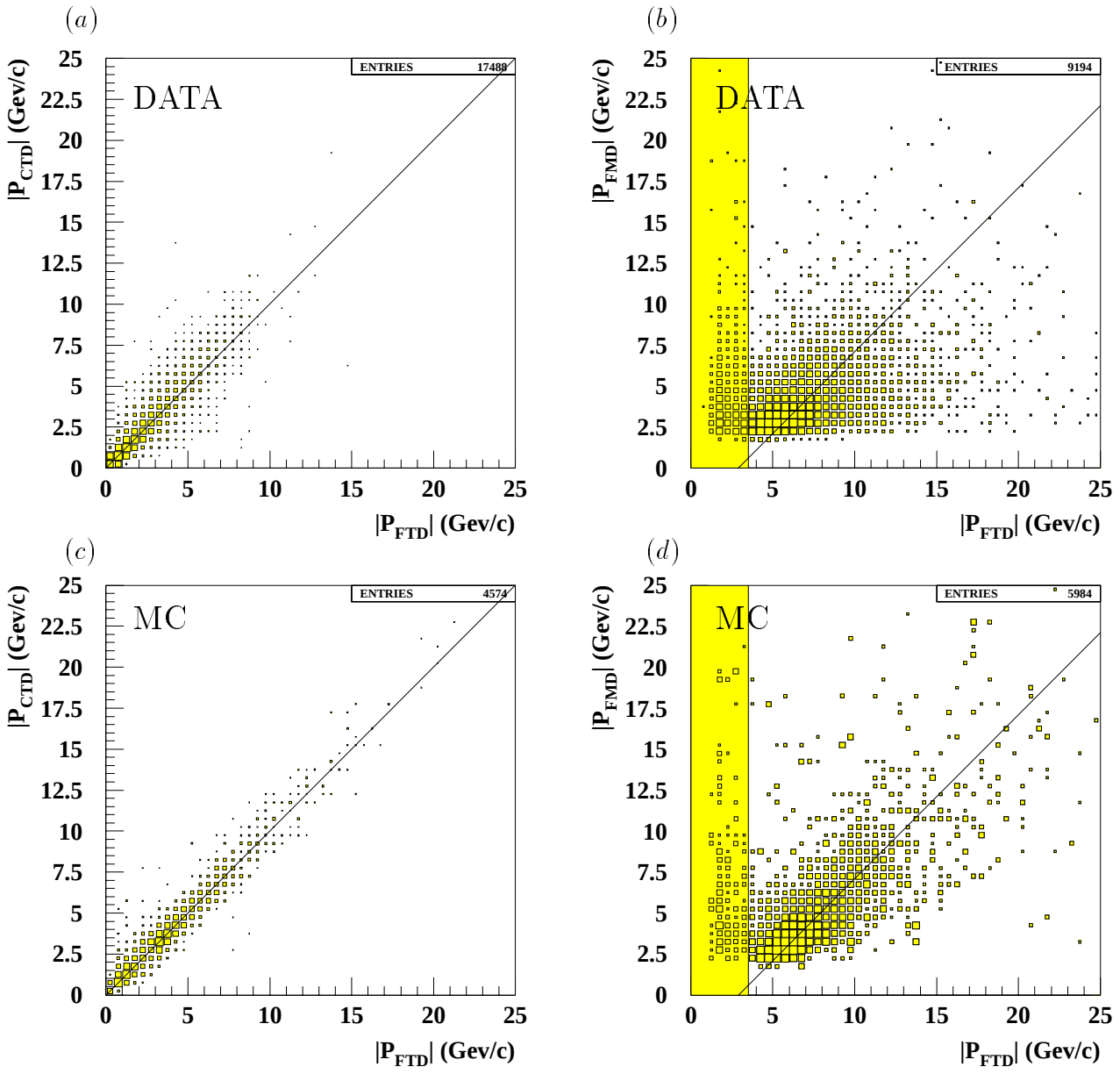

Figure 5.1: *The momentum measured by the FTD* ($|p_{FTD}|$) *plotted against : (a) the momentum measured by the CTD* ($|p_{CTD}|$) *and (b) the momentum measured by the FMD* ($|p_{FMD}|$) *for 1995 data. Plots (c) and (d) are equivalent to (a) and (b) but show the distributions for Monte Carlo. The shaded regions that have been indicated on plots (b) and (d) are where FTD tracks have been falsely linked to FMD tracks.*

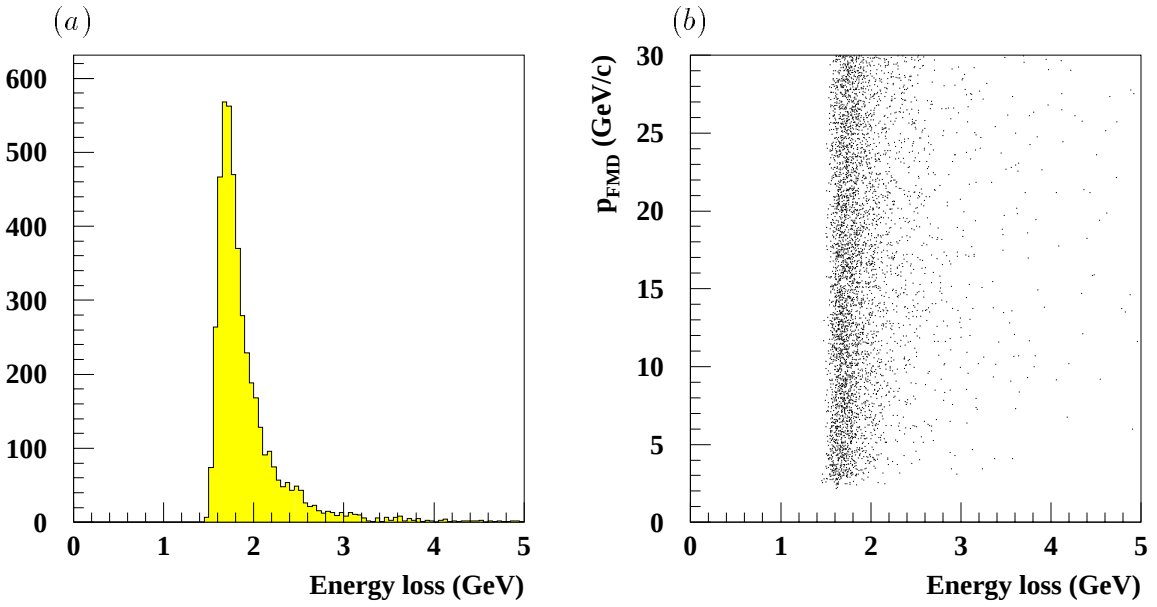

Figure 5.2: *(a) The energy loss of a muon passing through the FMD toroid and (b) the energy loss versus the muon momentum observed in the FMD.*

obtained with method (1) and plots (*b*) and (*d*) were obtained with method (2). If correlated the track momenta should fall along the solid line drawn on each plot; where an offset of 2.9 GeV (plots (*b*) and (*d*)) takes into account the mean energy loss experienced by a muon travelling through the LAr calorimeter and instrumented iron. In both cases the expected correlation can be seen, however, there is more agreement for method (1). The obvious departures from correlation for method (2) are discussed in the following sections.

5.4 False Links

It is observed that for method (2) there is a population of FTD tracks linked to a FMD tracks in the shaded regions of plots (*b*) and (*d*) of figure 5.1 with $|p_{FTD}| < 4\,\mathrm{GeV/c}$. This is physically impossible because of the expected energy loss sustained by a particle travelling from the FTD and reconstructed by the FMD.

Figure 5.2, plot (*a*) shows the energy loss in the toroid and plot (*b*) shows the energy loss in the toroid as a function of muon momentum for Monte Carlo events.

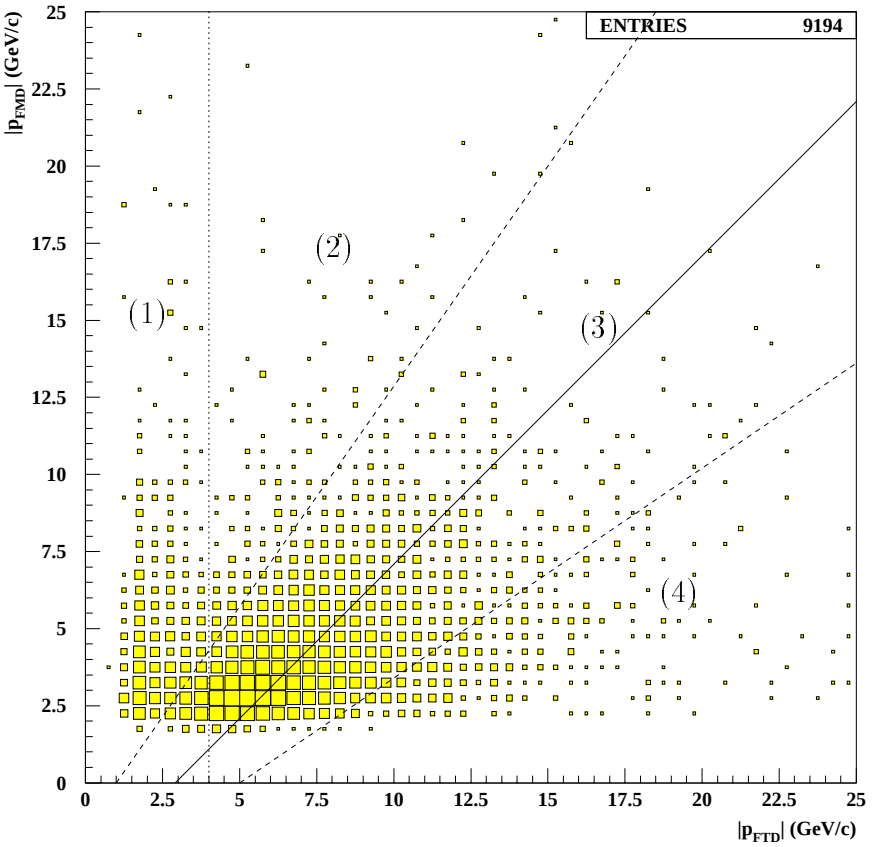

Figure 5.3: *Correlation plot showing the momentum measurement made by the FMD* ($|p_{FMD}|$) *against the momentum measurement made by the FTD* ($|p_{FTD}|$) *for 1995 data. The plot has been separated into four regions which are discussed in section 5.4.*

The only selection that has been made is that there must be FMD tracks present in the event. It is seen from plot (*b*) that muons entering the FMD with a momentum less than approximately 2.25 GeV/c cannot be reconstructed. Hence a muon track can only be detected in the FMD if it has an initial track momentum at the vertex of greater than approximately $(2.9 + 2.25 = 5.15)$ GeV/c.

Figure 5.3 is a repeat of figure 5.1 (*b*) for the correlation between the FMD momentum and the FTD momentum for data. The plot has been divided into four regions which have been studied in turn to examine separately the potential problems that are associated with the linking between the FTD, the iron and the FMD. The event display pictures, figures 5.4, 5.5, 5.6 (5.7) and 5.8 show event examples from

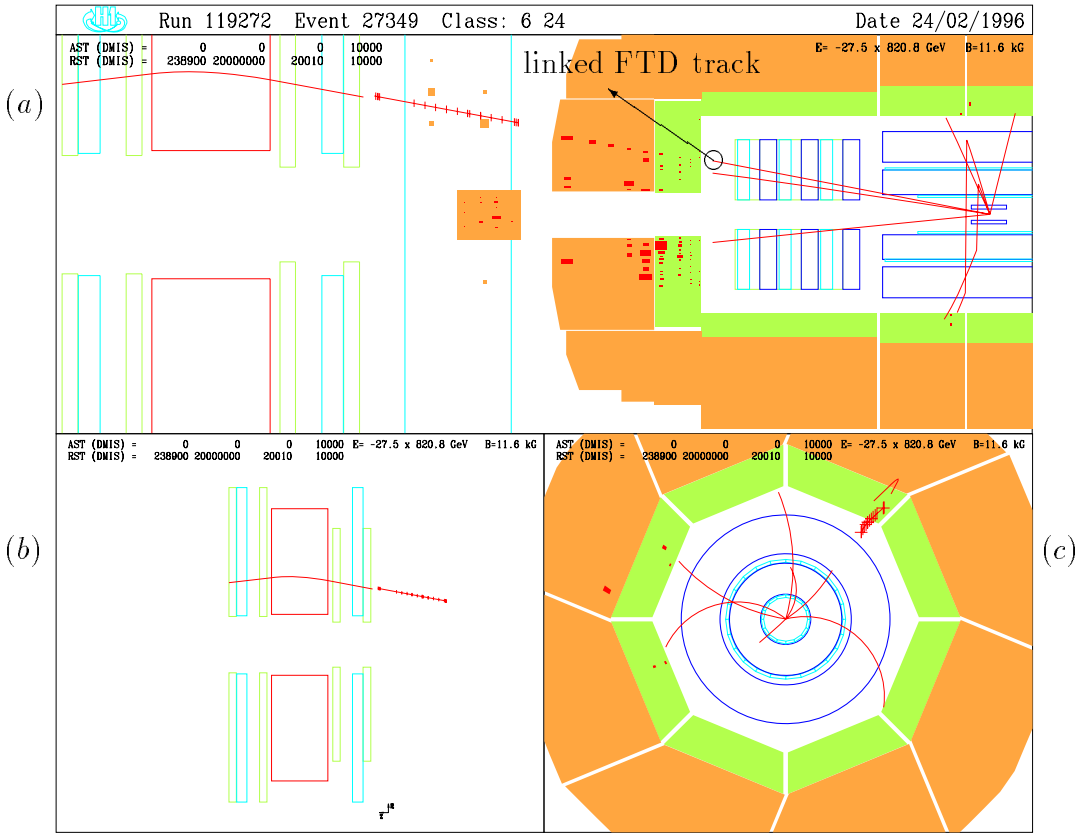

Figure 5.4: *An example event that can be found in region (1). The example illustrates how a track with low momentum measured by the FTD* (p_{FTD}) *has been linked incorrectly to a muon track reconstructed by the iron and FMD.*

the regions 1, 2, 3 and 4 respectively. In each case (*a*) shows a side view of the H1 detector, (*b*) is the side view limited to the FMD and showing again the muon track which has been reconstructed and (*c*) is a radial view of the H1 detector. The views (*a*) and (*c*) have been magnified so as to enhance the view of the forward detectors: the FTD, the instrumented iron, and the FMD.

Region (1)

In this region FMD tracks have been linked to lower momentum FTD tracks. The reconstructed momentum value measured by the FTD should exceed 5.15 GeV/c^2 if

[2]The plot displays a cut at 4GeV/c which is given as the minimum value of the momentum of the FTD track when taking into account the momentum resolutions of the FTD and FMD.

it is to be detected by the FMD.

These links are therefore incorrect and could be attributed to the FTD track having a badly measured momentum or that the wrong choice of FTD track has been made. In the latter case it is possible that the actual FTD track which should have been linked may not have been reconstructed due to a lack of hits. A reasonable hypothesis is that a low momentum track reconstructed by the FTD has been able to be linked to a FMD track because the linking errors are larger for low momentum tracks because they take into account the increased multiple scattering. Alternatively the FTD momentum measurement may be badly underestimated or the FMD measurement has been overestimated.

It is unlikely that the momentum of the muon track measured in the FMD is overestimated. This is because a FTD track with a minimum momentum of 4 GeV/c which has traversed the iron and LAr would not have enough energy to penetrate the toroid and leave any hits in the post-toroid layers of the FMD. To reconstruct a full FMD track the pre-toroid track segment would have to be linked to a post-toroid track segment. It is unlikely that the post-toroid segment is constructed from hits due to noise because the post-toroid chambers are shielded by the toroid, thus reducing the amount of hits due to noise.

Figure 5.4 shows an example of a bad link. The linked FTD track is labelled with a circle. The FTD track of 2.14 ± 0.02 GeV/c has been linked to an iron track and this in turn has been linked to a FMD track of 2.76 ± 0.39 GeV/c. The FTD track would not be able to reach the FMD as it does not have sufficient momentum so this track must be incorrectly linked.

Region (2)

The tracks in the FTD in this region are linked to higher momentum tracks in the FMD. These cases could be examples of incorrect linking or they may be due to the forward tracker underestimating the track momentum of the muon (as was the possible case in region (1)). Alternatively, the FMD may be overestimating the muon momentum.

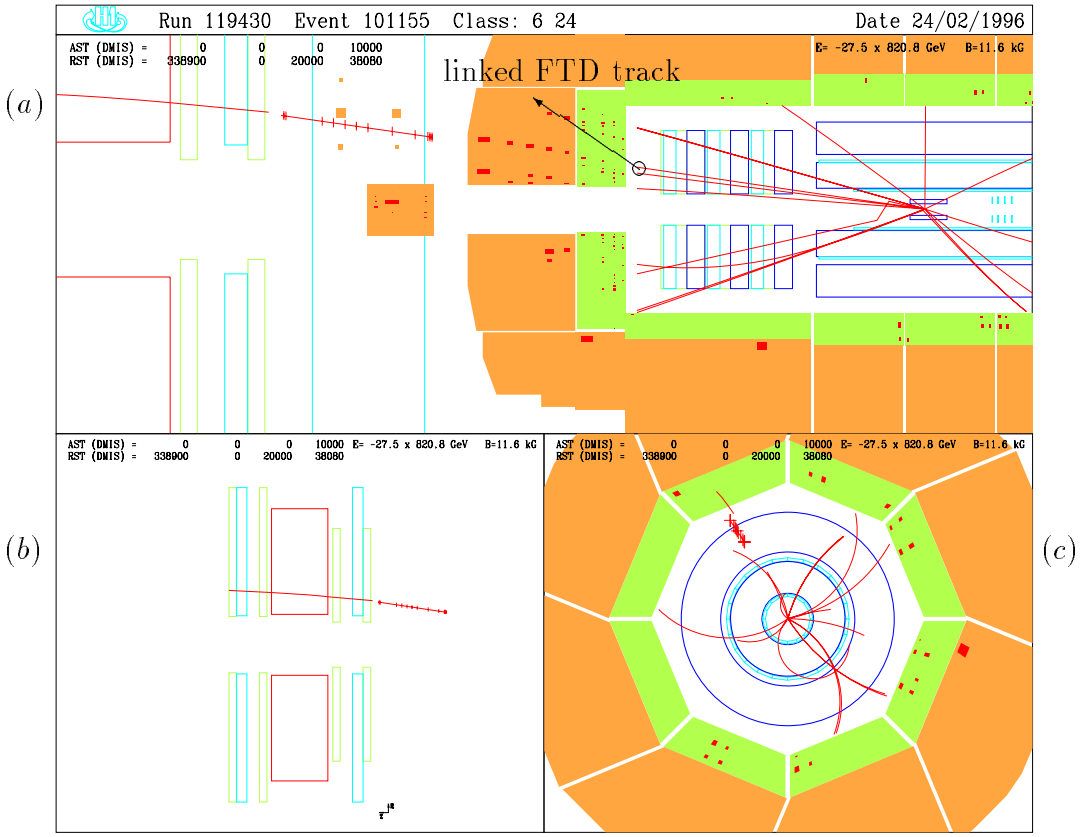

Figure 5.5: *An example event that can be found in region (2). The example illustrates an incorrectly linked muon track. This link has resulted from either the momentum measured by the FTD* (p_{FTD}) *being overestimated or the momentum measured by the FMD* (p_{FMD}) *being underestimated.*

Figure 5.5 shows an event from this region. The FTD track that has been linked to an iron track has been marked by a circle. In this example the track momentum measured in the FMD is $13.70 \pm 2.44\,\mathrm{GeV/c}$ and this is higher than the momentum measured in the FTD, namely $4.89 \pm 0.69\,\mathrm{GeV/c}$.

The FTD track has enough energy to penetrate the FMD system, however there is a considerable difference between the momentum measured by the FMD and the momentum measured by the FTD. The same conclusions that were formed for region (1) are applicable here. The FTD momentum measurement has been badly underestimated or the wrong FTD track has been linked.

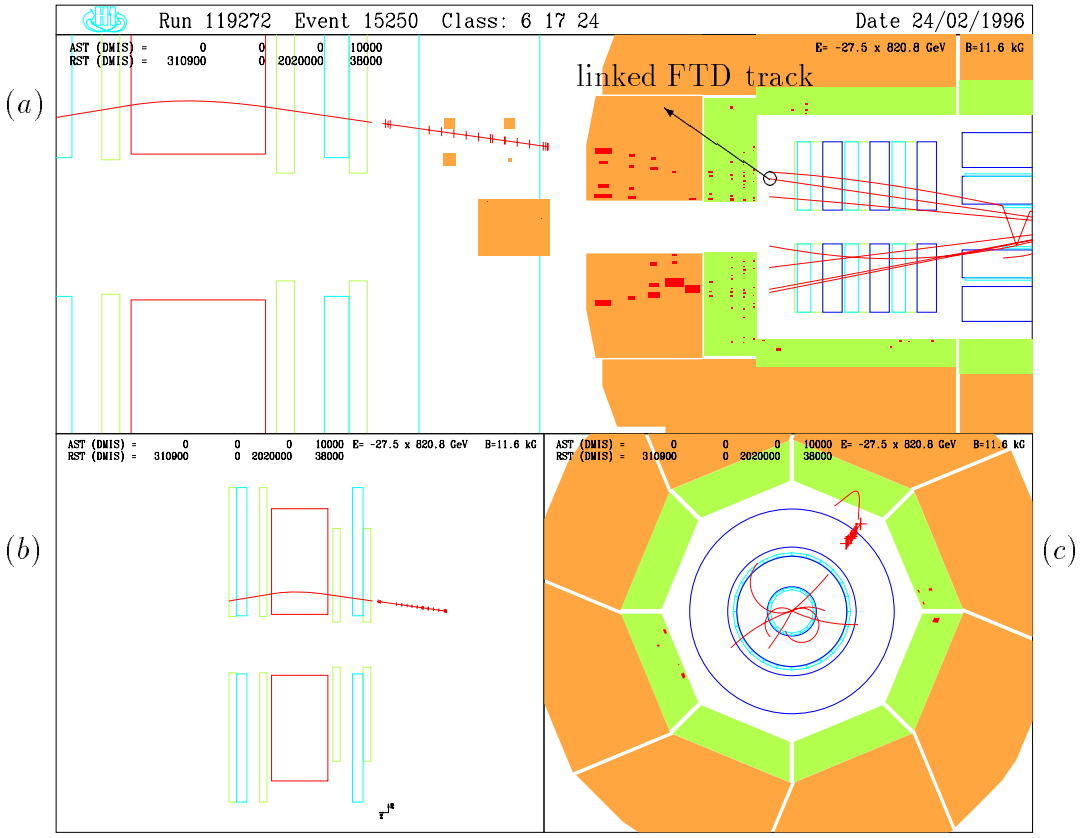

Figure 5.6: *An example event that can be found region (3). The example illustrates a muon track which has been correctly linked. The measured momentum values* p_{FTD} *and* p_{FMD} *correlate when energy losses are taken into account.*

Region (3)

This region was defined to cover the major part of the distribution of Monte Carlo events shown in figure 5.1, plot (*d*). Events in this region show that p_{FTD} and p_{FMD} are well correlated when taking into account the energy losses due to the intervening material. Two typical examples of the events found in this region are shown in figure 5.6 and figure 5.7. The event shown in figure 5.6 contains a track with a momentum measured in the FTD of $5.47 \pm 0.54\,\mathrm{GeV/c}$ linked to an iron track with an undefined momentum value which in is turn linked to a track in the FMD with a momentum of $2.69 \pm 0.43\,\mathrm{GeV/c}$. These momentum values differ by $2.78 \pm 0.69\,\mathrm{GeV/c}$ which is consistent with the expected energy loss when travelling

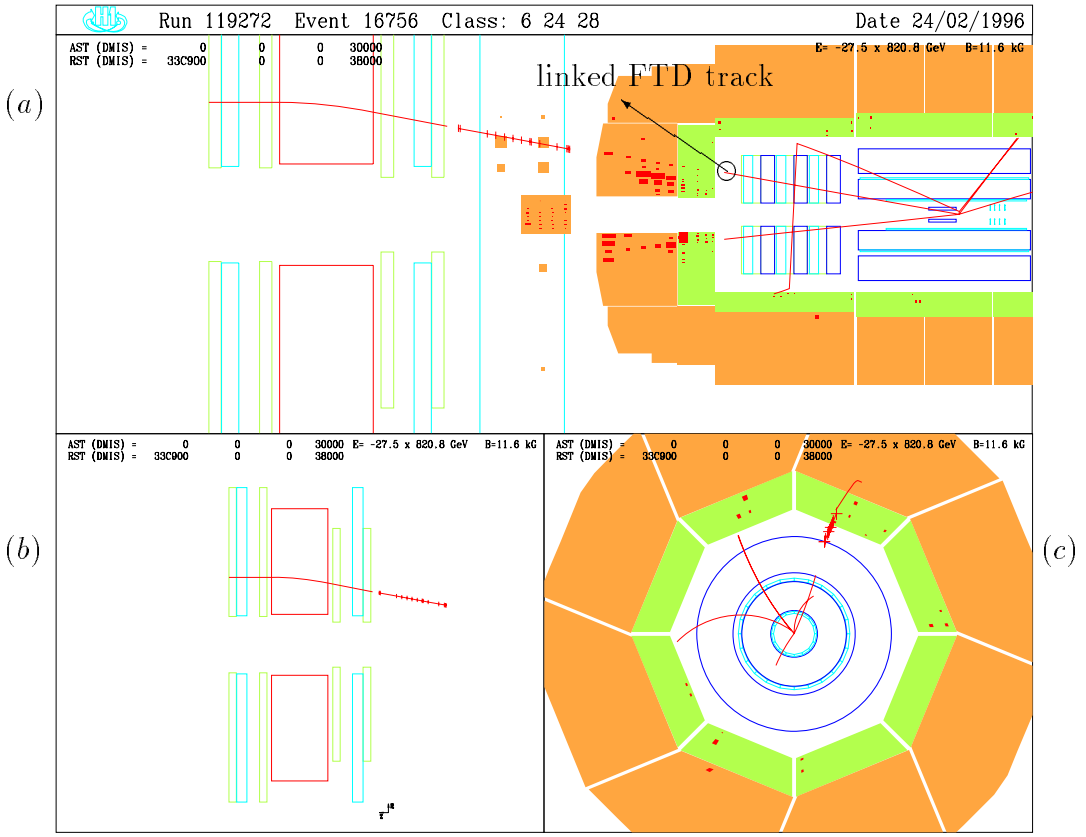

Figure 5.7: *An example event that can be found region (3). The example illustrates a muon track which has been correctly linked. The measured momentum values* p_{FTD} *and* p_{FMD} *correlate when energy losses are taken into account.*

from the FTD to the FMD.

Figure 5.7 shows an event with a FTD track of 7.40 ± 0.84 GeV/c linked to an iron track which is linked to a FMD track of 3.81 ± 0.67 GeV/c. The momentum difference of 3.59 ±1.07 GeV/c is consistent with expectation and this supports the conclusion that the tracks falling in this region have been correctly linked.

Region (4)

The FTD tracks in this region have momentum values of $|p_{FTD}| > 5$ GeV/c and are linked to FMD tracks where the momentum measured in the FTD is significantly higher than that measured in the FMD. This may be attributable to incorrect linking or it may be due to the track momentum being overestimated in the FTD or being

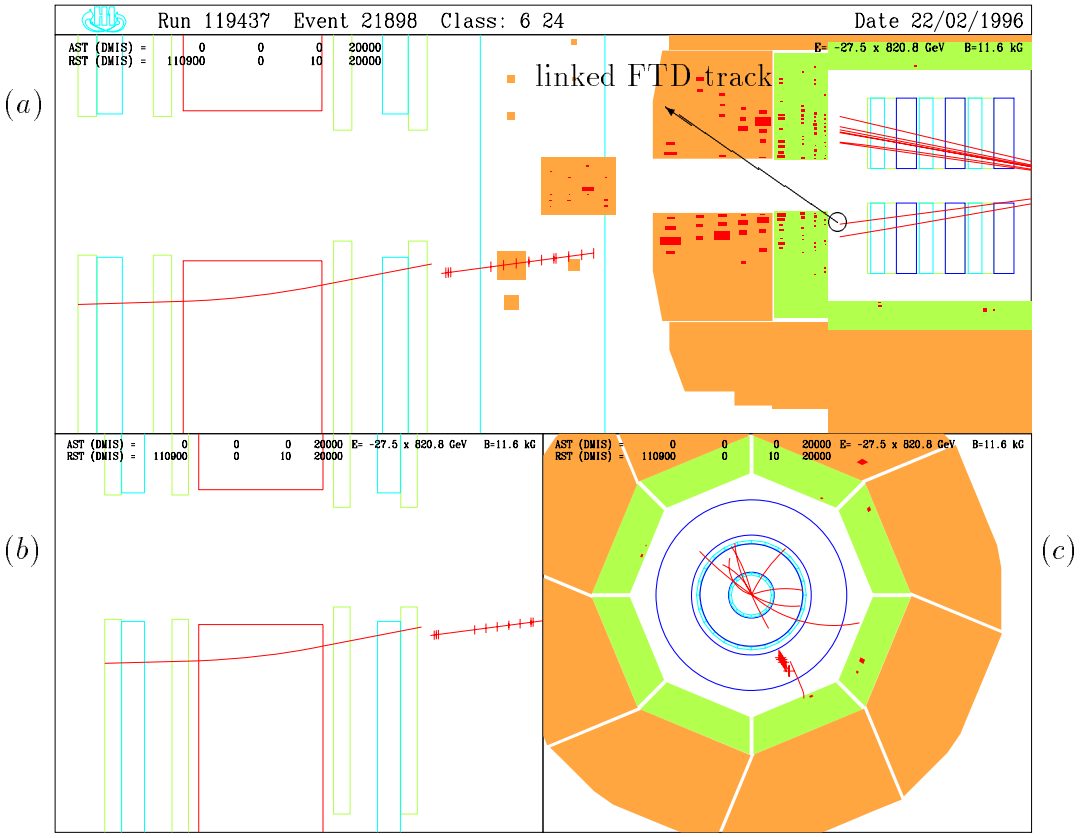

Figure 5.8: *An example event that can be found in region (4). The example illustrates how a muon track with low momentum as measured by the FMD* (p_{FMD}) *has been linked incorrectly to an inner track reconstructed by the FTD.*

underestimated in the FMD.

An event where the FMD measurement seems to have underestimated the muon momentum is shown in figure 5.8. The FTD track has a momentum of 13.5 GeV/c which is considerably higher than the FMD track which has a momentum value of 4.6 GeV/c. It is likely that the FMD pre-toroid track segment is incorrectly reconstructed as its extrapolation appears to be in bad agreement with the iron track. To gain further information about the FMD track the event could be studied before it reached DST (POT data) as the hit information would still be available.

5.5 The Dependence of False Links on the Number of FTD and FMD Hits

The extrapolation of lower momentum FTD tracks gives rise to larger uncertainties due to large multiple scattering effects within the LAr calorimeter thus making it more likely for a false link to occur. If this is indeed the dominant reason for false links then it could be expected that incorrect links would occur most often when the number of low momentum tracks reconstructed by the FTD was large. In order to investigate this point, correlation plots of $|p_{FMD}|$ versus $|p_{FTD}|$ for data are shown in figure 5.9 as a function of the total number of forward tracker planar drift chamber hits detected for the event.

Figure 5.9 (a) shows that low multiplicity events containing a maximum of 300 planar hits have a lower proportion of events in region (1) than for figures 5.9 (b), (c) and (d) where the number of planar hits is larger than 300. This shows that the number of false links in this region is correlated with the FTD hit multiplicity. An alternative way to illustrate this feature is given in figure 5.10 (a) which shows the ratio of the number of links with a FTD momentum value of less than 4 GeV/c divided by the total number of links in the sample plotted as a function of the number of FTD planar hits. Figure 5.10 (b) shows the same ratio but as a function of the sum of the number of pre-toroid hits in the FMD. The solid points are data and the open points are Monte Carlo predictions.

The false link ratio in the data increases by approximately a factor of four when the number of hits detected by the FTD planar chambers increases from 0 to 2000. There are no Monte Carlo points in figure 5.10 (a) for a high multiplicity of planar hits (1500-2000) because the number of high multiplicity events in Monte Carlo is smaller than for the data. Evidently, the more low momentum tracks that are reconstructed in the FTD increases the chance of an incorrect link. This can be expected because low momentum tracks undergo larger deviations due to multiple Coulomb scattering.

The false link ratio as a function of FMD hits, shown in figure 5.10, is approxi-

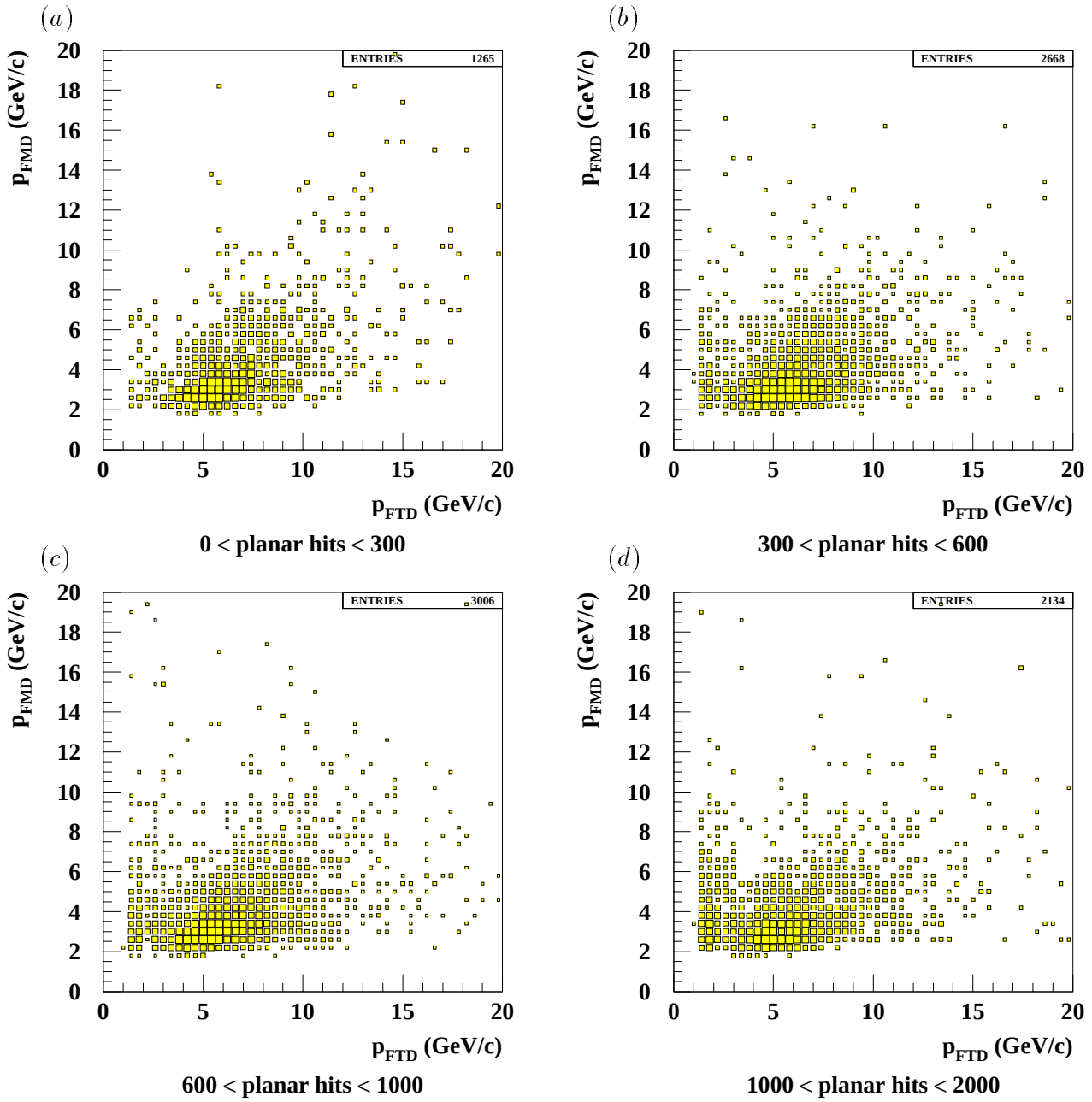

Figure 5.9: *The momentum measured by the FMD* (p_{FMD}) *plotted against the momentum measured by the FTD* (p_{FTD}) *as a function of the total number of FTD planar drift chamber hits detected for the event.*

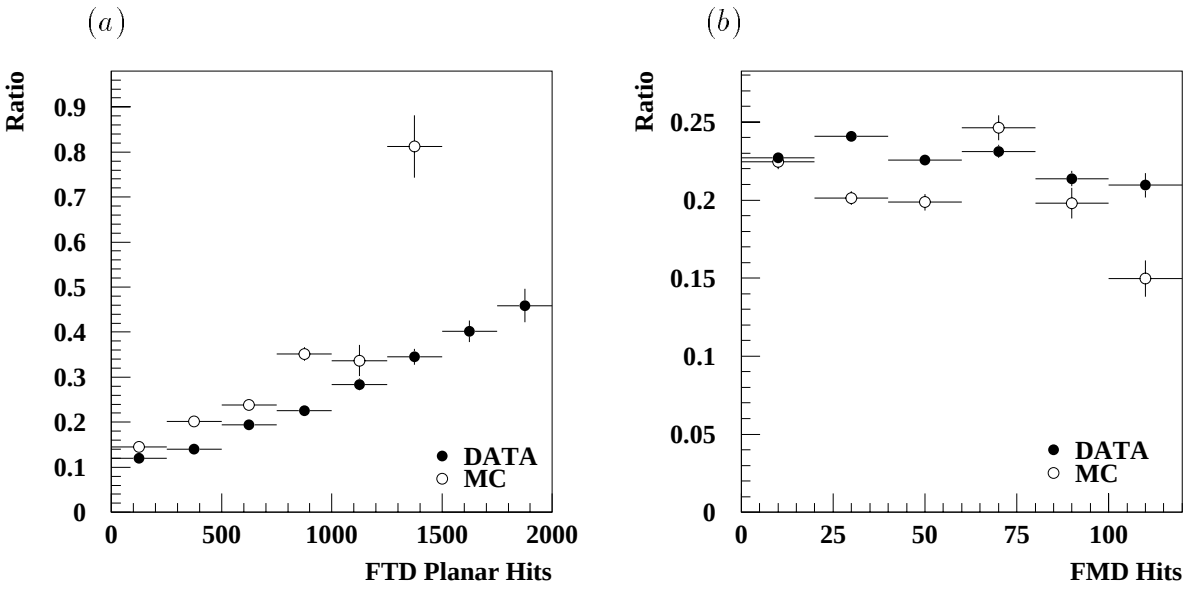

Figure 5.10: *The ratio of the number of links with* $|p_{FTD}| < 4$ *GeV/c (false links) divided by the total number of links in the data sample has been plotted against (a) the total number of FTD planar drift chamber hits and (b) the total number of hits detected by the pre-toroid layers of the FMD. The data points are the closed circles and the Monte Carlo points are the open circles.*

mately constant over the range of 0 to 100 hits detected in the first three pre-toroid layers. The chance of reconstructing a false FMD track is therefore not dependent on the multiplicity of the event and it is likely that the tracks that are detected are valid tracks.

The false link ratio was seen to fall for 1995 reconstructed data after reprocessing with improved FTD reconstruction. This is illustrated in figure 5.11 where the false link ratio is displayed as a function of FTD planar hits and FMD hits at these two stages of the reprocessing.

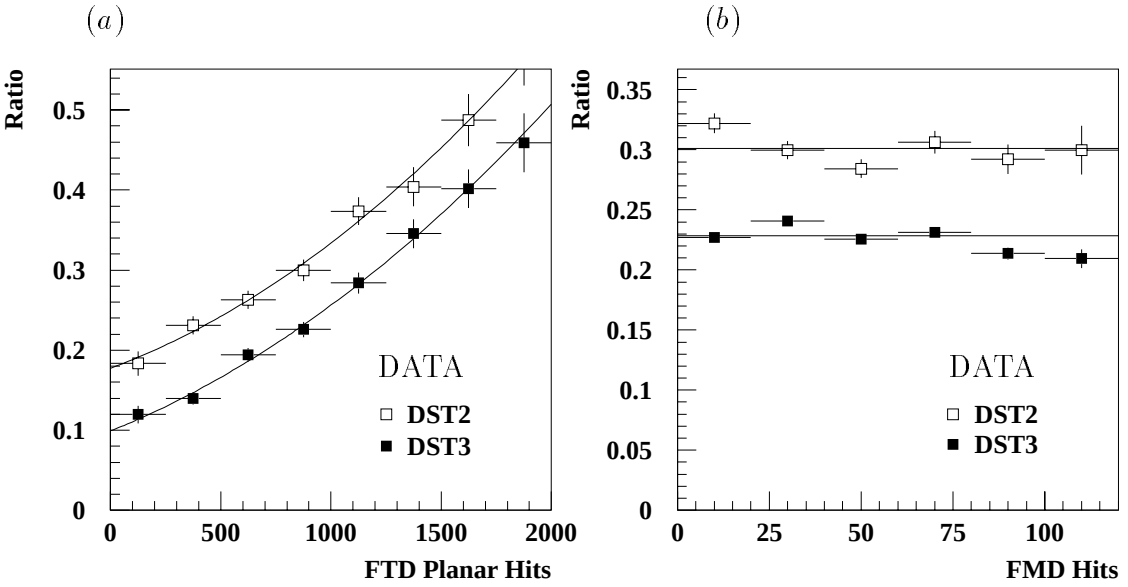

Figure 5.11: *The ratio of the number of links with* $|p_{FTD}| < 4$ *GeV/c (false links) divided by the total number of links in the data sample has been plotted against (a) the total number of FTD planar drift chamber hits and (b) the total number of hits detected by the pre-toroid layers of the FMD. For each plot the data has been displayed for different time intervals during the reprocessing. The open squares are DST2 reprocessed data points which represent data that was reprocessed before the DST3 data (closed square points).*

5.6 The Momentum Residual (Δp) between the FTD and the FMD measurements.

A momentum residual is defined by the expression :

$$\Delta p = \frac{p_1 - p_2}{\sqrt{\sigma_1^2 + \sigma_2^2}} \tag{5.1}$$

where p_1 and p_2 are the momentum measurements from two different detectors and σ_1 and σ_2 the errors on p_1 and p_2 respectively. If the momentum measurements are not offset by any systematic effect and the measured errors are correctly estimated then the plot of Δp takes the form of a Gaussian of width unity, centered at zero for a statistically meaningful event sample.

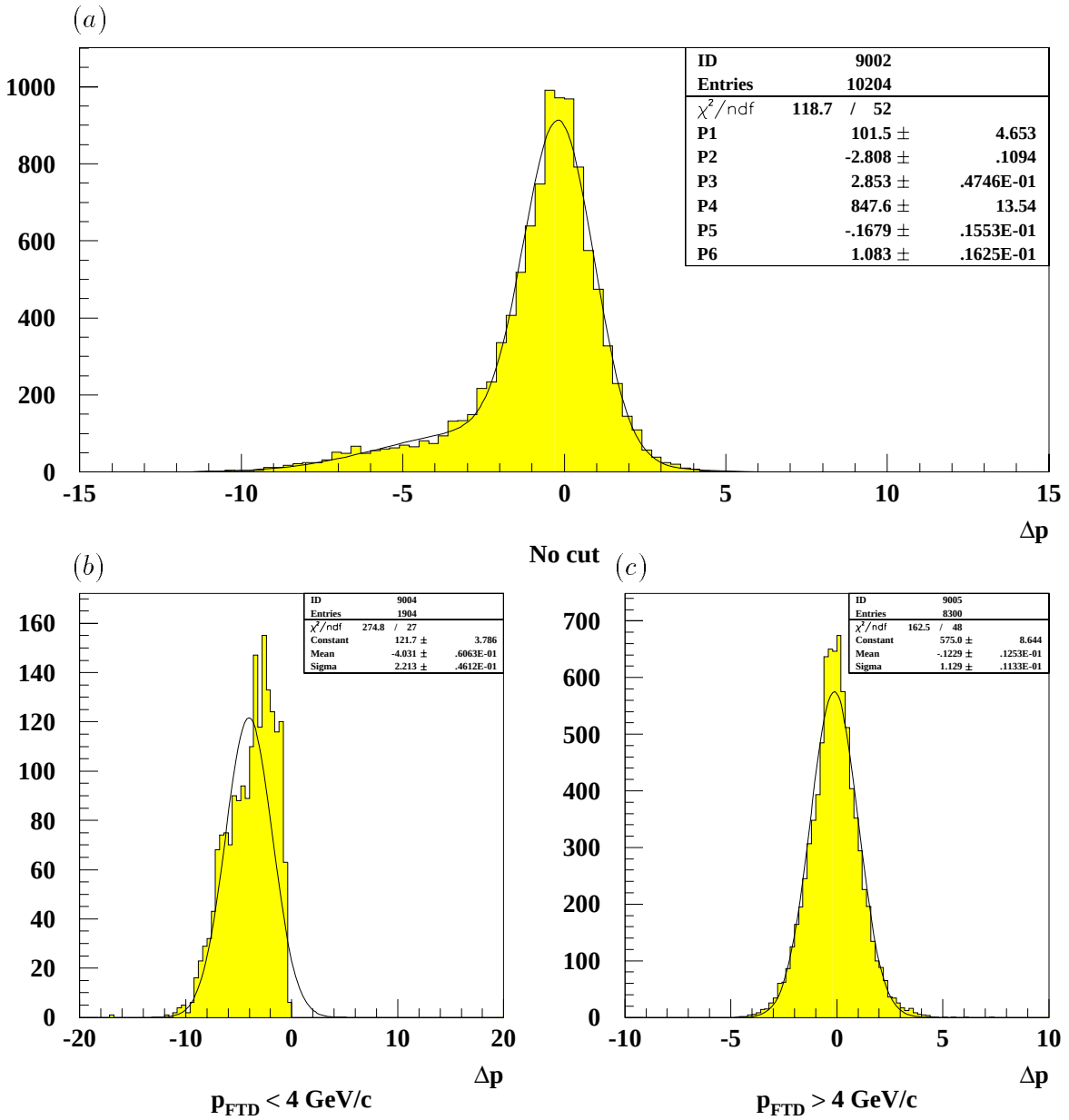

Figure 5.12: *The momentum residual (Δp) for data calculated using the momentum measured by the FTD and momentum measured by the FMD. Plot (a) is the full data sample, plot (b) shows events passing the momentum cut* $\mathrm{p_{FTD}} < 4\,GeV/c$ *and plot (c) shows events passing the momentum cut* $\mathrm{p_{FTD}} > 4\,GeV/c$.

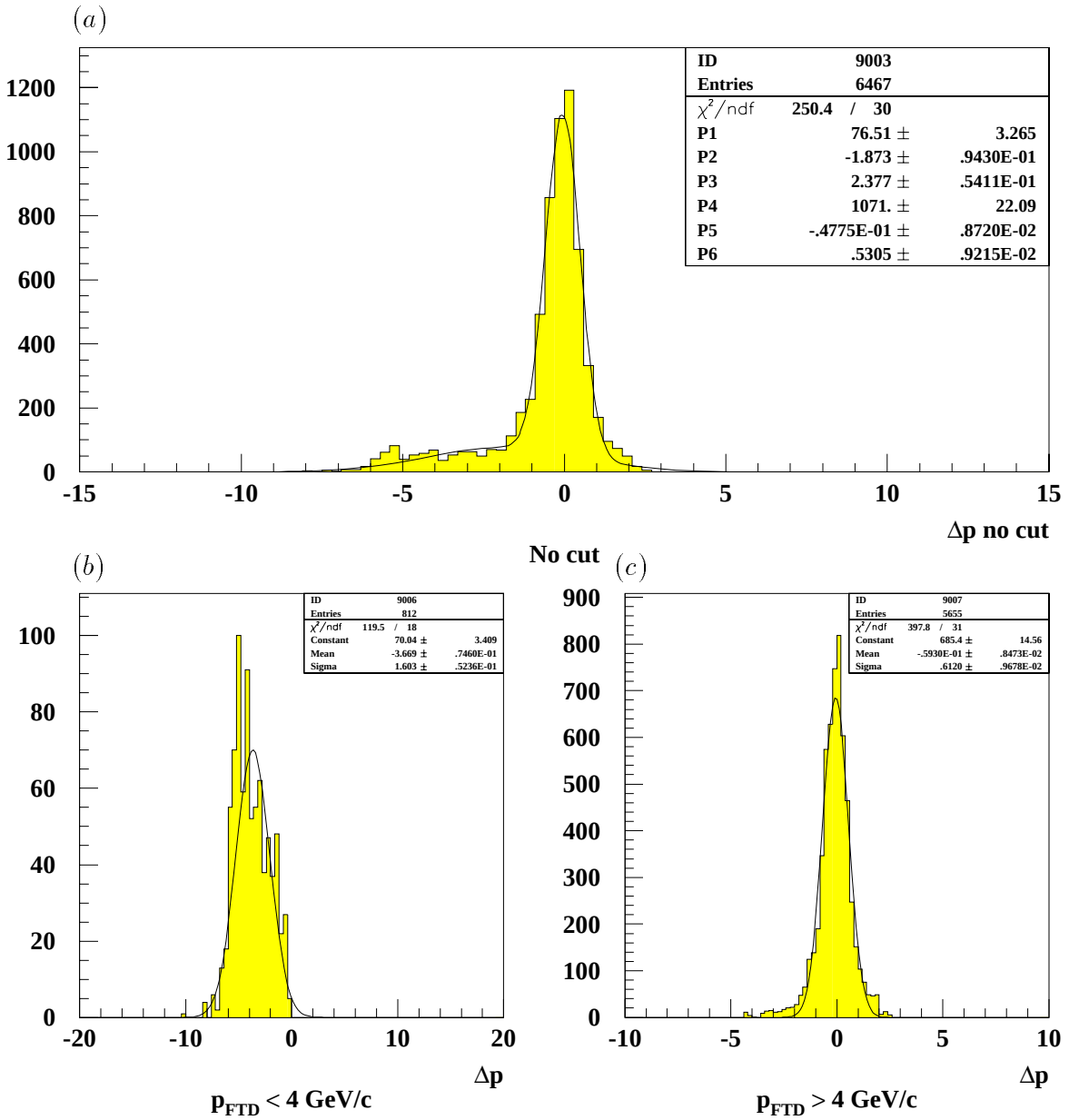

Figure 5.13: *The momentum residual (Δp) for Monte Carlo calculated using the momentum measured by the FTD and momentum measured by the FMD. Plot (a) is the full data sample, plot (b) shows events passing the momentum cut* $\mathrm{p_{FTD}} < 4\,GeV/c$ *and plot (c) shows events passing the momentum cut* $\mathrm{p_{FTD}} > 4\,GeV/c$.

The residuals between measurements in the FMD (p_1) and the FTD (p_2) are plotted in figures 5.12 and 5.13 for data and Monte Carlo respectively. The plots show (a) Δp before cuts, (b) Δp for $\mathrm{p_{FTD}} < 4\,\mathrm{GeV/c}$ and (c) Δp for $\mathrm{p_{FTD}} > 4\,\mathrm{GeV/c}$. Separating the tracks according to whether the FTD momentum is less than or greater than 4 GeV/c is effectively separating the tracks with false links from those with correct links. The plots are fitted with Gaussian functions. Plots (a) for both Monte Carlo and data show a characteristic 'shoulder' which requires a fit using the sum of two Gaussian functions. The parameters determined from the double Gaussian fit can be compared to the parameters obtained from the Gaussian fits to the distributions shown in plots (b) and (c). The values of the number of events, the mean and the sigma are given in tables 5.1 and 5.2.

The parameters determined from the double Gaussian fit to the distributions shown in plot (a) are reasonably compatible with those determined independently by the Gaussian fits to (b) and (c). Hence, the 'shoulder' of plot (a) for both data and Monte Carlo can be explained by the population of falsely linked tracks which are in region (1).

If the tracks populating region (1) in figure 5.3 are ignored, the Δp distributions for data and Monte Carlo are given by plot (c) in figures 5.12 and 5.13 respectively. For both data and Monte Carlo it can be seen that the mean is centered approximately on zero, however, $\sigma_{MC} \approx \frac{1}{2}\sigma_{data}$ which means that the resolution observed in the data is not well described by the Monte Carlo simulation and reconstruction. However, the width of the data is closer to unity (1.129) than the Monte Carlo (0.612).

5.6.1 Momentum Correlations between the FTD and the CTD and the FTD and the FMD.

By taking 'slices' of the momentum correlation plots displayed in figure 5.1 (a) and (b), the difference between the momentum determined by the FTD and that determined by the CTD or FMD can be expressed as a function of the momen-

	Data		Monte Carlo	
	No cut	$p_{FTD} < 4\,GeV/c$	No cut	$p_{FTD} < 4\,GeV/c$
Constant	101.5	121.7	76.51	70.04
Mean	-2.808	-4.031	-1.873	-3.669
Sigma	2.853	2.213	2.377	1.603

Table 5.1: *The fit parameters from the double Gaussian fit made to the distributions shown in plots (a). Figures 5.12 and 5.13 have been compared to the single Gaussian fit made to the distributions shown in plot (b) for the same figures. The parameters that correspond to the 'shoulder' of the uncut distribution have been compared to those which pass the momentum cut,* $p_{FTD} < 4\,GeV/c$.

	Data		Monte Carlo	
	No cut	$p_{FTD} > 4\,GeV/c$	No cut	$p_{FTD} > 4\,GeV/c$
Constant	847.6	575.7	1071.51	685.4
Mean	-0.1679	-0.1229	-0.04775	-0.0593
Sigma	1.083	1.129	0.5305	0.6120

Table 5.2: *The fit parameters from the double Gaussian fit made to the distributions shown in plots (a). Figures 5.12 and 5.13 have been compared to the single Gaussian fit made to the distributions shown in plot (c) for the same figures. The parameters that correspond to the main peak of the uncut distribution have been compared to those which pass the momentum cut,* $p_{FTD} > 4\,GeV/c$.

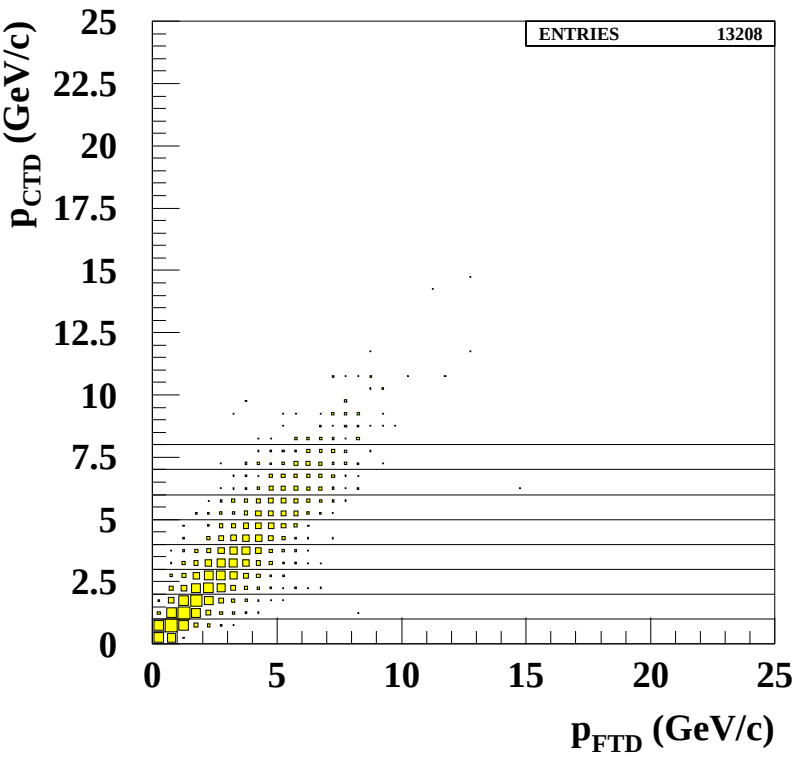

Figure 5.14: *Correlation plot showing the momentum measurement made by the CTD* ($|p_{CTD}|$) *against the momentum measurement made by the FTD* ($|p_{FTD}|$). *Slices in* $|p_{CTD}|$ *have been indicated which in section 5.6.1 are analysed to determine the difference in the momentum measured in the FTD and CTD.*

tum measured in the CTD or FMD. An illustration of the 'slicing' can be seen in figure 5.14.

For each slice, which represents a 1 GeV bin in $|p_{CTD}|$ or $|p_{FMD}|$, the difference between the the FTD momenta and the CTD or FMD momenta was calculated and a Breit-Wigner function was found to provided the best description of the distributions. These fits are shown for bins of the CTD and the FMD momentum in the figures 5.16 and 5.17 respectively. When comparing the FTD and the FMD momentum the region where $|p_{FTD}| < 4$ GeV has been excluded because these tracks, as discussed in the previous section, are seen to be the result of false links. The FMD momenta must also be incremented by 2.9 GeV/c to allow for energy loss. Each plot shows a distribution for data (points) and Monte Carlo (shaded histogram) for 1995

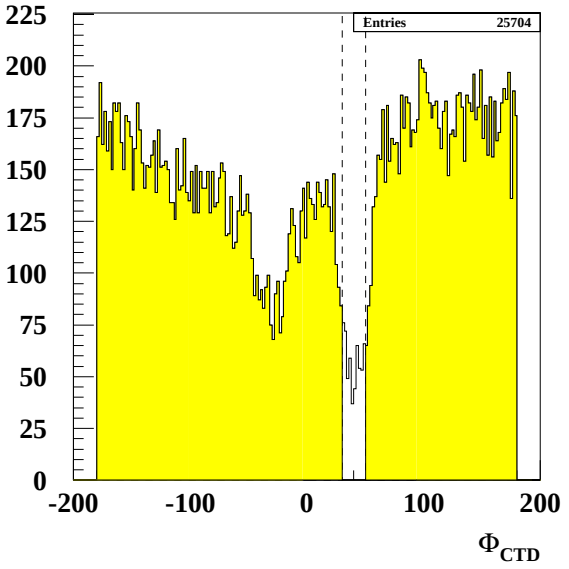

Figure 5.15: *The value of ϕ as measured by the CTD. The dead region due to dead and inefficient cells can be seen at* $30° < \phi < 45°$.

data. The fit to the data is displayed as a dashed line and the fit to the Monte Carlo is displayed as a solid line. The distributions have been normalised to the number of events seen in data. In all cases the fit agrees well with the shape of the distribution.

Figure 5.15 shows the azimuthal angular distribution of the CTD tracks for 1995 data. A loss of efficiency is seen in the angular range $30° < \phi < 50°$. Therefore, for 1995 data a cut was made to remove tracks in this angular range. The CTD tracks must also be reconstructed from more than 15 hits to ensure that a reliable CTD track is chosen[3].

From the fits in figures 5.16 and 5.17 it can be seen that the data distributions are offset from the Monte Carlo distributions which are themselves centered on zero. This shift is also seen to increase with momentum. The mean values from each fit have been plotted as a function of $|p_{CTD}|$ and $|p_{FMD}|$ in figure 5.18.

Comparing the CTD and FTD momentum measurements a systematic shift is observed which suggests that the FTD is underestimating the momentum of the tracks or alternatively the CTD is overestimating the momentum of the tracks.

[3]This cut was applied to 1995 data and 1996 data.

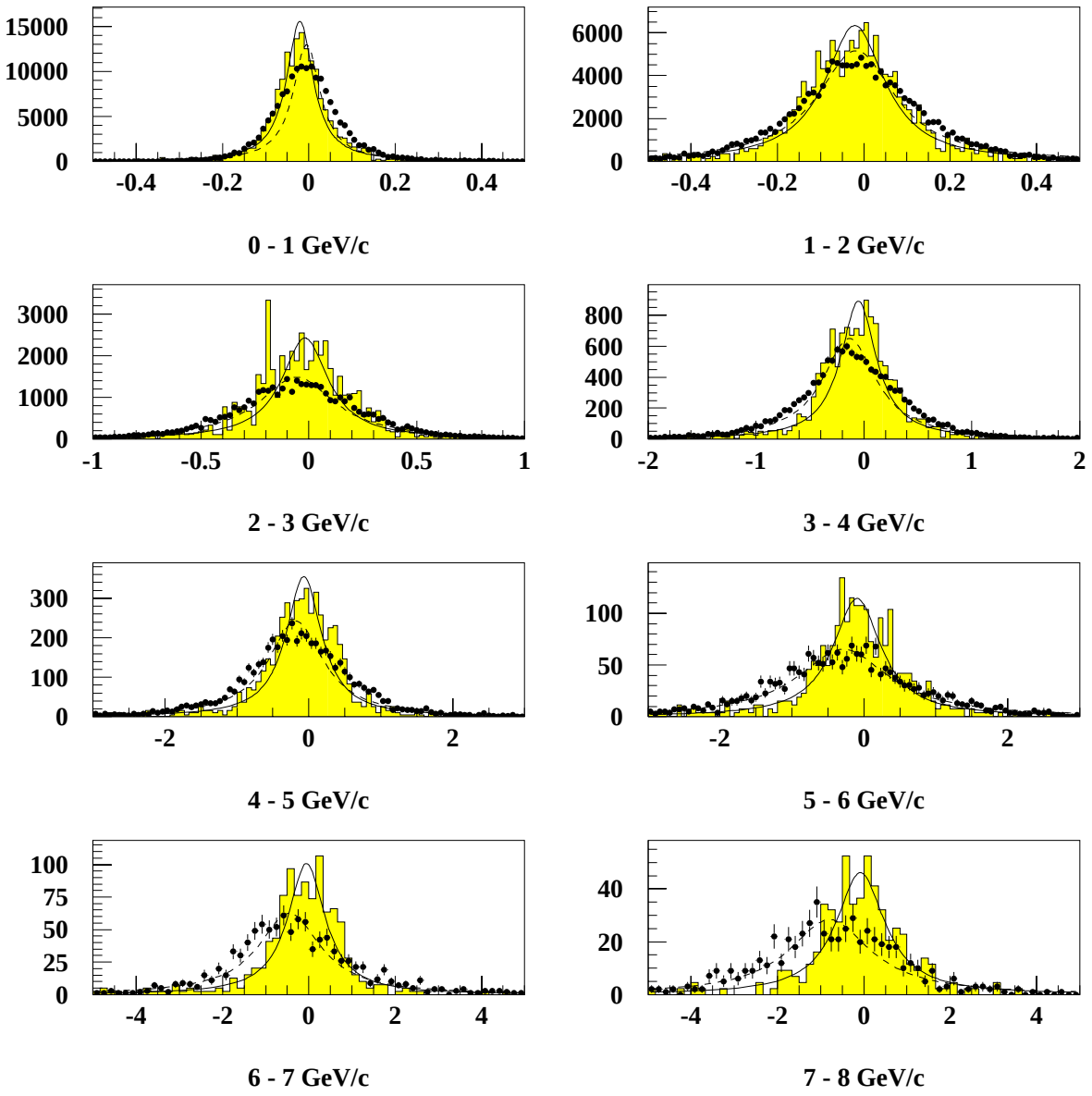

Figure 5.16: *Distributions showing* $|p_{FTD}|$-$|p_{CTD}|$ *as a function of the momentum measured by the CTD. The shaded histogram is the Monte Carlo distribution and the the fit is shown as the solid line. The points are the data distribution and the fit is shown as the dashed line.*

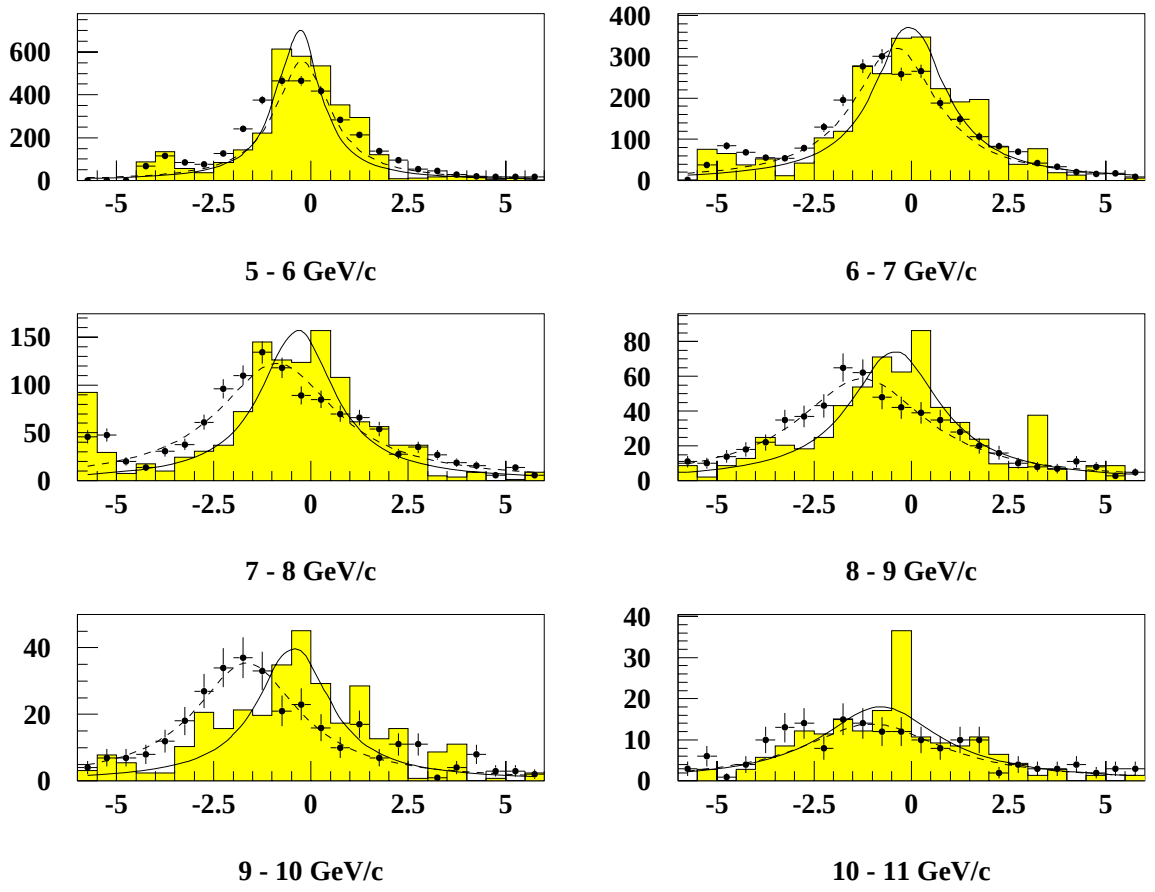

Figure 5.17: *Distributions showing* $|p_{FTD}|$-$|p_{FMD}|$ *as a function of the momentum measured by the FMD. The shaded histogram is the Monte Carlo distribution and the the fit is shown as the solid line. The points are the data distribution and the fit is shown as the dashed line.*

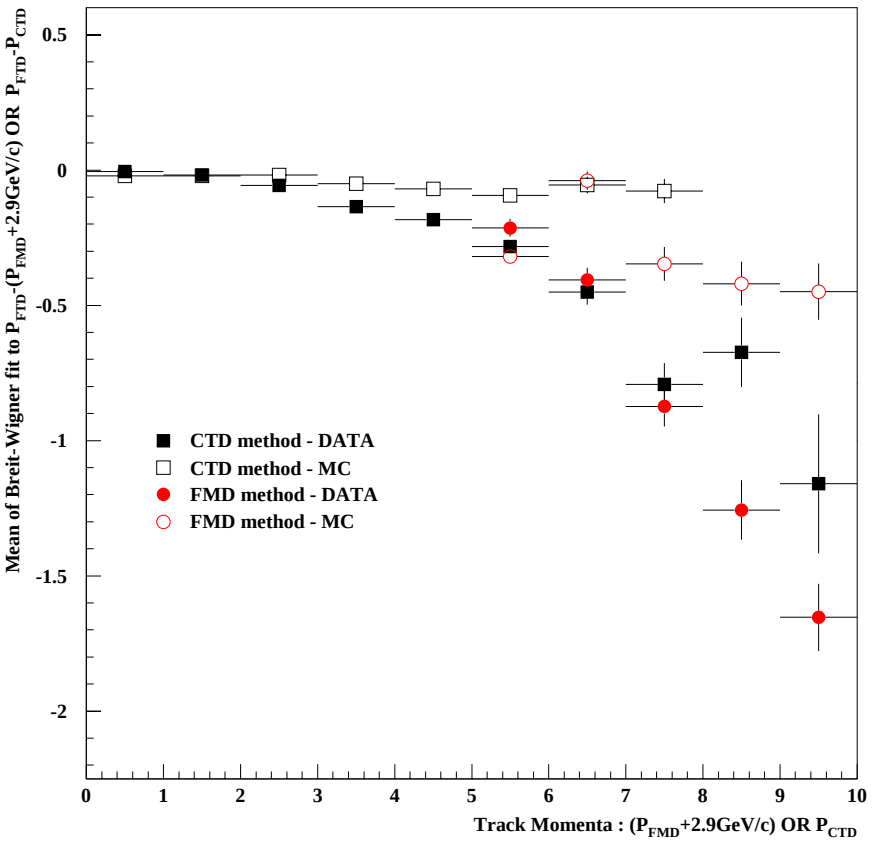

Figure 5.18: *The mean values of the Breit-Wigner fits applied to the distributions plotted in figures 5.16 and 5.17 are plotted against the momentum measured by the CTD or FMD for 1995 data. Method (1)* ($|p_{FTD}|$-$|p_{CTD}|$) *is represented by the square points and method 2* ($|p_{FTD}|$-$|p_{FMD}|$) *is represented by the circular points. Tracks of both charge are included.*

Comparing the FMD and the FTD momentum measurements a similar shift can be seen which again suggests that the FTD is underestimating the momentum of the track or that the FMD is overestimating the momentum. The two comparisons are independent apart from the common factor of the FTD which would indicate that the FTD is underestimating the momentum for vertex fitted tracks.

The Monte Carlo points in figure 5.18 show mean values centered approximately at zero. This is what would be expected in the data too if the detectors were measuring the momentum correctly.

If the FTD is indeed underestimating the momentum of the track then by comparing the data points of both methods it can be seen that the FMD results are in

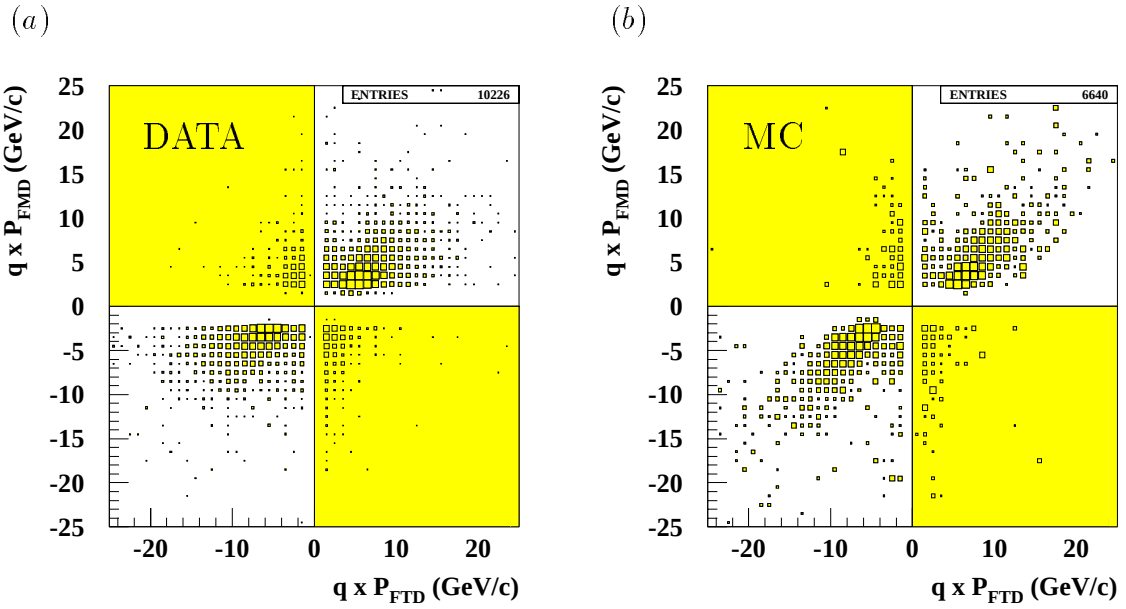

Figure 5.19: *Correlation plot showing the momentum measurement made by the FTD* (p_{FTD}) *against the momentum measurement made by the FMD* (p_{FMD}). *The shaded segments represent regions where muon tracks with different charges have been incorrectly linked.*

agreement with the results determined from the CTD. This is strong evidence that the FMD is reconstructing a track momenta reliably.

5.6.2 Wrong Sign Linking

It is possible for wrong sign tracks to be linked between the FTD and the FMD (method (2)). This can be investigated if the correlation plots shown in figure 5.1, (*b*) and (*d*), are replotted taking into account the charge of the track. As can be seen in figure 5.19 there are wrong sign combinations between the FTD and the FMD. This linking inefficiency can also be seen to be modelled by the Monte Carlo. It appears that the region containing falsely linked tracks of $|p_{FTD}| < 4\,\mathrm{GeV/c}$ also contains most of the wrong sign linked tracks, thus giving another reason why these tracks should be removed from this analysis. There are almost no cases of wrong sign tracks being linked between the FTD and the CTD.

5.6.3 Charge Ambiguities

All the previous distributions given for method (1) and method (2) have been for a combination of both positively and negatively charged tracks. When the tracks are separated according to their charge and the study is repeated, a marked difference is seen between the positive and the negative charged tracks. The distributions giving the difference in momentum for both methods and for each charge type can be seen in figures 5.20, 5.21, 5.22 and 5.23. Again, the distributions have been fitted using a Breit-Wigner function and they show a shift in the mean which differs in magnitude according to charge type. Figure 5.24 shows the mean differences plotted as a function of the momentum measured by the CTD or the FMD (+2.9 GeV/c) for positively charged tracks (a) and negatively charged tracks (b).

It is clear that there is a difference between the distributions for method (1) in particular. The trend that is seen for combined charges suggests that the FTD systematically underestimates the momentum of the track and this is still the suggested trend for positive tracks. However, negative tracks show a different behaviour in the mean of the distributions indicating a slight positive difference between the FTD and the CTD momentum. The deviation away from zero is small and appears to be constant over the whole CTD momentum range.

This last statement does not seem to be confirmed by the distributions for method (2), showing the mean differences between the momentum measured for tracks in the FTD and FMD. There appears to be an overall shift upwards in the mean difference for negatively charged tracks. However, there does not appear to be a 'flip' for positive tracks. For both cases there is substantial agreement between the Monte Carlo analyses.

Similar distributions have also been plotted for 1996 data after a new set of parameters describing the positioning of the FTD was inserted into the database to describe a twist effect in the FTD [56]. The mean values obtained from fitting the difference between the momentum determined by the FTD against that determined by the CTD or FMD are shown in figure 5.25. The results show that when a combination of both charges are plotted the mean of the distributions give a negative

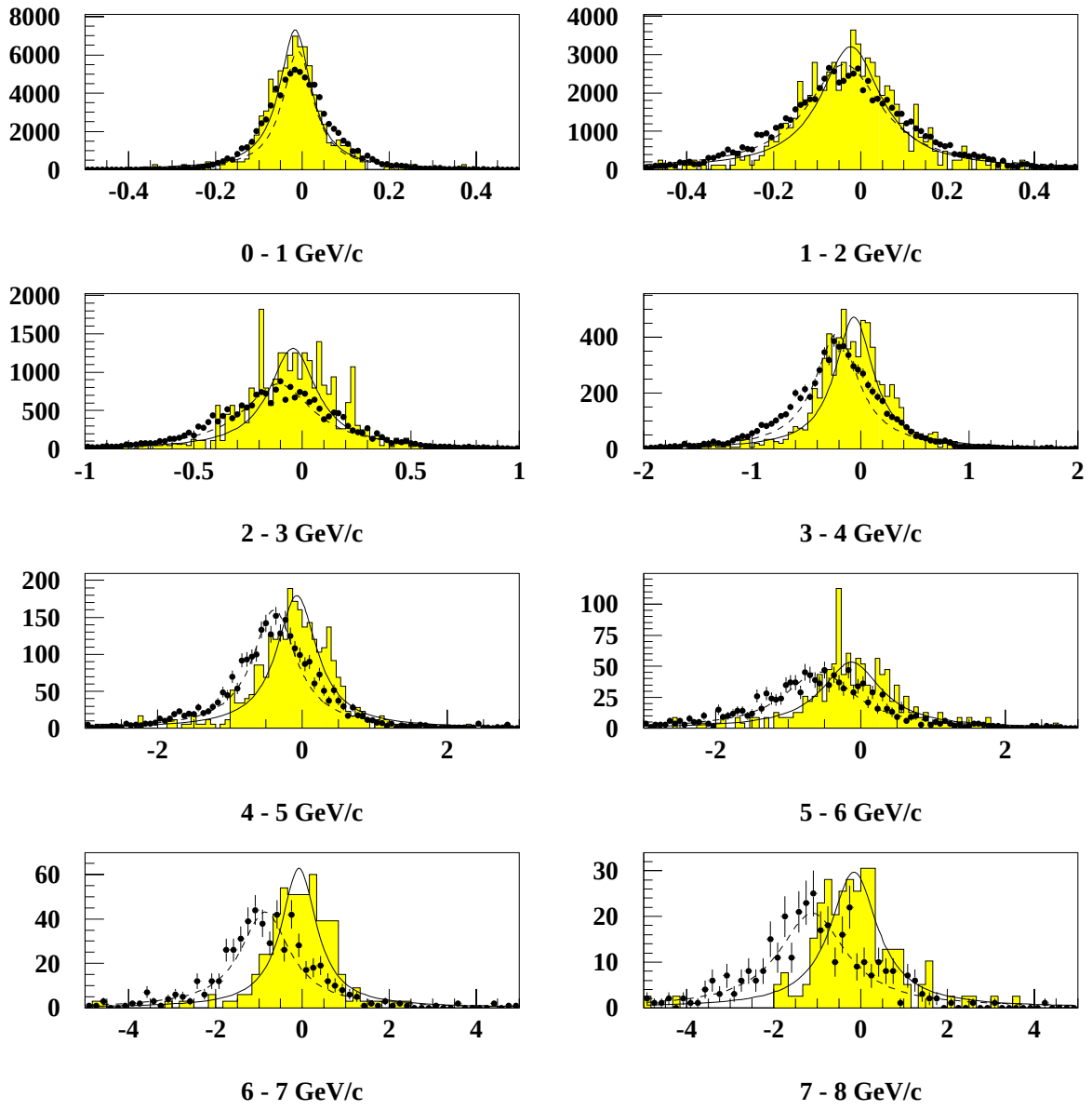

Figure 5.20: *Distributions showing* $|p_{FTD}|$-$|p_{CTD}|$ *as a function of the momentum measured by the CTD for positively charged tracks. The shaded histogram is the Monte Carlo distribution and the the fit is shown as the solid line. The points are the data distribution and the fit is shown as the dashed line.*

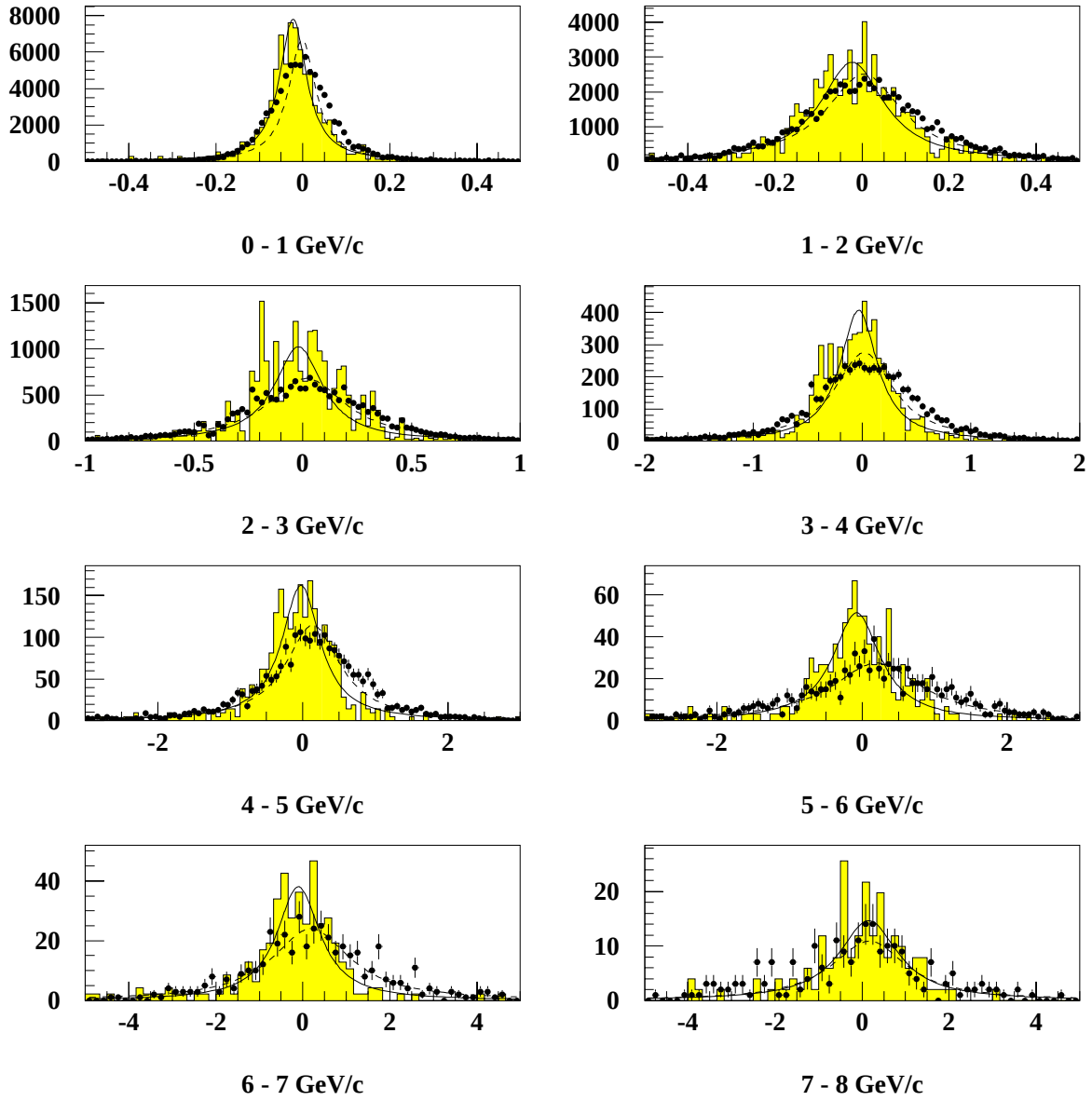

Figure 5.21: *Distributions showing* $|p_{FTD}|$-$|p_{CTD}|$ *as a function of the momentum measured by the CTD for negatively charged tracks. The shaded histogram is the Monte Carlo distribution and the the fit is shown as the solid line. The points are the data distribution and the fit is shown as the dashed line.*

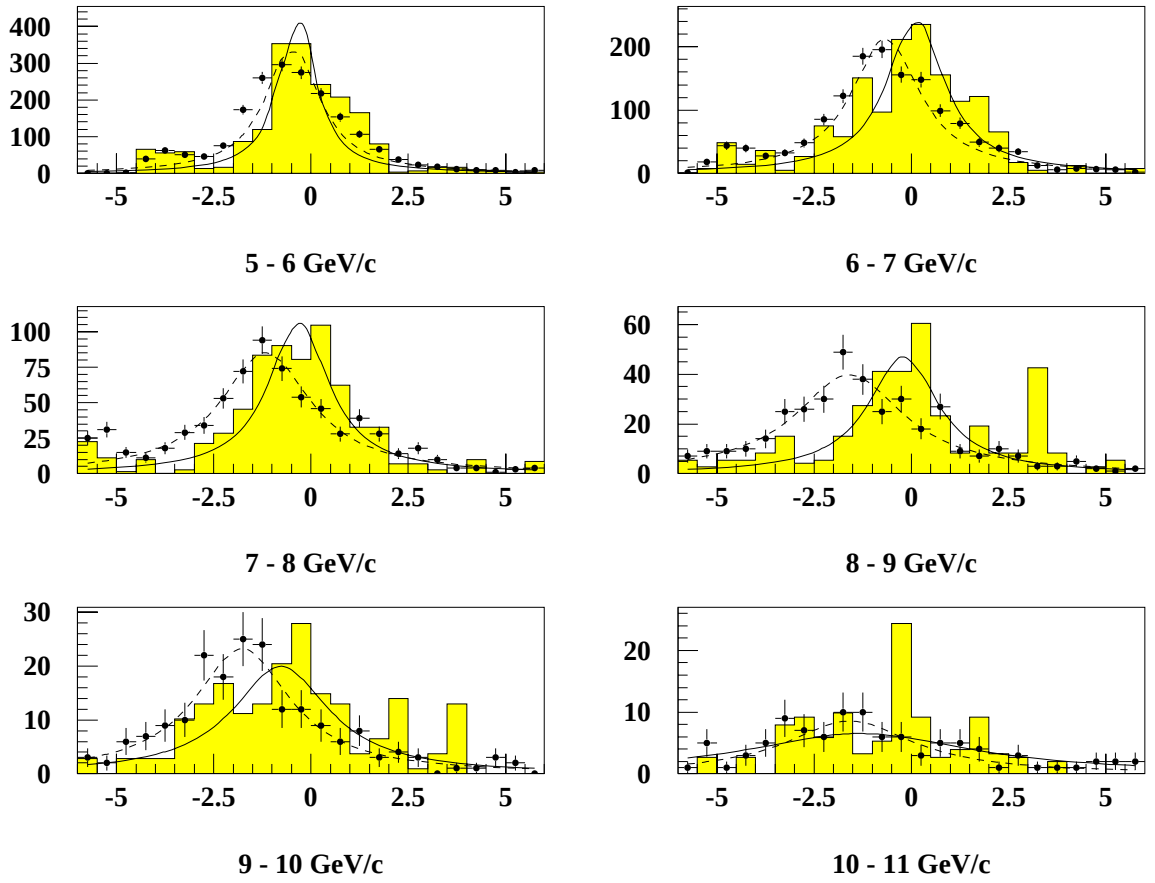

Figure 5.22: *Distributions showing* $|p_{FTD}|$-$|p_{FMD}|$ *as a function of the momentum measured by the FMD for positively charged tracks. The shaded histogram is the Monte Carlo distribution and the the fit is shown as the solid line. The points are the data distribution and the fit is shown as the dashed line.*

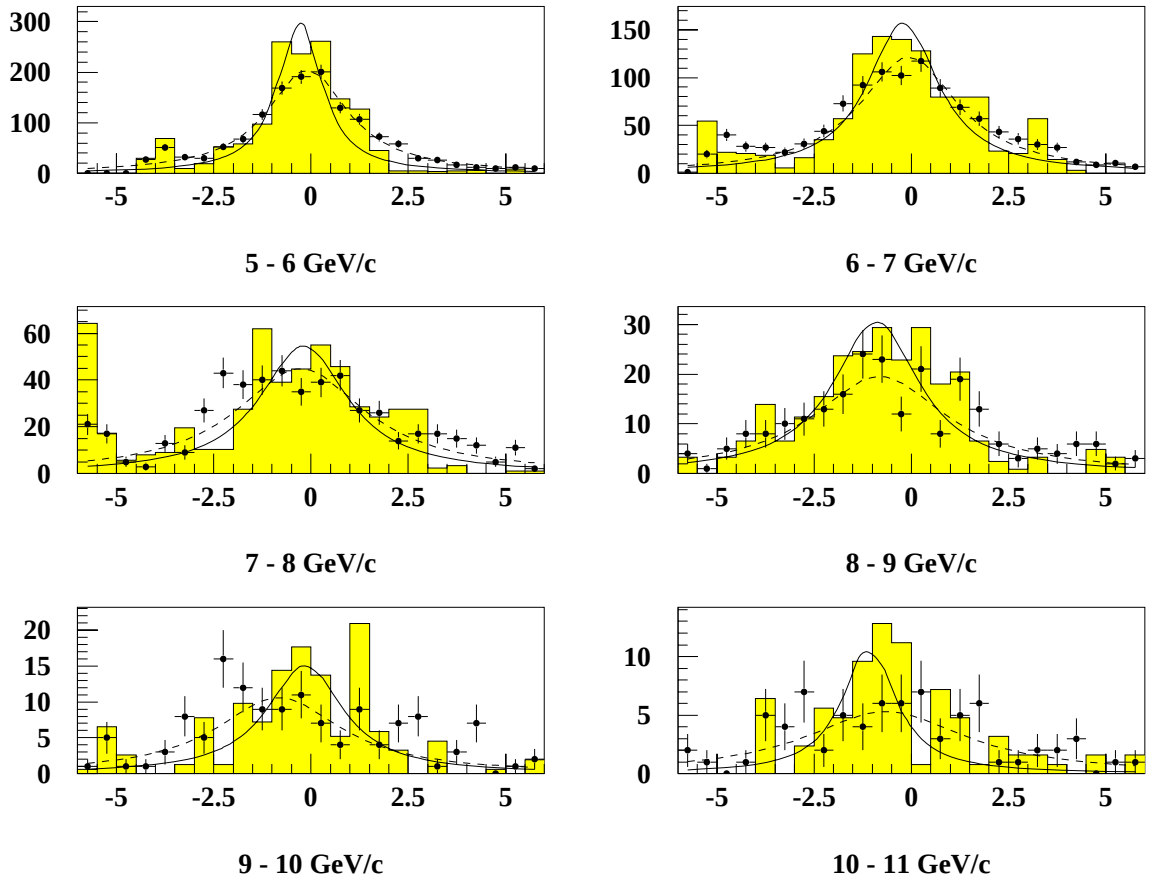

Figure 5.23: *Distributions showing* $|p_{FTD}|$-$|p_{FMD}|$ *as a function of the momentum measured by the FMD for negatively charged tracks. The shaded histogram is the Monte Carlo distribution and the the fit is shown as the solid line. The points are the data distribution and the fit is shown as the dashed line.*

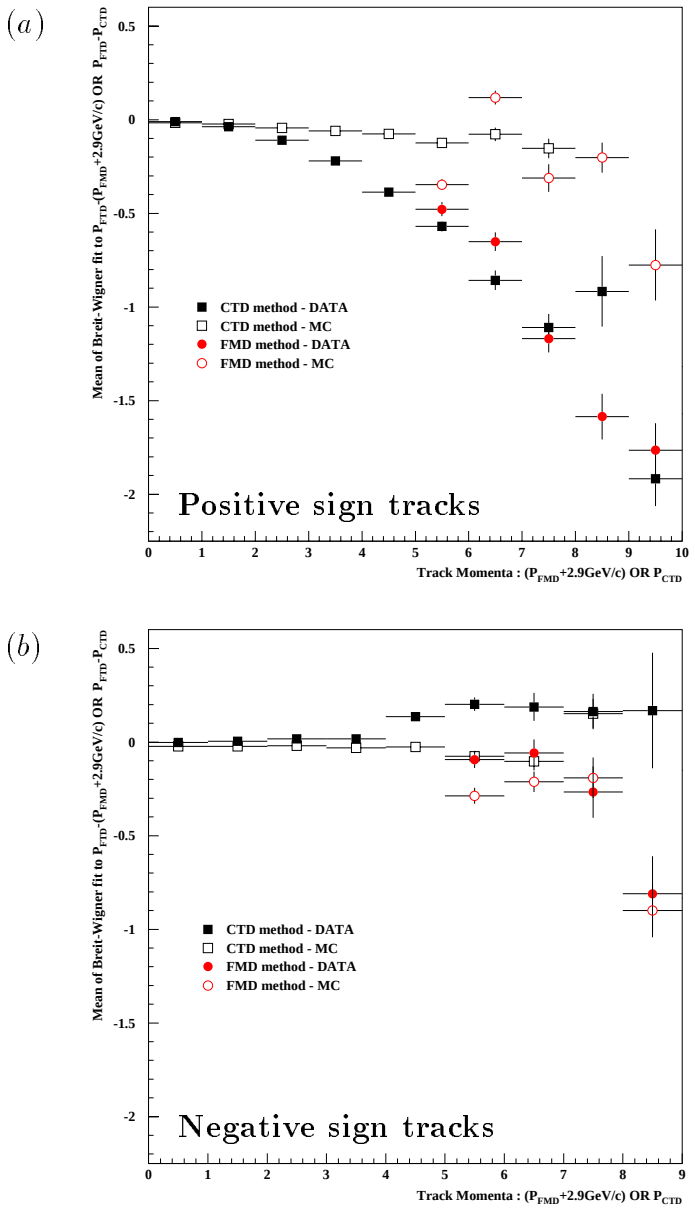

Figure 5.24: *The mean values of the Breit-Wigner fits applied to the distributions plotted in figures 5.20 and 5.22 and figures 5.21 and 5.23 have been plotted against the momentum measured by the CTD or FMD for 1995 data. Plot (a) represents positive sign tracks and plot (b) represents negative sign tracks. Method (1)* ($|p_{FTD}|$-$|p_{CTD}|$) *is represented by the square points and method (2)* ($|p_{FTD}|$-$|p_{FMD}|$) *is represented by the circular points.*

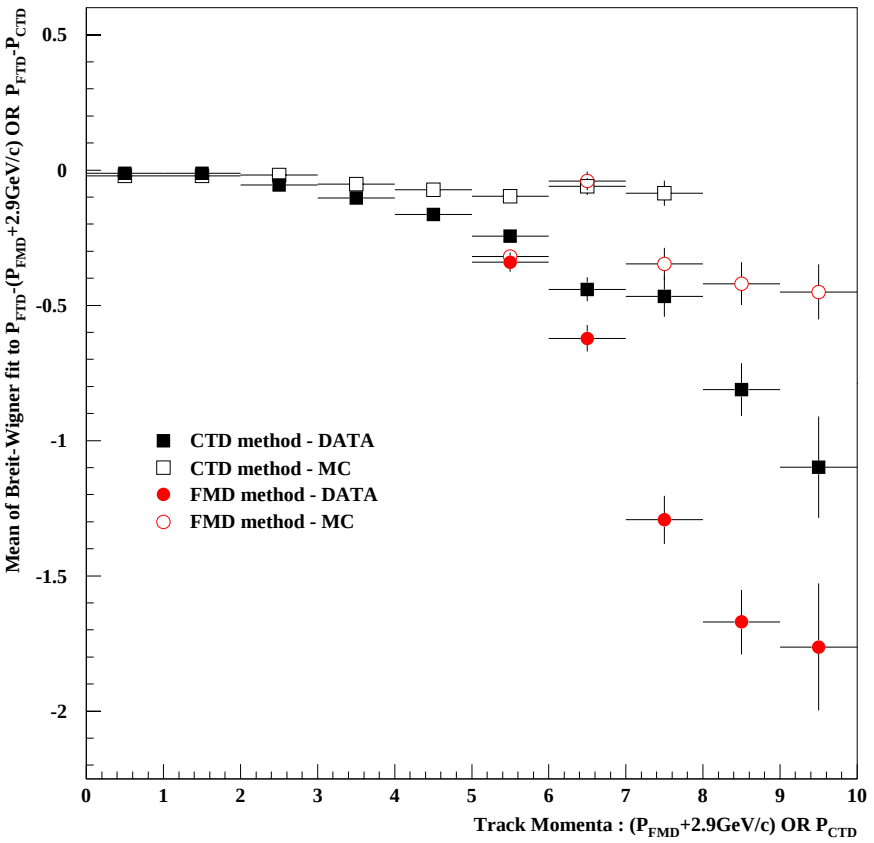

Figure 5.25: *The mean values of the Breit-Wigner fits applied to the distributions* ($|p_{FTD}|$-$|p_{CTD}|$ or $|p_{FTD}|$-$|p_{FMD}|$) *plotted against the momentum measured by the CTD or FMD for 1996 data. Method (1)* ($|p_{FTD}|$-$|p_{CTD}|$) *is represented by the square points and method 2* ($|p_{FTD}|$-$|p_{FMD}|$) *is represented by the circular points. Tracks of both charge are included.*

systematic shift, again suggesting that the FTD is underestimating the momentum of the reconstructed vertex fitted track.

When the mean values are plotted as a function of charge a dependence is again observed. Figure 5.26 shows the same data for 1996 as figure 5.25 but separated according to the charge of the track. The 1995 Monte Carlo results have been used because 1996 Monte Carlo was not available. In agreement with the 1995 analysis there is still a systematic shift for positive tracks, giving a negative mean difference. Within errors negative tracks give more consistent agreement with Monte Carlo for both methods.

From these results it appears that attempts to improve the discrepancies within

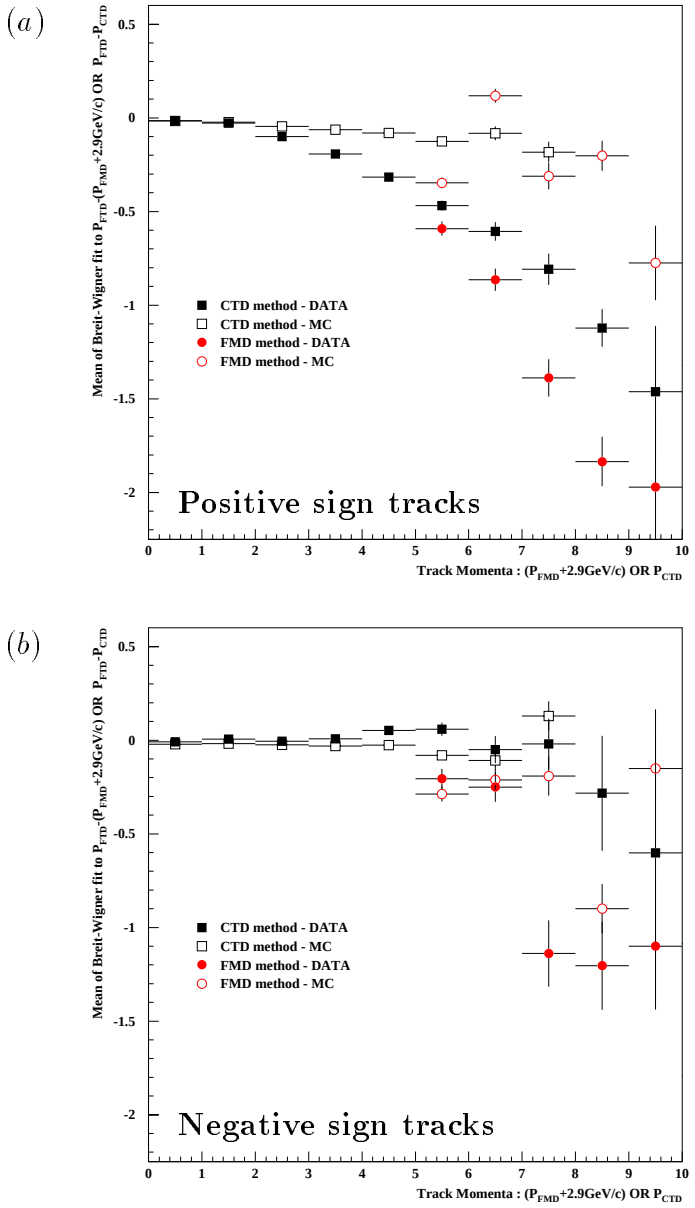

Figure 5.26: *The mean values of the Breit-Wigner fits applied to the distributions* $|p_{FTD}|$-$|p_{CTD}|$ and $|p_{FTD}|$-$|p_{FMD}|$ *plotted against the momentum measured by the CTD or FMD for 1996 data. Plot (a) represents positive sign tracks and plot (b) represents negative sign tracks. Method (1)* ($|p_{FTD}|$-$|p_{CTD}|$) *is represented by the square points and method (2)* ($|p_{FTD}|$-$|p_{FMD}|$) *is represented by the circular points.*

the reconstruction between 1995 and 1996 have not yielded substantial improvement. The results are in reasonable agreement between years but there is no simple explanation for the dependence on charge. In the following study attempts have been described which are aimed at taking into account these effects.

5.7 Momentum Correction Factors

The previous results have been put into a practical form by fitting a function to describe the systematic shifts in the momentum measured by the FTD as compared to the momentum measured by the CTD. The correction factors are found to be a function not only of charge but also the azimuthal angle[4]. Figures 5.28, 5.29, 5.30, and 5.31 show the FTD momentum deviation from the CTD momentum plotted for regions of azimuthal angle and for positive and negative sign tracks. The open circles are the Monte Carlo data and the closed circles are the data. The deviations have been plotted against the quantity $p_{CTD} - \Delta p$ which is the momentum measured by the FTD that can be determined from figures 5.18 and 5.25, where Δp is equal to the deviation ($|p_{FTD}|$-$|p_{CTD}|$).

The fits that have been made to the distributions provide the correction factors which can be applied to the momentum measured by the FTD for 1995 and 1996 data. The fits are polynomial functions of the form :

$$y = \sum_n A_n \ p_{FTD}^n \tag{5.2}$$

where n runs from 0 to 3. These coefficients A_n are listed in tables 5.3 and 5.4 for 1995 and 1996 data.

To test these correction factors they were applied to the FTD momentum measurement used to reconstruct the J/ψ mass for events containing forward going muons as studied in chapter 7. Events were selected from 1995 data and 1996 data which passed the quasi-elastic event selection cuts[5] described in chapter 7. These events contain two muons and describe the quasi-elastic decay of a J/ψ meson

[4]The ϕ value that is taken is measured by the CTD.

[5]To maximise the statistics the elastic cuts have not been applied.

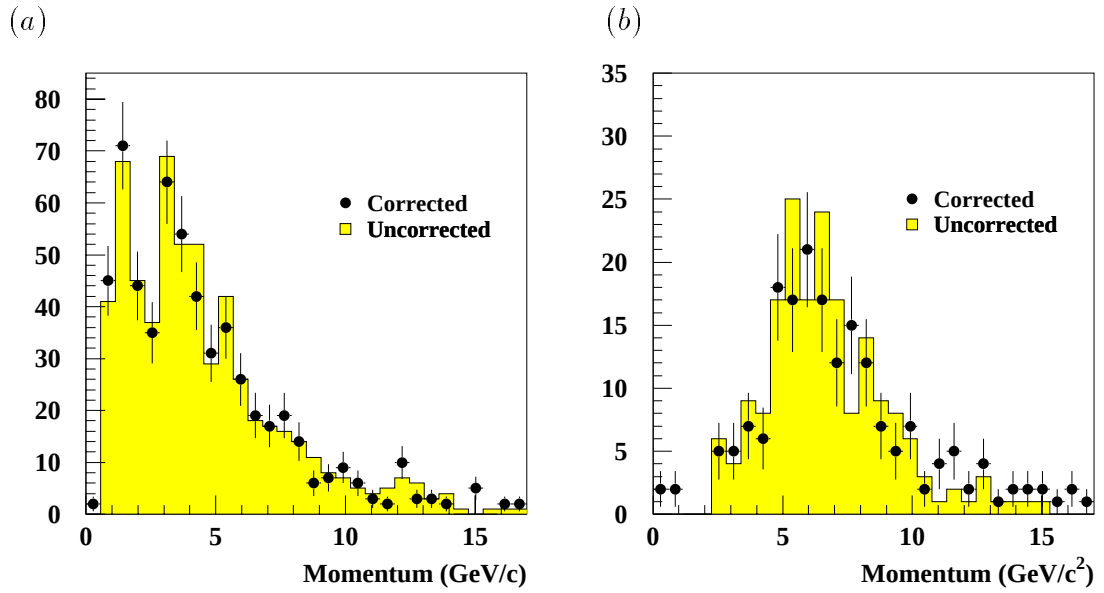

Figure 5.27: *Figure showing the momentum measured by the FTD for muon tracks resulting from the decay of a J/ψ meson. The event selection is described in chapter 7 and (a) shows events where one of the muons is found at $\theta < 20°$ and (b) shows events where both muons are found at $\theta < 20°$. The points represent the corrected momentum and the histogram is the momentum distribution before the correction factors are applied.*

through the muon decay branch. The quasi-elastic events have been separated into two event types as follows :

(1) One identified muon must be found in the angular range $\theta < 20°$ and other in the range $\theta > 20°$.

(2) Both identified muons must lie in the angular range $\theta < 20°$.

Due to the boost of a J/ψ resonance produced in the forward direction, the muons from the $J/\psi \rightarrow \mu^+\mu^-$ decay are often high momentum tracks. The momentum distribution for each event type can be seen in figure 5.27. There are more high momentum tracks for the two forward going muons sample (2), however high momentum muons are also observed within the one forward going muon sample (1).

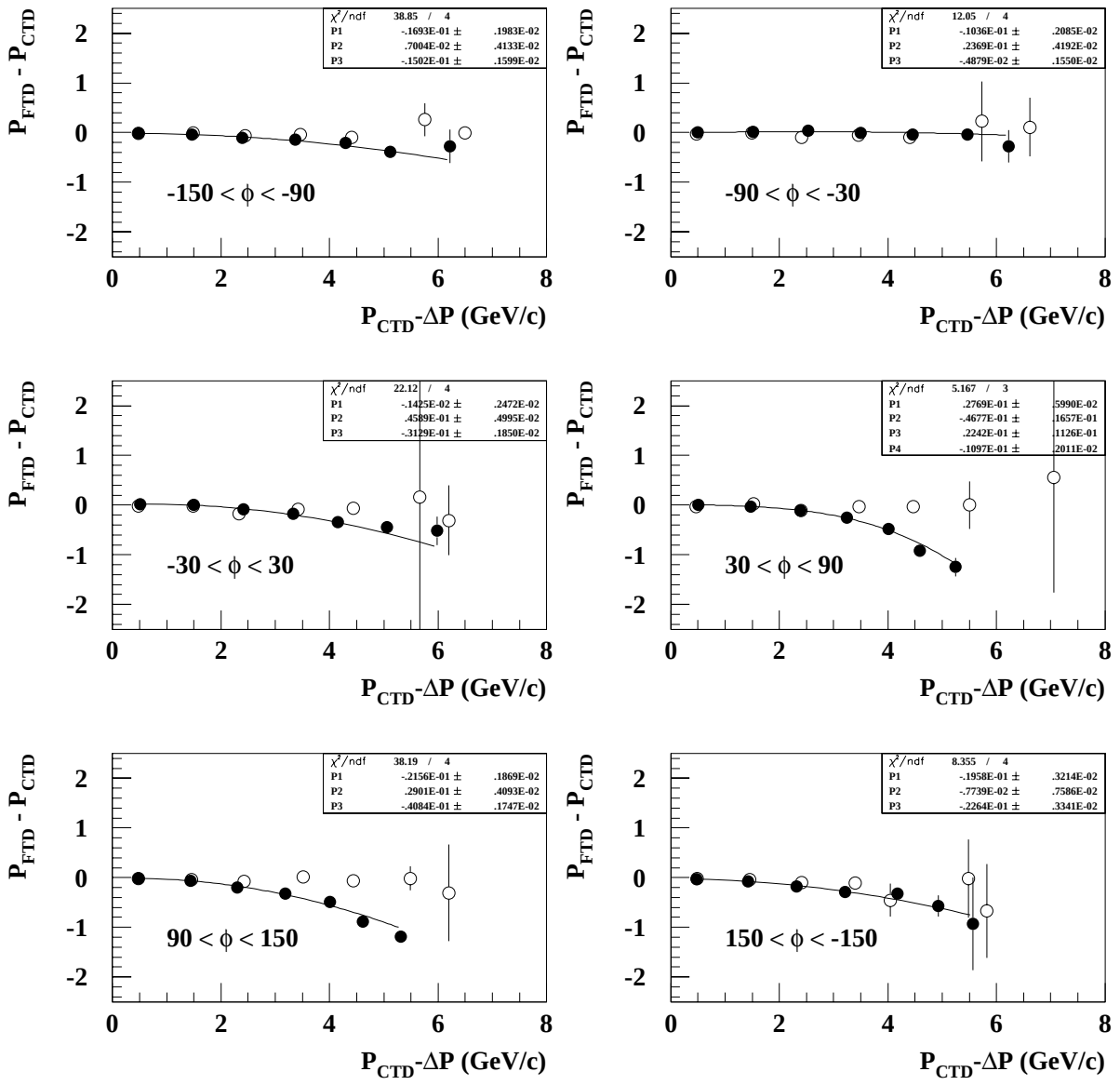

Figure 5.28: *Correction factors for 1995 data for positively charged tracks. The correction factors are seen to differ according to the range of ϕ that is chosen.*

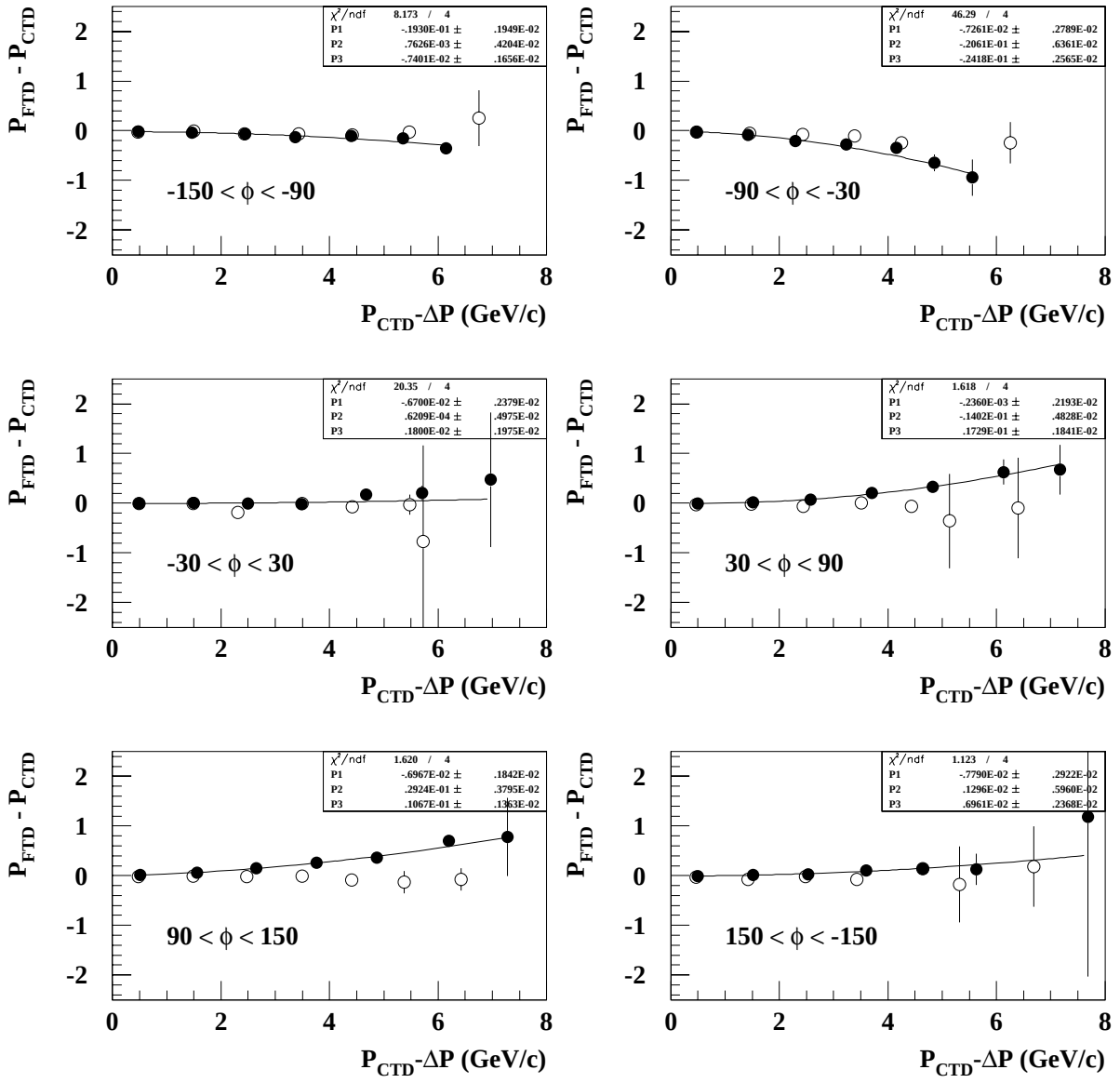

Figure 5.29: *Correction factors for 1995 data for negatively charged tracks. The correction factors are seen to differ according to the range of ϕ that is chosen.*

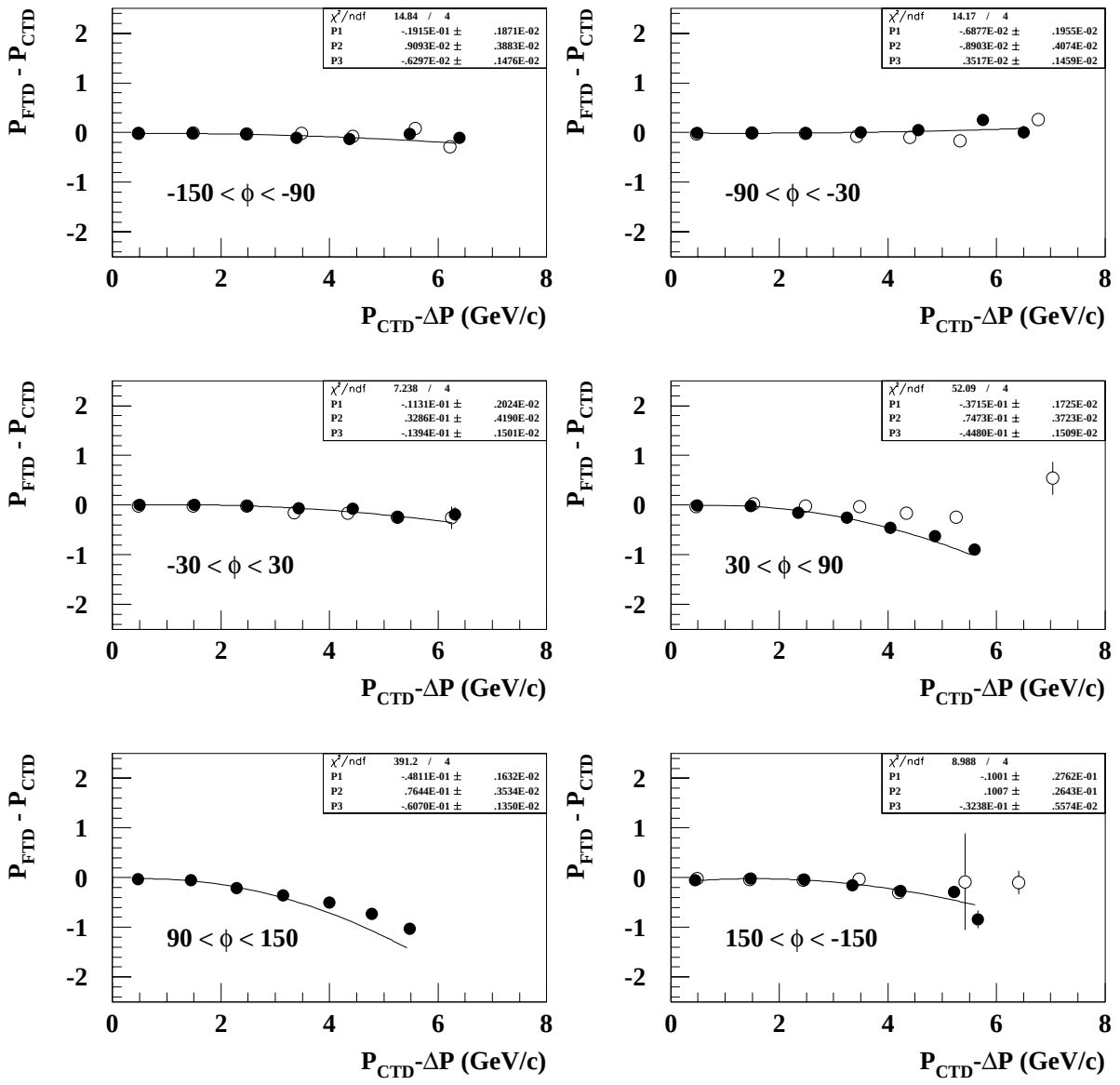

Figure 5.30: *Correction factors for 1996 data for positively charged tracks. The correction factors are seen to differ according to the range of ϕ that is chosen.*

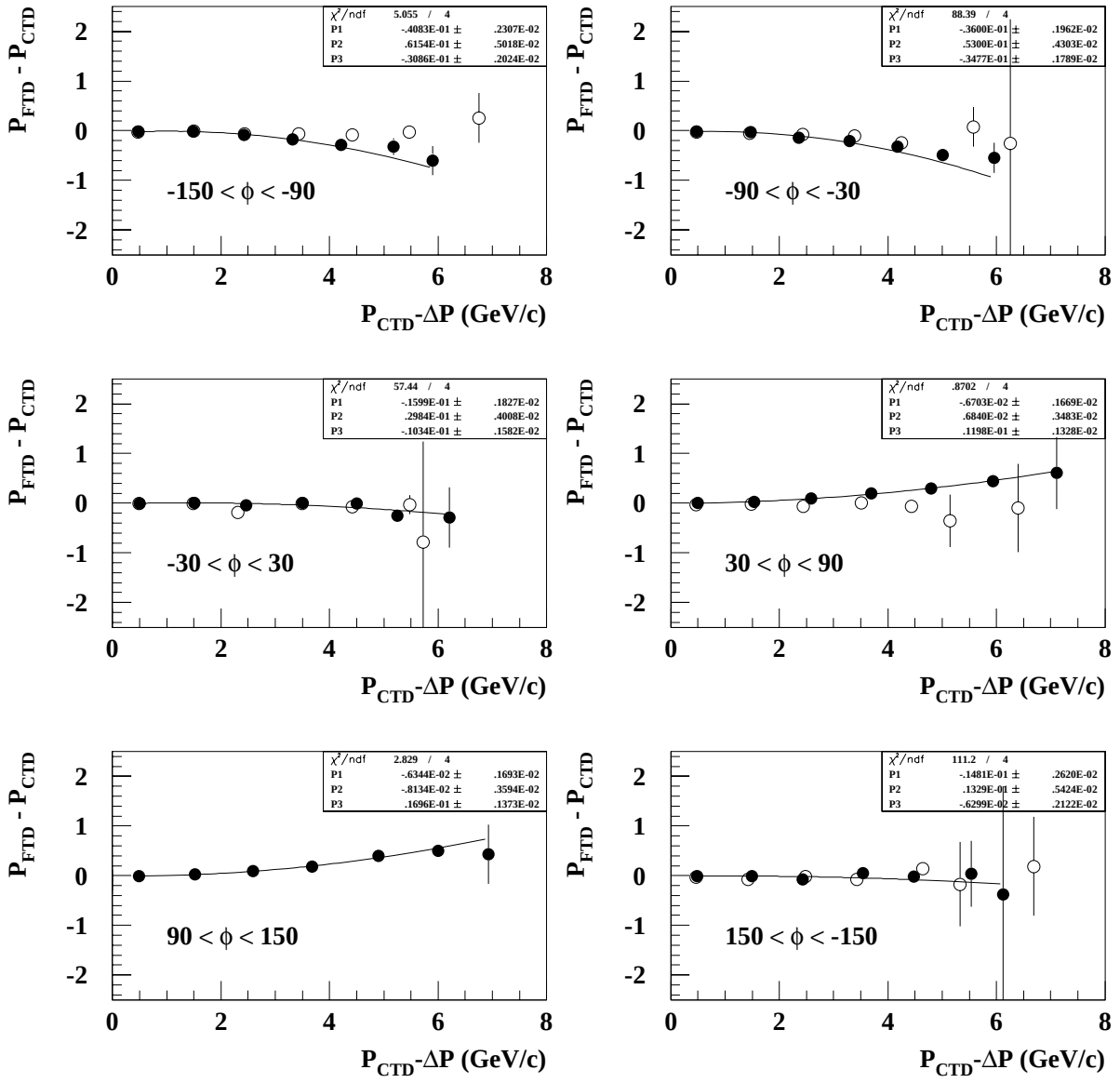

Figure 5.31: *Correction factors for 1996 data for negatively charged tracks. The correction factors are seen to differ according to the range of ϕ that is chosen.*

For vertex fitted tracks reconstructed by the FTD the momentum measurement has been corrected and this distribution is given by the points. For both event types the momentum correction does not change the distributions significantly. However, for the two forward going muons sample (2) the corrected distribution shows an increased population in high momentum tracks. This is be expected as it has been shown that the FTD tends to underestimate the track momentum and this effect increases with the track momentum.

Figures 5.32 (a) and (b) contain events where only one muon is found at $\theta < 20°$ and the other is found at $\theta > 20°$ and figures 5.32 (c) and (d) contain events where both muons are found at $\theta < 20°$. Plots (a) and (c) show the reconstructed dimuon invariant mass before the momentum measured by the FTD is corrected and plots (b) and (d) show the dimuon invariant mass after the corrections to the momentum have been made. The data for both years have been combined and the appropriate correction factors given by tables 5.3 and 5.4 applied.

A Gaussian fit to the peak and a fit to the background has been made to the invariant masses in figure 5.32. The mean of the Gaussian fits are seen to differ between (a) and (b), and (c) and (d). The values of the mean and width of the distributions before and after the correction factors are applied are given in table 5.5. The current world average value for the mass of the J/ψ resonance is $3.086\,\mathrm{GeV/c^2}$. The J/ψ resonance corresponding to event type (1) gives a mean that is consistent with the world average before and after the correction factor is applied. The J/ψ resonance corresponding to event type (2) gave a mean which was lower than the world average by approximately 270 MeV before the correction factor was applied. This shift improves significantly after the corrections to the momentum have been made and the new mean of the distribution is now consistent with the world average. The width of the peaks have narrowed slightly indicating an improvement in the resolution.

Another way in which to correct the momentum used to calculate the invariant mass of the J/ψ is by using the momentum measured by the FMD. It was shown in figures 5.18 and 5.25 that the deviation in the momentum measured by the FTD

-150 < ϕ < -90				
	1995		1996	
	$p_{FTD} > 0$	$p_{FTD} < 0$	$p_{FTD} > 0$	$p_{FTD} < 0$
A_0	-0.01693	-0.0193	-0.01915	-0.04083
A_1	0.007	0.00076	0.00909	0.06154
A_2	-0.0015	-0.0074	-0.006297	-0.03086

-90 < ϕ < -30				
	1995		1996	
	$p_{FTD} > 0$	$p_{FTD} < 0$	$p_{FTD} > 0$	$p_{FTD} < 0$
A_0	-0.01036	-0.007261	-0.006877	-0.036
A_1	0.02369	-0.02061	-0.008903	0.053
A_2	-0.004879	-0.02418	0.003517	-0.03477

-30 < ϕ < 30				
	1995		1996	
	$p_{FTD} > 0$	$p_{FTD} < 0$	$p_{FTD} > 0$	$p_{FTD} < 0$
A_0	-0.001425	-0.0067	-0.01131	-0.01599
A_1	0.04589	0.000062	0.03286	0.02984
A_2	-0.03129	0.0018	-0.01394	-0.01034

Table 5.3: *Coefficients obtained from fitting n (n=0,3) degree polynomials to the distributions shown in figures 5.28, 5.29, 5.30 and 5.31.*

$30 < \phi < 90$				
	1995		1996	
	$p_{FTD} > 0$	$p_{FTD} < 0$	$p_{FTD} > 0$	$p_{FTD} < 0$
A_0	0.02769	-0.00024	-0.03715	-0.006703
A_1	-0.04677	-0.01402	0.07473	0.00684
A_2	0.02242	0.01729	-0.0448	0.01198
A_3	-0.01097	0.0	0.0	0.0

$90 < \phi < 150$				
	1995		1996	
	$p_{FTD} > 0$	$p_{FTD} < 0$	$p_{FTD} > 0$	$p_{FTD} < 0$
A_0	-0.02156	-0.006967	-0.04811	-0.006344
A_1	0.02901	0.02924	0.7644	-0.008134
A_2	-0.04084	0.01067	-0.0607	0.01696

$150 < \phi <$ -150				
	1995		1996	
	$p_{FTD} > 0$	$p_{FTD} < 0$	$p_{FTD} > 0$	$p_{FTD} < 0$
A_0	-0.01958	-0.00779	-0.1001	-0.01481
A_1	-0.007739	0.0013	0.1007	0.01329
A_2	-0.02264	0.006961	-0.03238	-0.006299

Table 5.4: *Coefficients obtained from fitting n (n=0,3) degree polynomials to the distributions shown in figures 5.28, 5.29, 5.30 and 5.31.*

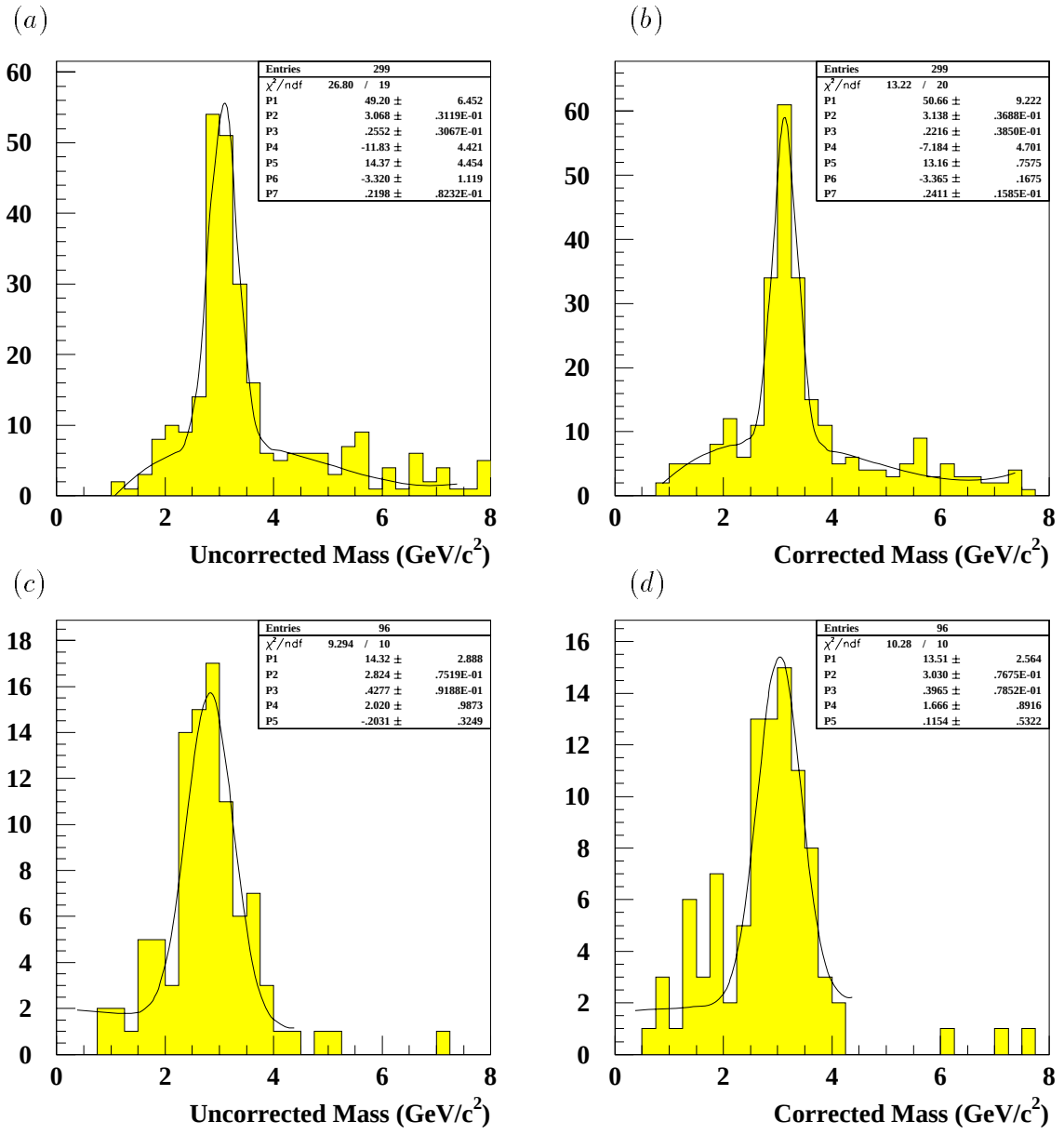

Figure 5.32: *The reconstructed invariant mass of a J/ψ resonance for the decay $J/\psi \to \mu^+\mu^-$ where one of the muons is found at $\theta < 20°$ and the other at $\theta > 20°$ ((a) and (b)) and both are found at $\theta < 20°$ ((c) and (d)). Figures (b) and (d) are the invariant masses after the momentum measured by the FTD is corrected using the functions shown in figures 5.28, 5.29, 5.30 and 5.31. Figures (a) and (c) are the invariant masses before the the correction.*

	One Forward μ		Two Forward μ's	
	Uncorrected Mass	Corrected Mass	Uncorrected Mass	Corrected Mass
Mean	3.07 ± 0.03	3.14 ± 0.04	2.82 ± 0.08	3.03 ± 0.08
Width	0.26 ± 0.03	0.22 ± 0.04	0.43 ± 0.09	0.40 ± 0.08

Table 5.5: *The values of the mean and width of the J/ψ resonances plotted in figure 5.32 before and after the correction factors have been applied.*

compared to the momentum measured in the CTD and FMD give comparable results thus this method is justifiable. The invariant masses can be recalculated using the momentum measured by the FMD for when a FMD muon track exists[6]. The results can be seen in figures 5.33 and 5.34 which display 1995 data only. Plots (a) and (b) are the invariant masses calculated using the momentum measured by the FTD before and after the correction factors for 1995 data have been applied. Plot (c) shows the recalculated invariant mass using the momentum measured by the FMD. The momentum distribution of the muon tracks used when calculating the invariant mass is shown in plot (d). The shaded histogram represents the proportional of muon tracks detected by the FMD. The values of the mean and width of the distributions plotted in figures 5.33 and 5.34 are given in table 5.6. The most significant result is that the mean of the invariant mass calculated for two forward going muons has shifted closer towards the accepted J/ψ mass when the momentum measured by the FMD is used. The momentum measured by the FTD for vertex fitted tracks must therefore require a further correction which has not been determined here. Therefore, the momentum measured by the FMD will be taken in favour of the momentum measured by the FTD when calculating the invariant mass of the J/ψ meson.

[6]If a FMD muon track does not exist the momentum measured by the FTD is taken

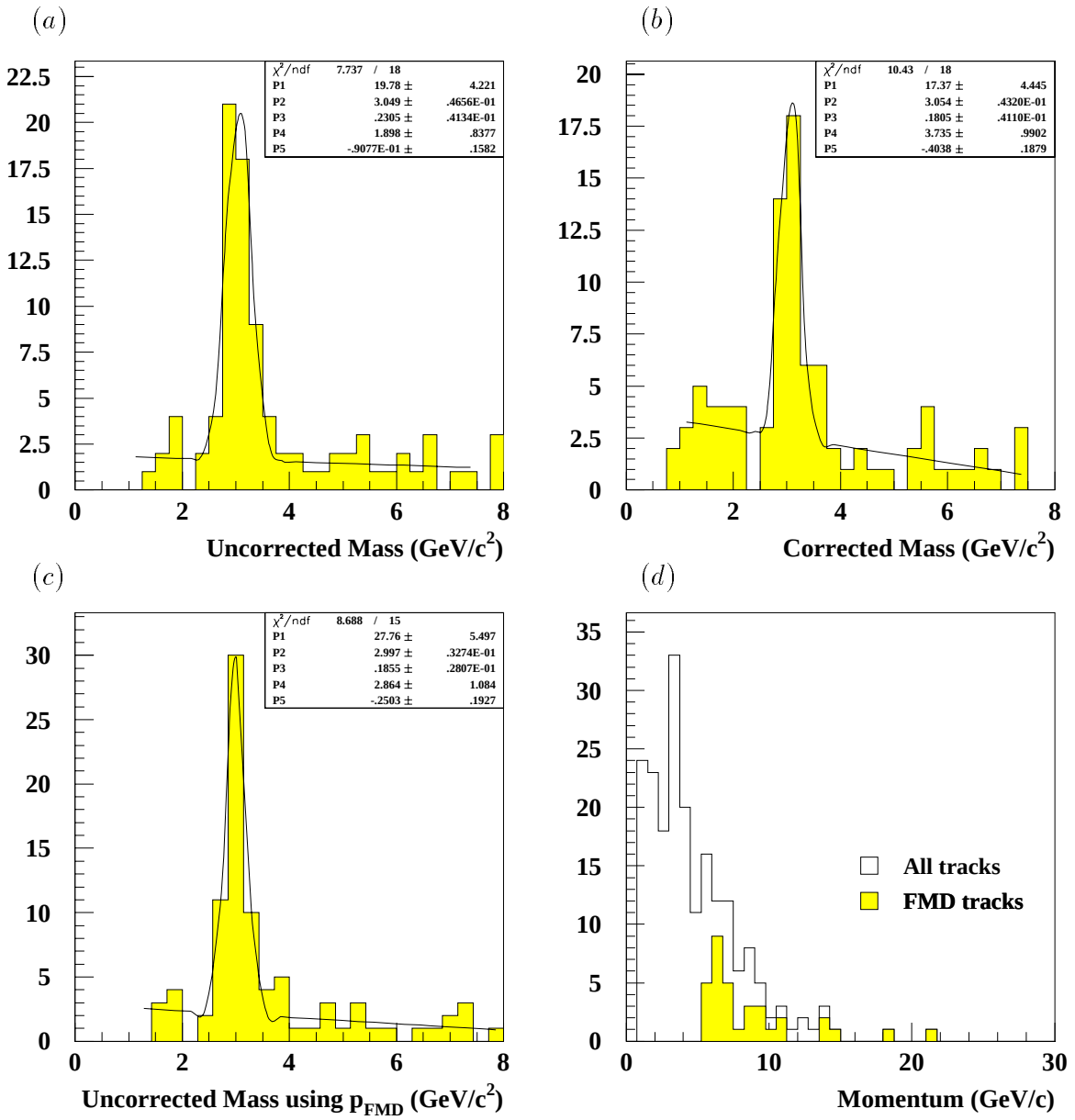

Figure 5.33: *The reconstructed invariant mass of a J/ψ resonance for the decay $J/\psi \to \mu^+\mu^-$ where one of the muons is found at $\theta < 20°$ and the other at $\theta > 20°$ for 1995 data. Figures (a) and (b) are the invariant masses before and after the momentum measured by the FTD is corrected using the functions in figures 5.28 and 5.29. Figure (c) is the invariant mass before the correction is applied but using the momentum measured by the FMD for when a FMD muon exists. Figure (d) shows the momentum distribution of the muon tracks. The proportion of FMD muon tracks is shown by the shaded histogram.*

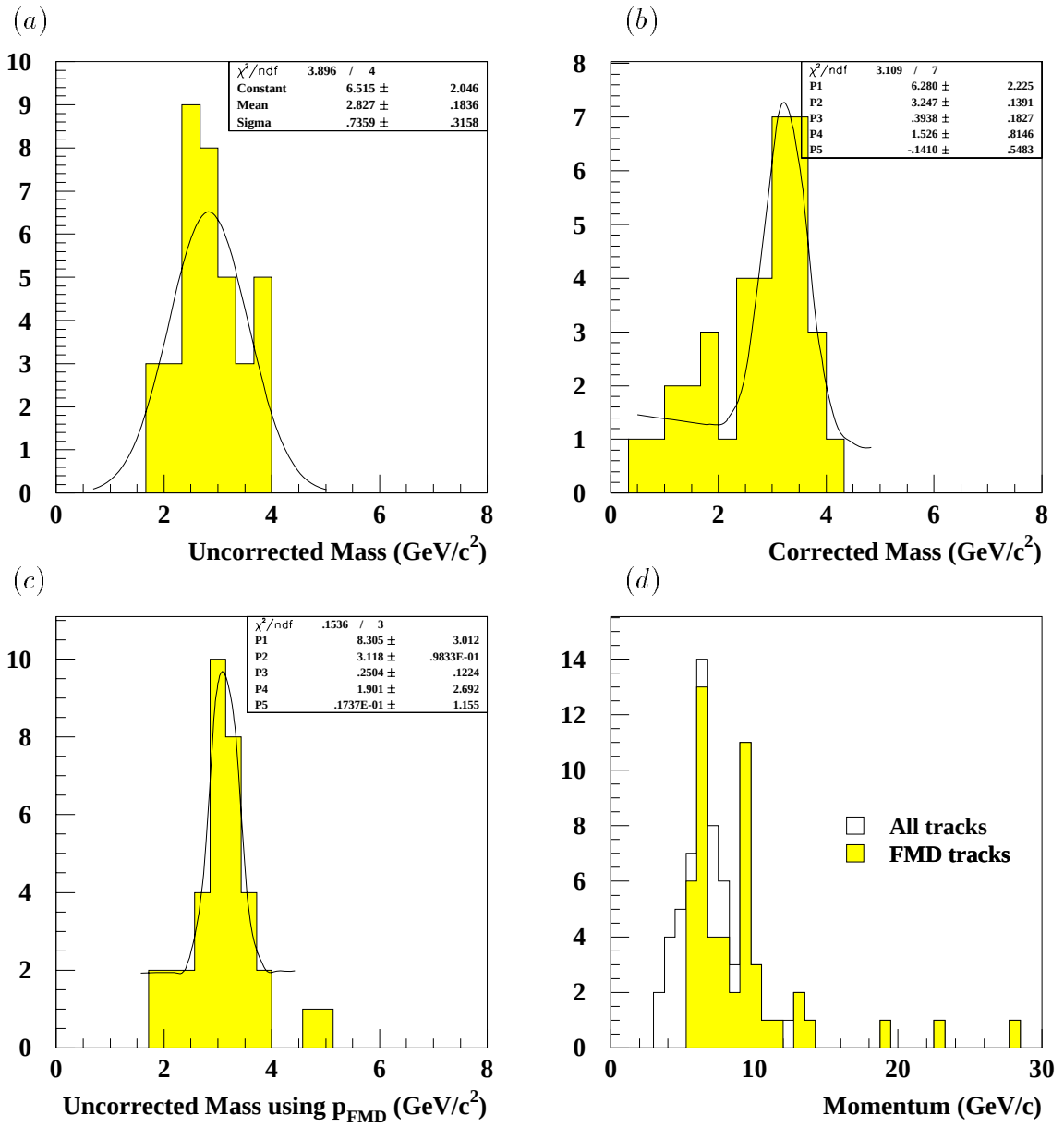

Figure 5.34: *The reconstructed invariant mass of a J/ψ resonance for the decay $J/\psi \to \mu^+\mu^-$ where both of the muons are found at $\theta < 20°$ for 1995 data. Figures (a) and (b) are the invariant masses before and after the momentum measured by the FTD is corrected using the functions in figures 5.28 and 5.29. Figure (c) is the invariant mass before the correction is applied but using the momentum measured by the FMD for when a FMD muon exists. Figure (d) shows the momentum distribution of the muon tracks. The proportion of FMD muon tracks is shown by the shaded histogram.*

	One Forward μ		
	Uncorrected Mass (only p_{FTD} used)	Corrected Mass (only p_{FTD} used)	Uncorrected Mass (p_{FTD} and p_{FMD} used)
Mean	3.05 ± 0.05	3.05 ± 0.04	3.0 ± 0.03
Width	0.23 ± 0.04	0.18 ± 0.04	0.185 ± 0.03

	Two Forward Going μ's		
	Uncorrected Mass (only p_{FTD} used)	Corrected Mass (only p_{FTD} used)	Uncorrected Mass (p_{FTD} and p_{FMD} used)
Mean	2.83 ± 0.18	3.24 ± 0.14	3.12 ± 0.25
Width	0.74 ± 0.32	0.39 ± 0.18	0.25 ± 0.12

Table 5.6: *The values of the mean and width of the J/ψ resonances plotted in figure 5.32 before and after the correction factors have been applied.*

5.8 Conclusion

It has been shown that the momentum measured by the FTD is systematically underestimated when the charge of the track is ignored. In addition systematic shifts dependent on the sign of charge and azimuthal angle are seen. An attempt is made to correct the momentum measured by the FTD by quantifying these results. Before corrections are made the dimuon mass distributions peak at $3.07\,GeV/c^2$ and $2.82\,GeV/c^2$ for events with one forward going muon and two forward going muons respectively. After correcting the momentum measured by the FTD the peaks move to $3.14\,GeV/c^2$ and $3.03\,GeV/c^2$. In both cases the peaks are seen to be narrower.

Finally for events where a momentum measurement can be made using the FMD the dimuon mass distributions peak at $3.0\,GeV/c^2$ and $3.12\,GeV/c^2$ for events with one forward going muon and two forward going muons respectively. It has therefore been shown that if the momentum measured by the FMD is used to calculate the invariant mass the mean of the distribution is in agreement with the mean obtained from correcting the momentum measured by the FTD with the correction factors

given in tables 5.3 and 5.4. On the basis of how well the observed dimuon mass spectrum agrees with the accepted J/ψ mass it appears that both methods give a satisfactory solution in obtaining a correct momentum value for vertex fitted tracks reconstructed in the forward direction.

Chapter 6

Detector and Trigger Efficiency Studies

This chapter presents a study of the track reconstruction detection and the triggering efficiency of a muon travelling in the forward direction. This is necessary when measuring the production of elastic J/ψ mesons as described in chapter 7. The overall acceptance for an elastic J/ψ event decaying to a $\mu^+\mu^-$ pair has been determined using the Monte Carlo. However, in order for this acceptance to be meaningful, the individual efficiencies for triggering, track reconstruction and linking have to be determined from the data and the Monte Carlo simulation to check they are in good agreement.

The L1 subtriggers that have triggered the event samples described in section 7.1.1 have been listed in tables 7.1 and 7.2. These trigger elements will be also studied in this chapter. To summarise the following track reconstruction efficiencies and trigger efficiencies have been determined :

- The Forward Muon Detector (FMD) and Trigger (FMT) efficiencies ;
- The Forward Iron End-Cap Detector and Trigger efficiencies ;
- The Z-Vertex Trigger and the Topological Trigger efficiencies.

For those cases in which the Monte Carlo does not agree well with the data corresponding correction factors must be applied to the Monte Carlo before it can

be used to calculate the overall acceptance. The differences between the efficiencies determined using the Monte Carlo and the data are taken into account when assigning a systematic uncertainty to the overall acceptance.

6.1 The Forward Muon Detector Track Reconstruction and Trigger Efficiency

1995 was the first year that a measurement of the track reconstruction and linking efficiency of the FMD was made. During 1994 data taking the FMD was seriously affected by synchrotron radiation from the positron beam. This had caused problems with the currents drawn from the post-toroid layers of the FMD and as a result the FMD was not operational at the optimal voltage for a large proportion of the collected luminosity. Hence it was not possible to calculate the track reconstruction and linking efficiencies associated with the detector for that year's data taking.

In order to calculate both the track reconstruction efficiency of the FMD and the trigger efficiency of the FMT a sample of events is required which is independent of the FMD and the FMT[1]. Class 24 events (see section 4.1) were chosen which contained at least one forward going muon with the proviso that the classification had not resulted from the FMD muon alone. The sample is made independent of the FMT by requiring that they have been triggered by a different subtrigger. Such events are typically triggered by electron tagger or Spacal triggers.

It is also essential that the FTD momentum determination for vertex fitted tracks is reliable for these tracks if they are to be used in calculating the FMD track reconstruction efficiency and this was the motivation for the work in the chapter 5. It has been shown that the momentum of the FTD tracks must be at least $p_{FTD} > 4\,GeV/c$ if the muon is to pass through the iron, LAr and traverse the FMD toroid to be reconstructed as a FMD track. If the FTD repeatedly overestimates the momentum measurement the initial sample of events may contain tracks that would never be able to be fully reconstructed within the FMD, thus lowering the

[1]Correlation between the FMD and the FMT is expected.

measured efficiency. However, it was shown in figure 5.18 that there is a systematic shift indicating an overall underestimation in the momentum measured by the FTD. This will therefore not affect the following studies.

6.1.1 The FMD Track Reconstruction Efficiency

The track reconstruction efficiency of the FMD has been calculated as a function of the momentum measured by the FTD (p_{FTD}) and the polar angle measured by the FTD (θ_{FTD}). The sample of data and Monte Carlo events that were selected passed the following cuts :

- A good quality FTD track is required which is linked to a good quality iron track[2].
- A linked iron track that must have a momentum value within the range $2\,GeV/c < p_{FE} < 100\,GeV/c$.
- The number of the last wire layer that has been used to reconstruct the iron track must be greater than 11.
- The absolute difference between the polar angles measured by the iron and the FTD must be less than 6°.

Further cuts are applied when obtaining the efficiency as either a function of p_{FTD} or θ_{FTD}. Figure 6.1 shows the track reconstruction efficiency of the FMD as a function of (*a*) the polar angle (θ_{FTD}) and (*b*) the track momentum (p_{FTD}). For plot (*a*) the FTD momentum of the track must lie in the range $7\,GeV/c < p_{FTD} < 20\,GeV/c$ and for plot (*b*) the polar angle of the track measured by the FTD must lie in the range $8° < \theta_{FTD} < 16°$. This angular range in θ_{FTD} has been chosen because it is where the efficiency is flat.

A fit to the efficiency as a function of p_{FTD} is shown in figure 6.1 (*b*)[3]. The same functional form has been applied to the data points and to the Monte Carlo.

[2]The track identified by the FTD and iron must have passed the Class 24 track selection.

[3]The fit describes a second degree polynomial for $p_{FTD} < 12\,GeV/c$ and a straight line for $p_{FTD} > 12\,GeV/c$

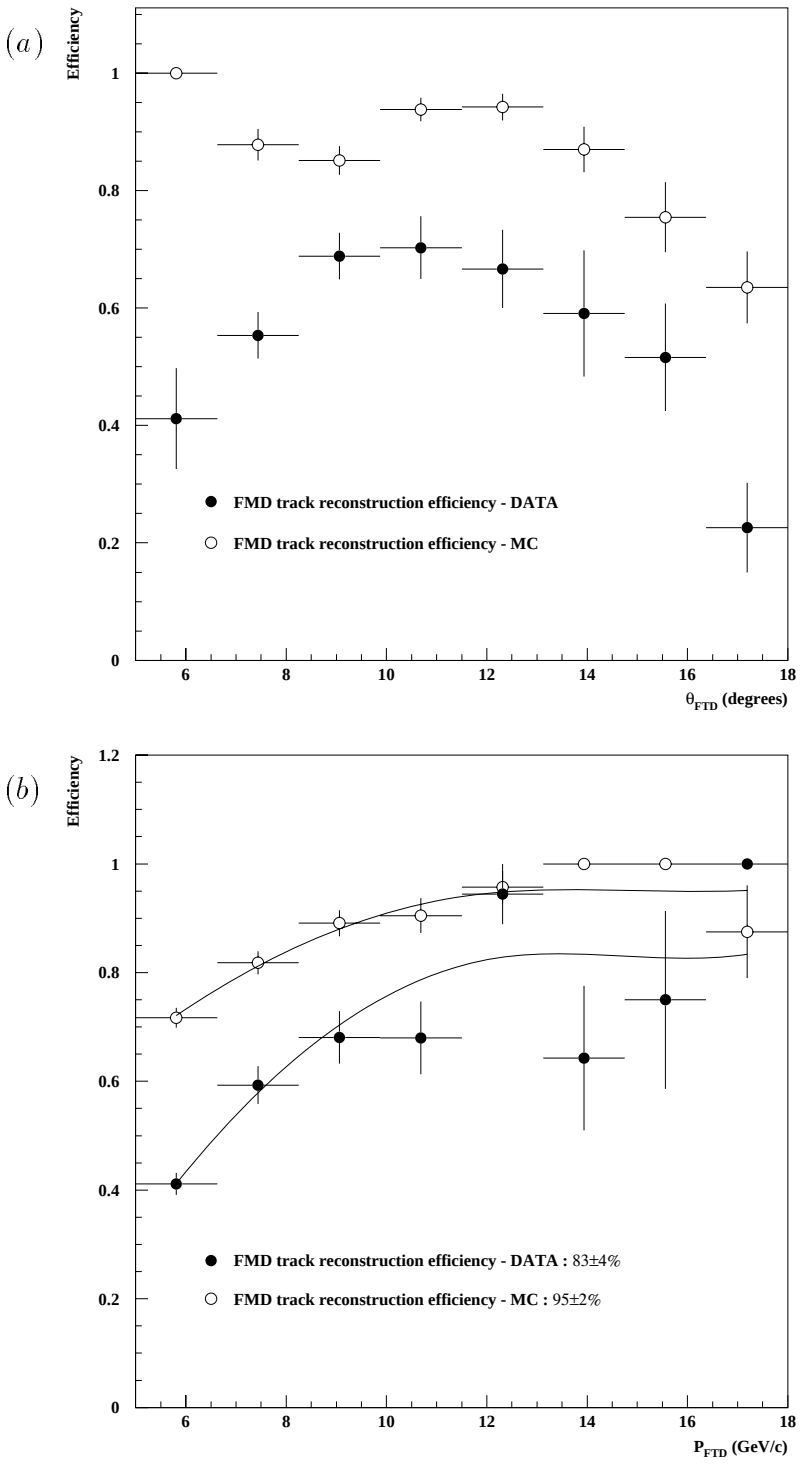

Figure 6.1: *Plot showing the track reconstruction efficiency of the FMD as (a) a function of* θ_{FTD} *and (b) a function of* pFTD. *Plot (b) has been parameterized by the fit shown by the solid line.*

This common parameterization shape seems to agree well with both data and Monte Carlo. The plateau in efficiency which occurs at $p_{FTD} > 12\,GeV/c$ corresponds to a value for the data of $83\pm4\,\%$ and for the Monte Carlo of $95\pm2\,\%$.

Independent studies using Beam Halo muons in the data [58] have given comparable results to the data shown here. Beam Halo data is collected in special runs using triggers which require a coincidence of a forward or backward, inner or outer end-cap reconstructed muon track and hits detected in the veto wall. From this sample of events those with a good forward end-cap iron track are selected. The full FMD reconstruction procedure is then carried out. Only events which have a post-toroid track segment, which when extrapolated, is consistent with the forward end-cap iron track are used. If this criterion is satisfied then the segment finding efficiency can be calculated for pre-toroid segments. It is then assumed that the segment finding efficiency is the same for pre- and post-toroid parts of the FMD. Using events with both a pre- and post-toroid segment, the probability of the segments forming a fully reconstructed track is then calculated and the final overall track reconstruction efficiency approximated to be :

$$\text{Eff} = [\text{segment finding efficiency}]^2 \times [\text{probability of linking pre and post toroid segments}]$$

Since the tracks do not originate from the vertex a momentum measurement cannot be made so the efficiency cannot be expressed as a function of track momentum (or polar angle). The efficiency was measured to be approximately $80\,\% \pm 1.4\,\%$ for full reconstruction of tracks for this method.

The displacement between the Monte Carlo and the data efficiencies is as yet unexplained. One possible explanation in the difference of the efficiency of the FMD is lack of response at the readout ends of the wires known as the 'Maltese Cross Effect'. This can be observed when a hit map is plotted using Class 24 muon tracks for the θ layers of the FMD as is shown in figure 6.2. The effect is only observed in data and indicates that this effect is not modelled by the simulation program.

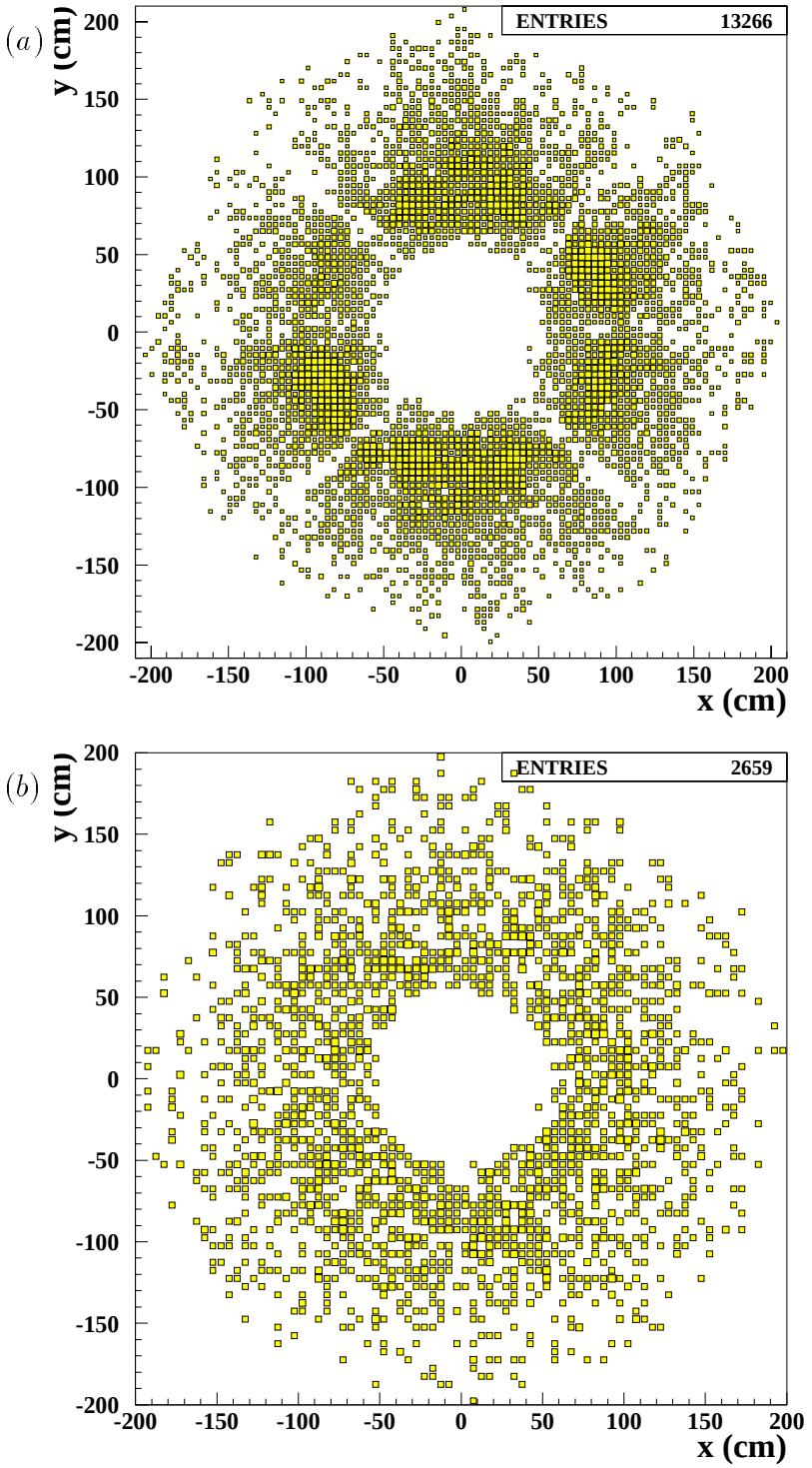

Figure 6.2: *Hit-map distributions of Class 24 muon tracks illustrating the 'Maltese Cross Effect'. Plot (a) shows the distribution as seen in data and plot (b) shows the distribution as seen in Monte Carlo.*

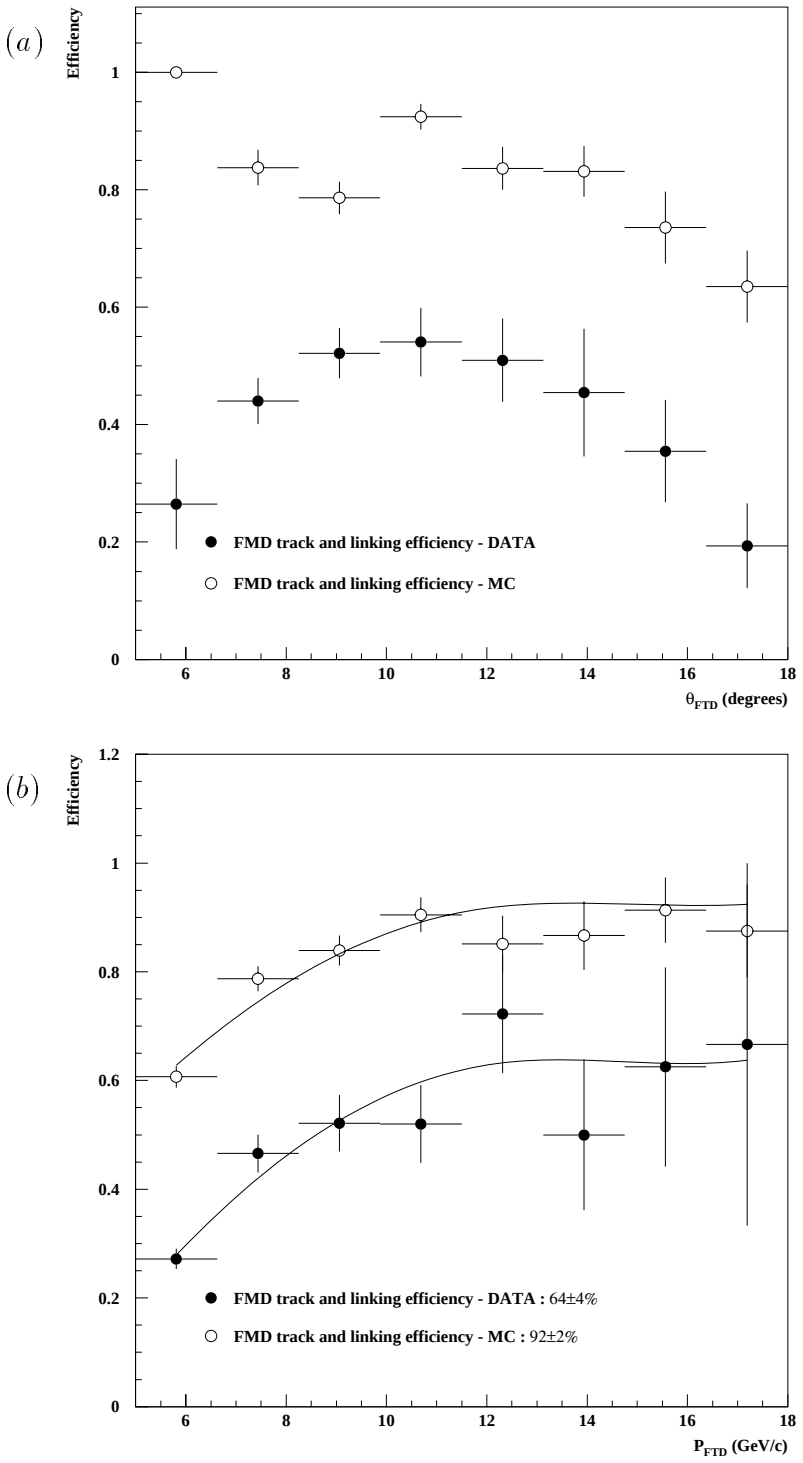

Figure 6.3: *Plot showing the linking and track reconstruction efficiency of the FMD as (a) a function of* θ_{FTD} *and (b) a function of* pFTD.

6.1.2 The FMD Track Linking Efficiency

The efficiency of linking the muons detected by the FMD to the iron or to the FTD is next considered. The event selection described in section 6.1.1 was tightened with the further requirement that the event should contain a reconstructed muon in the FMD. The product efficiency for reconstruction and linking is plotted in figure 6.3 as a function of (a) θ_{FTD} and (b) $\mathrm{p_{FTD}}$ and shows very much the same features as the track reconstruction efficiency plots in figure 6.1.

6.1.3 The Forward Muon Trigger Efficiency and Acceptance

In this section the efficiency and acceptance of the simplest FMT trigger element ($FwdMu\_Val\_Any$) is determined. This trigger element is a component of subtrigger 16 which is used to select events analysed in the elastic J/ψ photoproduction studies of chapter 7. Subtrigger 28 is built from the trigger element $FwdMu\_Val\_Multi$ which is a multi-muon trigger. The efficiency of this trigger for two muon tracks can be calculated using the efficiency determined for single muon trigger element. The efficiency and acceptance of the FMT can be determined by studying a sample of events which contain single muons detected in the FMD. The event selection is that which is described in section 6.1.1. These muons are therefore linked, 'good' quality muons.

Figure 6.4 shows the efficiency of the trigger element, $FwdMu\_Val\_Any$, as a function of (a) the polar angle (θ_{FTD}) and (b) the track momentum ($\mathrm{p_{FTD}}$).

Figure 6.4 plot (b) shows that the FMT efficiency falls off at approximately 10 GeV/c. This can be explained as a result of the correlator chip which introduces a momentum cut on the track bending angle in the magnetic field of the toroid equivalent to $\mathrm{p_{FTD}} > 7\,\mathrm{GeV/c}$. As the tracks undergo multiple scattering in the toroid this angle does not correspond exactly with the momentum of the track. Since the efficiency is being measured as a function of the momentum measured by the FTD the tracker resolution will further broaden the cut off introduced by the correlator chips. By introducing this tight momentum cut the requirement of only

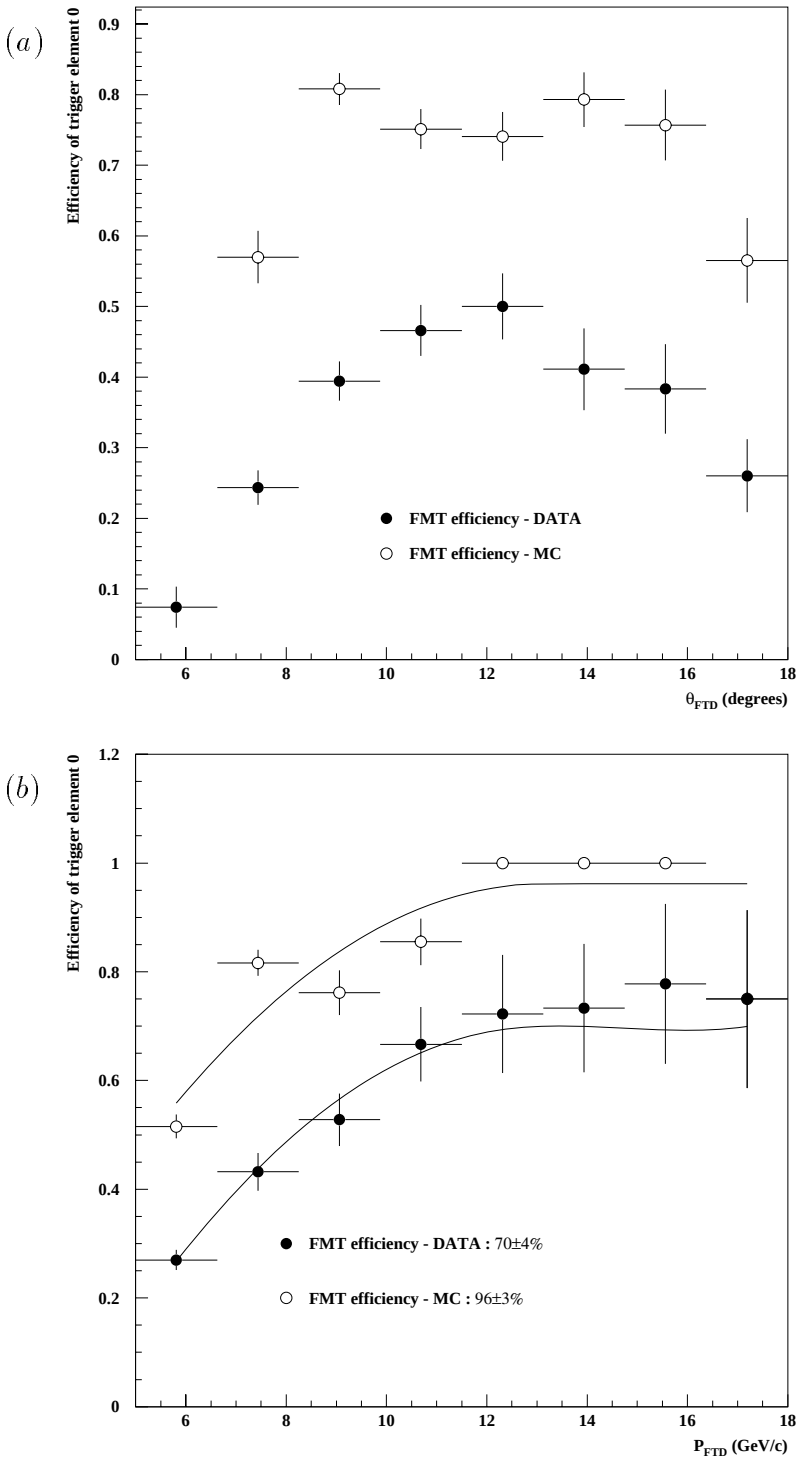

Figure 6.4: *Plot showing the efficiency of the FMT (trigger element 0) as (a) a function of* θ_{FTD} *and (b) a function of* $\mathrm{p_{FTD}}$.

three hits out of a possible four for a track segment reconstruction can be used while still maintaining an acceptable trigger rate.

Figure 6.4 plot (a) shows a loss of lower angle tracks below approximately 8°, which is due to the fact that the inner region of the detector is used to produce a veto for diffractive physics.

Considering only events which are found in the region of good acceptance, defined by $7\,\mathrm{GeV/c} < \mathrm{p_{FTD}} < 20\,\mathrm{GeV/c}$ and $8° < \theta < 16°$ the efficiency of the trigger element $FwdMu\_Val\_Any$, is calculated to be $70\pm4\,\%$ from the data and $96\pm3\,\%$ from the Monte Carlo sample. This discrepancy is partially a result of the single hit finding inefficiencies of the DM, however, it was found that for 1995 data an incorrect timing parameter was used when simulating the FMT [59]. A further study is required to fully understand these features with respect to the efficiency of the trigger.

6.2 The Forward Iron End-Cap Track Reconstruction and Trigger Efficiency

Provided they have sufficient energy ($> 2\,\mathrm{GeV}$) muons travelling in the forward direction can traverse the forward iron end-cap. If a track can be reconstructed by the iron and linked to a FTD track then the particle may be identified as a muon[4]. This detector therefore provides muon track identification that supplements the FMD and FMT. It is essential that the track reconstruction efficiency and the trigger efficiency of the instrumented iron is determined for data and Monte Carlo if this detector is used when calculating the acceptance for the given decay.

A sample of data events triggered independently of all muon triggers were collected. The data and Monte Carlo events were selected to pass the event selection described by the following cuts :

- A good quality FTD track is required that passes the Class 24 cuts which is linked to a good quality FMD track.

[4]Alternatively the FTD track maybe linked to a FMD track segment and thus identified as a muon.

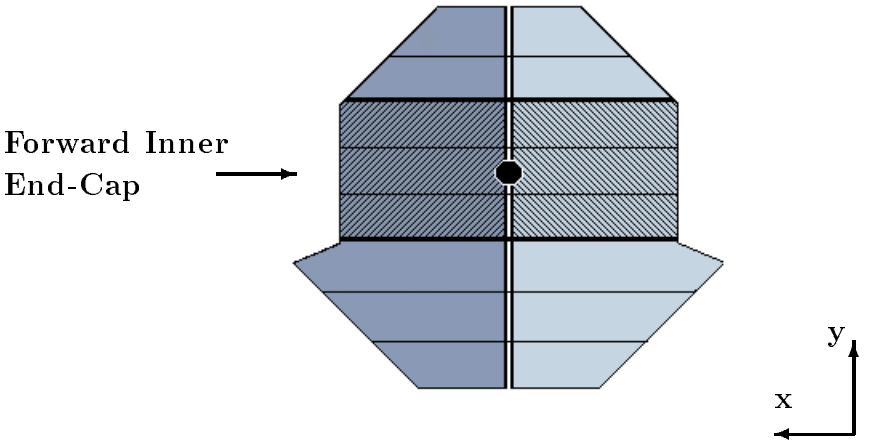

Figure 6.5: *The design structure of a the forward iron end-cap illustrating how it is divided into distinct modules in x and y. The the inner end-cap has been shaded The beam pipe position (approximately (0,0) in the xy plane) is shown by the circle.*

- The y coordinate associated with the tracks must fall in the range -120 cm $< y <$ 120 cm.
- The momentum measured by the FTD must be greater than 4 GeV/c.
- The run number must be above 120000. This removes runs where the instrumented iron was not fully functional.

The event sample described above was then used to calculate the track reconstruction efficiency and the trigger efficiency of the forward iron inner end-cap. The track reconstruction efficiency of the forward iron end-cap is shown in figure 6.6 as a function of (a) and (b) the y coordinate in the iron module for $x < 0$ and $x > 0$ respectively, (c) the momentum and (d) the polar angle of the track. The efficiency was measured to be 86$\pm$1 % for data and 87$\pm$1 % for Monte Carlo [59]. The bins used in figure 6.6 (a) and (b) match the six modules which make up the forward iron inner end-cap. The modular structure of the forward iron end-cap in the xy plane can be seen in figure 6.5 where the six modules of the inner end-cap have been cross-hatched. The hole for the beam pipe can be seen at the center of the end-cap

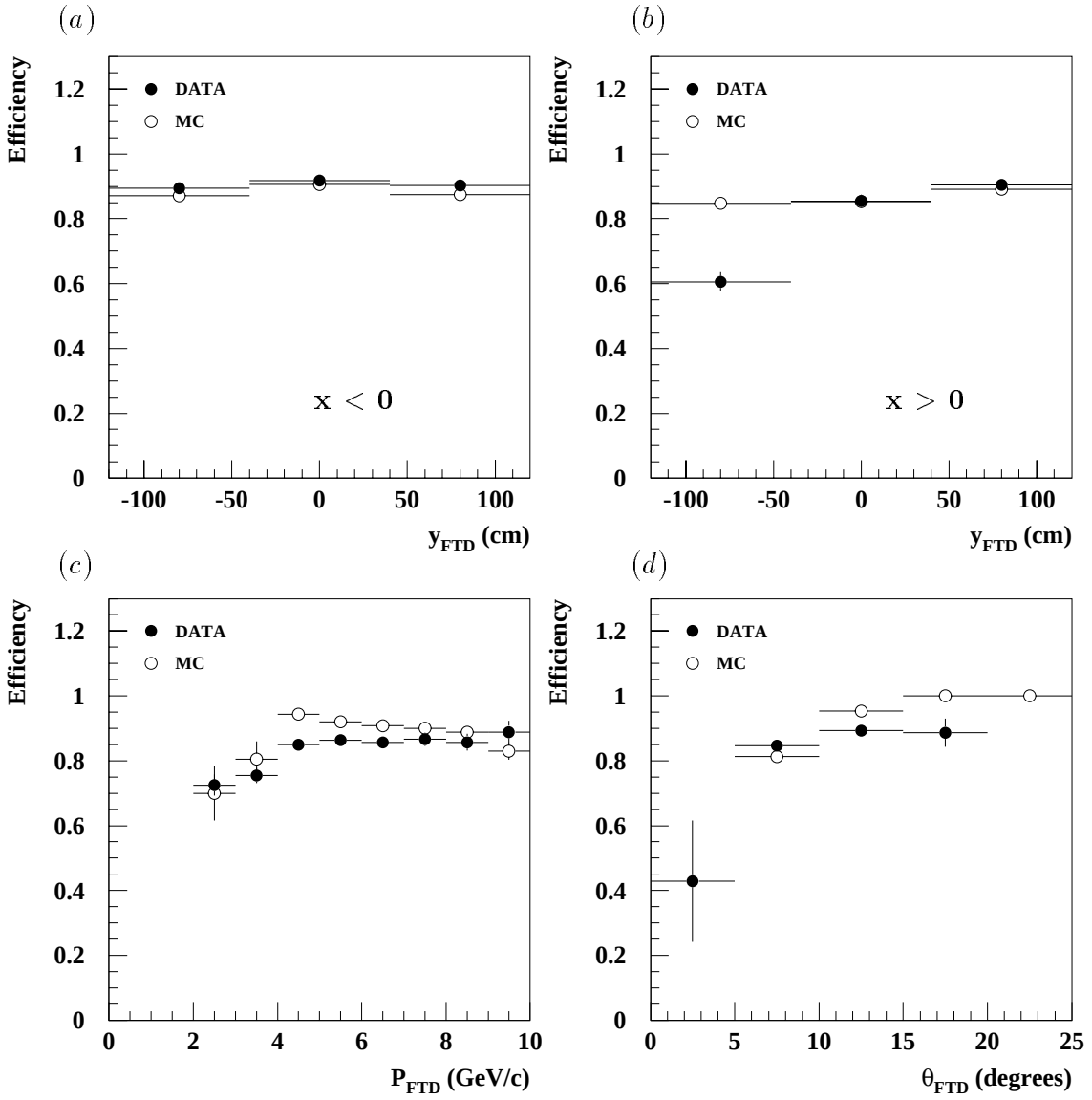

Figure 6.6: *Figure showing the efficiency of the track reconstruction of the forward iron end-cap. Plots (a) and (b) show the efficiency as a function of y for $x < 0$ and $x > 0$ respectively. Plots (c) and (d) show the efficiency as a function of the momentum measured in the FTD and theta measured in the FTD. The closed points represent the data and the open points represent the Monte Carlo.*

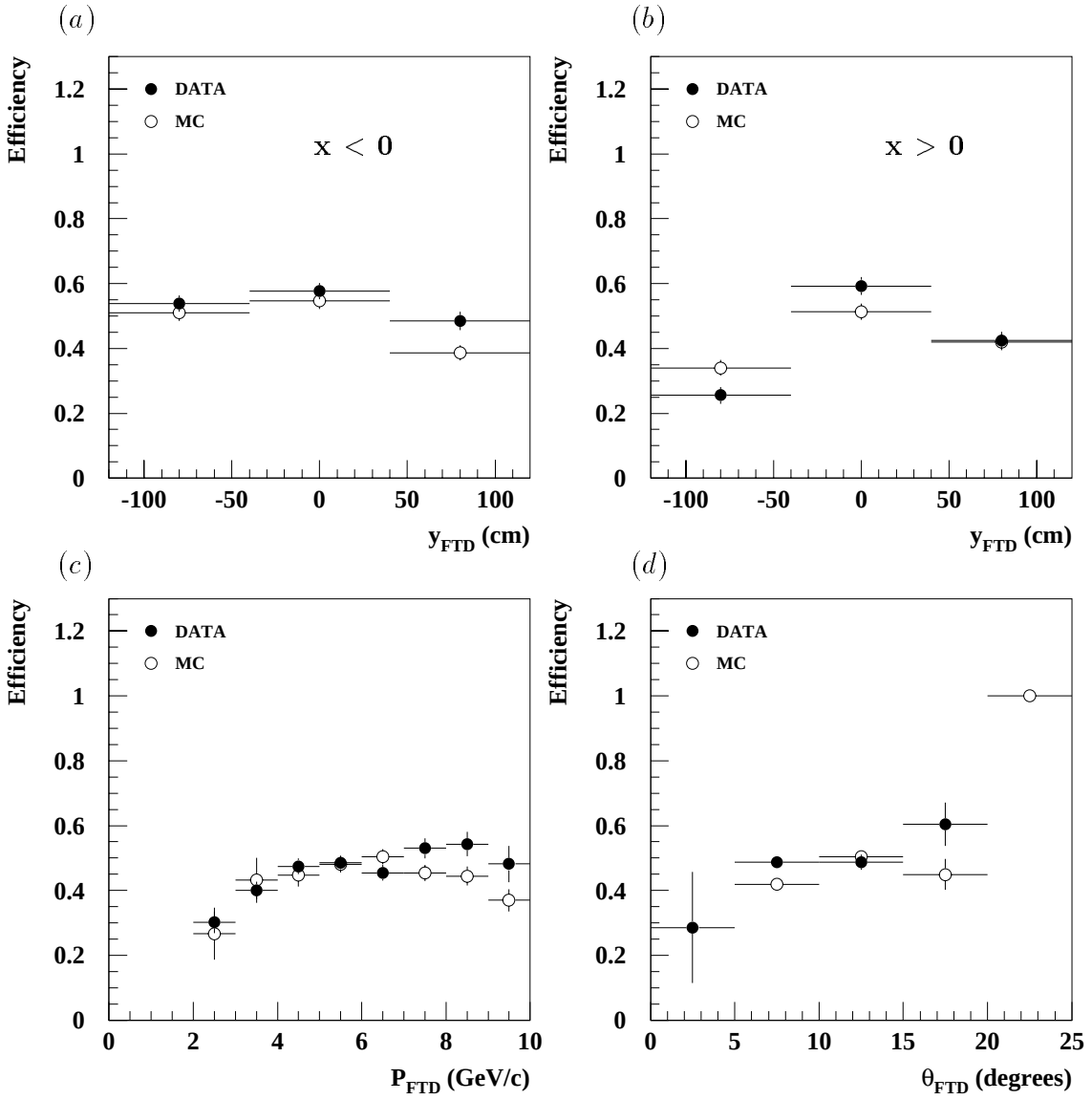

Figure 6.7: *Figure showing the efficiency of the forward iron end-cap trigger element Mu_FIEC. Plots (a) and (b) show the efficiency as a function of y for $x < 0$ and $x > 0$ respectively. Plots (c) and (d) show the efficiency as a function of the momentum measured in the FTD and theta measured in the FTD. The closed points represent the data and the open points represent the Monte Carlo.*

which is located at approximately (0,0) in the xy plane.

The efficiency of the forward iron inner end-cap trigger element (Mu_FIEC) is shown in figure 6.7 as a function of (a) and (b) the y coordinate in the iron module for $x < 0$ and $x > 0$ respectively, (c) the momentum and (d) the polar angle of the track. The efficiency was measured to be 49$\pm$1 % for data and 45$\pm$1 % for Monte Carlo [59]. The forward iron outer end-cap trigger element (Mu_FOEC) has not been studied as the subtriggers selected for the analysis described in chapter 7 do not contain this trigger element (the selected subtriggers are listed in tables 7.1 and 7.2).

The requirement that the FTD track is linked to a FMD track forces the track to have a momentum of at least 4 GeV/c. Figures 6.6 and 6.7, plots (c), show the efficiency as a function of momentum. The efficiency is seen to fall at momentum values below 4 GeV/c, however, a non-zero efficiency is observed down to approximately $p_{FTD} \sim 3$ GeV/c. These tracks must be falsely linked tracks in which the FTD track have been incorrectly linked to the FMD track and should in fact have an efficiency of zero.

6.3 The Inner Track Reconstruction and Triggering Efficiencies

As described in chapter 4, the term inner tracks refers to tracks which have been detected and reconstructed by the FTD or the CTD (or a combination of both detectors). The subtriggers on which the analysis in chapter 7 is based also include components from the inner region namely the z-vertex, central track and topological trigger elements. The efficiencies of these trigger elements are determined in the following section following a brief description of the CTD and FTD track reconstruction efficiencies. The event selection made for the study of the quasi-elastic photoproduction of the J/ψ meson in chapter 7 includes the following two event topologies :

(1) One identified muon must be found in the angular range $\theta < 20°$ and the other in the range $\theta > 20°$;

(2) Both identified muons must lie in the angular range $\theta < 20°$.

The same event topology is used to determine the inner track trigger efficiencies, but in order to maximise statistics, no requirement was made that the pair of particles are identified as muons.

6.3.1 The FTD and CTD Track Reconstruction Efficiencies

In order to determine the FTD track reconstruction efficiency a good quality CTD track was chosen which was linked to a good forward iron end-cap or FMD track. All tracks must pass the Class 24 selection that was described in section 4.1 with the proviso that the classification was not dependent on the detection of the FTD tracks. Other requirements made on the CTD track were as follows :

- $\theta_{\mathrm{CTD}} < 20°$;
- The z coordinate of the CTD track vertex must have $|z|$ <20 cm ;
- $\mathrm{p_{CTD}} > 2\,\mathrm{GeV}$.

The FTD reconstruction efficiency was determined by finding a reconstructed FTD track which had theta and phi values compatible with the CTD track. To reduce the track multiplicity of the events the number of FTD hits (radial + planar) was restricted to less than 2000. The track reconstruction efficiency from this study was found to be 72±1 % for data and 77±1 % for Monte Carlo [59].

The CTD track reconstruction has been studied in detail [60] and is seen to rise sharply as a function of the transverse track momentum (p_T). It rises from approximately 0 % at $p_T = 80\,\mathrm{MeV}$ to approximately 97 % at $p_T > 120\,\mathrm{MeV}$. The tracks that are studied in the analysis described here have a much higher momenta lying in the plateau region of 97±3 % acceptance.

6.3.2 The Z-Vertex Trigger Elements

This trigger uses tracks found and reconstructed in the proportional chambers interleaved in the FTD and the CTD. All tracks are extrapolated back to the beam axis and then the z position of each track where it crosses the beam axis is entered in a 16 bin histogram, each bin representing approximately 5.4 cm in z. A z-vertex is then determined from the z distribution. The events under consideration are events with only two tracks so that the determination of a z-vertex is difficult. The trigger elements $zVtx\_Cls$ and $zVtx\_small$ of interest are both low multiplicity trigger elements. These trigger elements are components of subtriggers 17 and 54 detailed in tables 7.1 and 7.2. In each case a sample of events was collected which were triggered independently of the z-vertex trigger and are typically triggered by DIS triggers which do not require tracks or a vertex.

The *zVtx_small* trigger element

This trigger element forms a part of subtriggers 14 and 17 (see tables 7.1, 7.2) and it demands low multiplicity in the z-vertex histogram. . Figure 6.8 shows the efficiency of this z-vertex trigger element as a function of momentum and polar angle. For the one forward going muon sample the momentum and angle plotted is that of the forward going muon and for the two forward muons sample the parameters are the averaged value of the momentum and angle of the two tracks.

The results from the study gave an efficiency value for the trigger element $zVtx\_small$ for the one forward going muon sample of 74.8±2.5% for data and 75.0±1% for Monte Carlo while for the two forward going muons sample of 32.2±3% for the data and 31.0±1% for the Monte Carlo.In both cases these are the efficiencies for momenta $p > 0.5\,\mathrm{GeV/c}$ only.

The *zVtx_Cls* trigger element

This is a low track multiplicity trigger element that requires all histogram entries to be within four neighbouring bins. As shown in table 7.1, subtrigger 54 contains the trigger element $zVtx\_Cls$, and hence this trigger element is only relevant where the

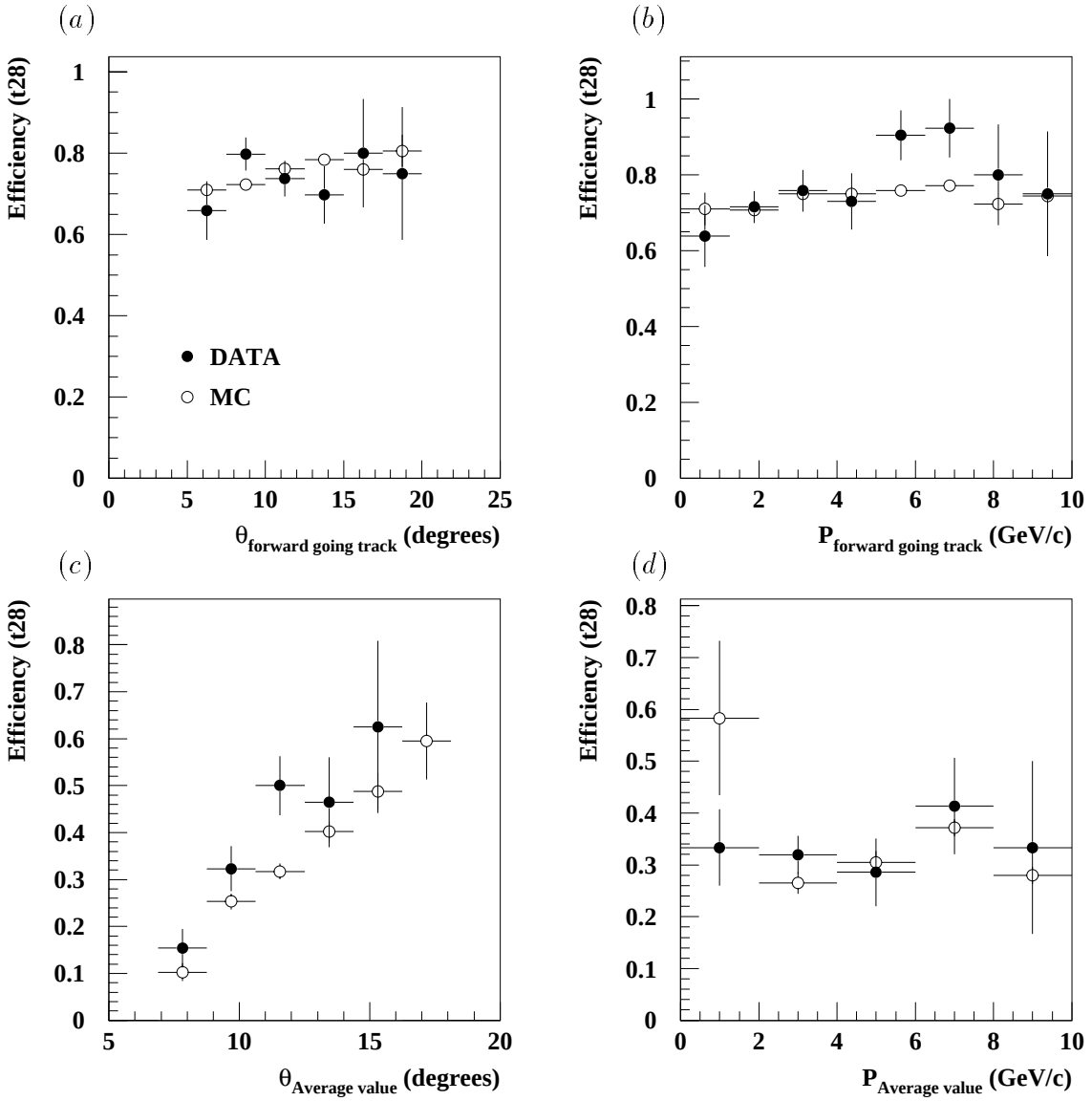

Figure 6.8: *Figure showing the efficiency of the z-vertex trigger element zVtx_small for each event sample. Plots (a) and (b) show the efficiency as a function of the momentum and theta of the forward going track. Plots (c) and (d) show the efficiency as a function of the average value of the measured momentum and theta of the two forward going tracks. The closed points represent the data and the open points represent the Monte Carlo.*

one forward going muon sample is concerned. Figure 6.9 shows the efficiency of this z-vertex trigger element as a function of momentum and polar angle. The efficiency is plotted as a function of the momentum and polar angle of the forward going track ($\theta < 20°$). The results from the study gave an efficiency value of 82.7±2.2% for data and 75.9±1.0% for Monte Carlo for the trigger element $zVtx\_small$ in the region of $p > 0.5\,\mathrm{GeV/c}$.

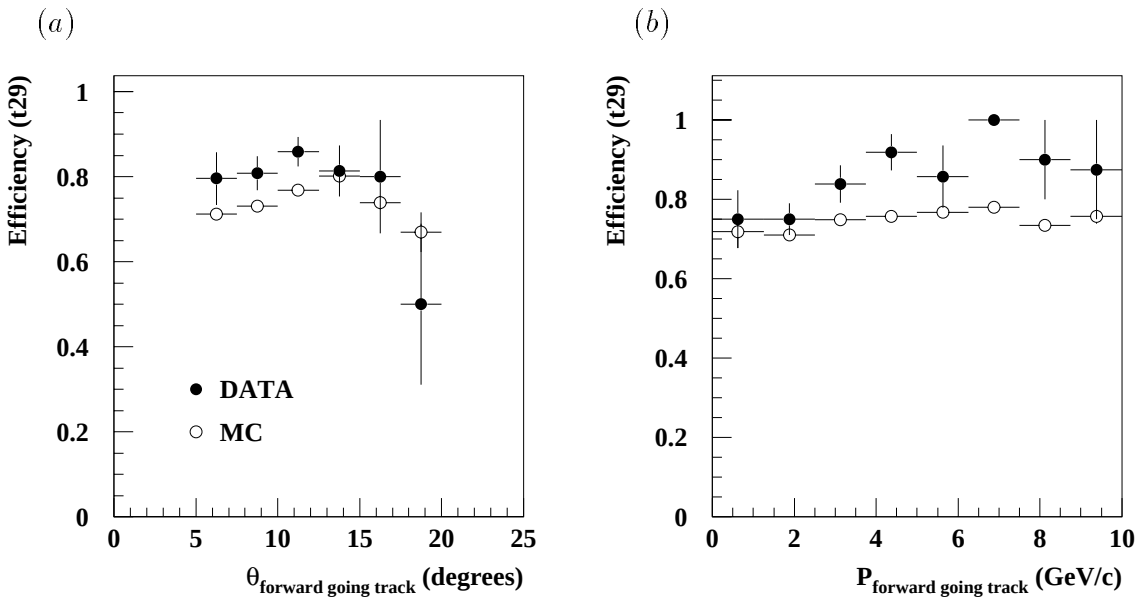

Figure 6.9: *Figure showing the efficiency of the z-vertex trigger element zVtx_Cls as a function of (a) the momentum, and (b) the polar angle for the forward going track. The closed points are the data and the open points are the Monte Carlo.*

6.3.3 Central Track Trigger Elements

Subtrigger 54 used for the sample of one forward going muons, contains the central track trigger element $DCRPh\_TNeg$. The $DCRPh$ trigger looks for tracks in the CJC which reach at least the third layer of CJC 2 (this imposes a cut on the acceptance in theta). The trigger efficiency for tracks with a $DCA > 2\,\mathrm{cm}$ is below 40%, while the trigger efficiency for tracks with $DCA < 2\,\mathrm{cm}$ is above 90% [61]; which suppresses the triggering of background events.

The trigger element $DCRPh\_TNeg$ requires at least one negative mask above 450 MeV which is the minimum p_T for accepting a track. A mask is the internal representation of a track in the trigger and one track on average fires 1.5 masks.

A study was carried out to compare the efficiency of the central track trigger elements of the data to Monte Carlo [62]. The events were collected independently of the $DCRPh$ trigger and had been triggered mainly by DIS subtriggers which do not require tracks or a vertex. The results from the study gave an efficiency value of 78.7±1.1 % for the data and 80.2±0.5 % for the Monte Carlo for the trigger element $DCRPh\_TNeg$ in the region of $p > 0.5\,\mathrm{GeV/c}$ and $50° < \theta < 150°$.

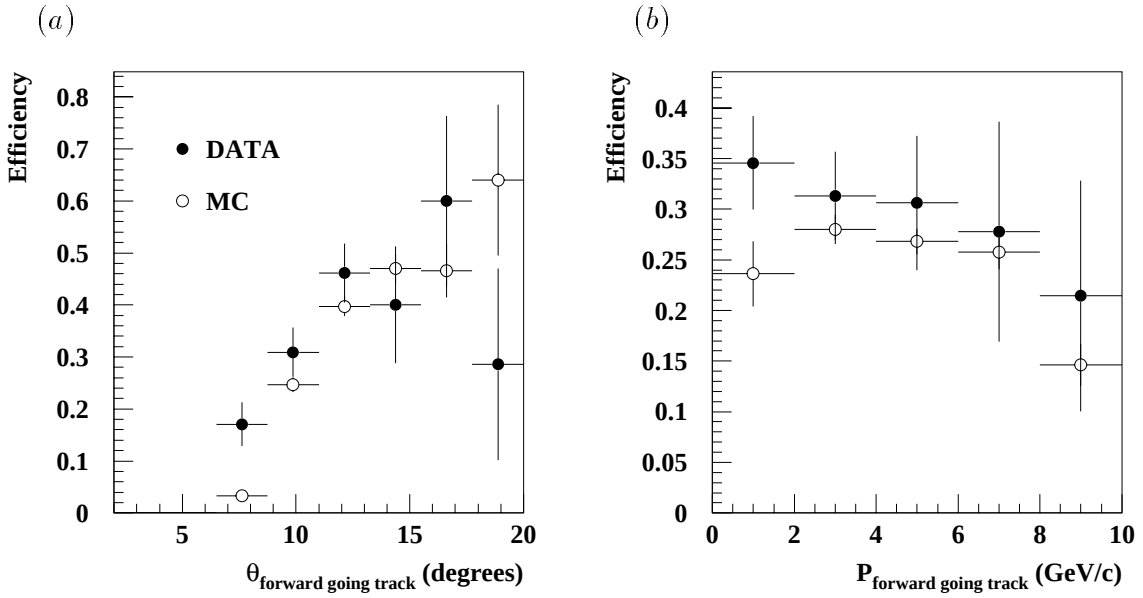

Figure 6.10: *Figure showing the efficiency of the topological trigger element Topo_BR as a function of (a) the momentum, and (b) the polar angle for the forward going track. The closed points represent the data and the open points represent the Monte Carlo.*

6.3.4 The Topological Trigger Element

This trigger element referred to as $Topo\_BR$ requires two tracks 'back-to-back' in the $r\phi$ plane. The tracks are detected by the central proportional chambers, CIP and

COP. This back-to-back event topology of the events triggered by the topological trigger can only be satisfied by the events containing one forward going muon. The efficiency of this trigger has been studied using a sample of events selected independently of the MWPC triggers and which contained a single forward going track ($\theta < 20°$). The efficiency was found to be $29.9 \pm 3.3\%$ for data and $27.0 \pm 1.0\,\%$ for Monte Carlo.

6.3.5 Summary of the Inner-Track Trigger Efficiencies

The results obtained from these inner-track trigger studies are listed in table 6.1. There are some discrepancies observed between the efficiencies measured for data and Monte Carlo. The difference between the efficiencies is taken as a measure of the systematic error and is discussed further in section 7.5.

Trigger Element	Efficiency (%) - 1fwd		Efficiency (%) - 2fwd	
	Data	Monte Carlo	Data	Monte Carlo
$zVtx\_small$	74.8 ± 2.5	75.0 ± 1.0	32.2 ± 3.0	31.0 ± 1.0
$zVtx\_Cls$	82.7 ± 2.2	75.9 ± 1.0	-	-
$DCRPh\_TNeg$	78.7 ± 1.1	80.2 ± 0.5	-	-
$Topo\_BR$	29.9 ± 3.3	27.0 ± 1.0	-	-

Table 6.1: *Inner track trigger element efficiencies.*

Chapter 7

Elastic J/ψ Photoproduction at Low $W_{\gamma p}$

Studies of elastic J/ψ photoproduction from H1 and ZEUS have been published [63, 64] for the $W_{\gamma p}$ range 30 GeV $< W_{\gamma p} <$ 150 GeV. The following chapter presents results which extend the $W_{\gamma p}$ range down to 20 GeV. This is only made possible through utilising the forward detectors which have been discussed in detail in previous chapters. The published results indicate a steeper rise in the cross-section with $W_{\gamma p}$ (this can be seen in figure 1.10) than the Donnachie and Landshoff soft Pomeron model can accommodate. The extension of the $W_{\gamma p}$ range provided by the data presented in this chapter provides cross-section points between the energy range from the previously published H1 results at 30 GeV$< W_{\gamma p} <$150 GeV and the fixed target experiment results at 10 GeV$< W_{\gamma p} <$30 GeV. Thus an attempt to extract the cross-section dependence on $W_{\gamma p}$ can be made over the whole energy range.

The cross-section measurement for elastic J/ψ production has been determined for data taken at H1 during the 1995 run period. This data corresponds to a total integrated luminosity of $5.09 \pm 0.06\,\mathrm{pb}^{-1}$. The following reaction has been studied :

$$\gamma\ p \longrightarrow J/\psi\ p \qquad J/\psi \longrightarrow \mu^+\ \mu^-$$

The $J/\psi \rightarrow e^+e^-$ decay mode cannot be studied in this region of acceptance because the trigger and detector acceptance for electrons is found to be very low in the forward direction. From preliminary studies using a 1995 data sample the e^+e^- decay channel was found to be very statistically limited.

7.1 Preliminary Elastic Event Sample

A preliminary elastic event sample for the dimuon decay channel of photoproduced elastic J/ψ's was selected using the following event criteria :

- There must only be two reconstructed tracks per event. These tracks are identified as muons using either the LAr, the FMD or the instrumented iron. The muons linked to tracks with $\theta < 20°$ are required to be identified by either the FMD or the instrumented iron only. The tracks must pass the 'good' track selection as described in section 4.2.

- There must be no calorimeter cluster detected above the threshold energy of 0.5 GeV in the LAr calorimeter within $\eta \leq 2.5$[1]. Energy deposits due to the reconstructed muon pair are first removed before applying this cut. The threshold energy has been selected to allow for noise within the calorimeter but ensures that events which contain particles other than the muon pair are rejected.

- A cut of $E_e < 8$ GeV is applied to the most energetic electron found in the event. This imposes a cut of $Q^2 < 1.2\,\mathrm{GeV}^2$ and defines an upper limit to the Q^2 range for the measured cross-section. This is also used when calculating the photon flux factor ($\Phi_{\gamma/e}$) defined in chapter 1.

- The High Voltage (H.V.) of all the H1 sub-detectors is required to be on.

- The z co-ordinate of the reconstructed event vertex must be within ± 35 cm of the nominal event vertex (0,0).

[1] Where η is the pseudo-rapidity defined as η = -ln tan$\frac{\theta}{2}$.

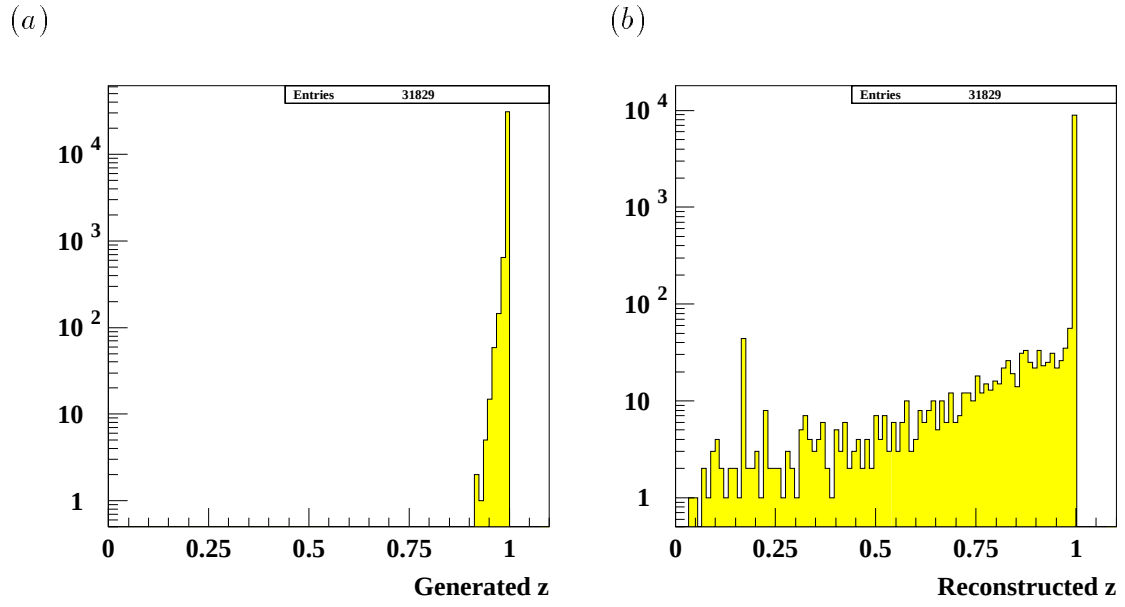

Figure 7.1: *Plots showing the (a) generated values and (b) the reconstructed values for z for elastic J/ψ events as described by the DIFFVM generator (section 7.2.1).*

As discussed in section 1.5.5, events which have $z > 0.95$ are termed quasi-elastic. These events can be crudely separated into elastic events by applying the following cuts which are designed to detect activity in the forward direction which can be associated with the proton breaking up :

- There must be no calorimeter cluster detected above the threshold energy of 0.5 GeV by the LAr within $\eta \leq 6.0$.
- The total number of pairs[2] detected by the pre-toroid layers of the Forward Muon Detector (FMD) should be 0 or 1.
- There should be no hits in the Proton Remnant Tagger.

Figure 7.1 shows: (a), the generated z values and (b), the reconstructed z values of elastic events which are typically $z > 0.95$. The spread in the reconstructed z values is not seen at the generator level. The variable z is not used to make a direct cut on the elasticity of the event for this reason. However, the demand that there are only two tracks found in the event and no other activity detected imposes a limit of $z > 0.95$.

[2]Pairs associated with muon tracks were removed before applying this cut.

Subtrigger	Composite Trigger Elements
st16	Mu_FIEC && $FwdMu\_Val\_Any$
st17	Mu_FIEC && $zVtx\_small$
st54	$zVtx\_Cls$ && $DCRPh\_TNeg$ && $Topo\_BR$

Table 7.1: *Subtriggers used for one forward going muon sample.*

Subtrigger	Composite Trigger Elements
st16	Mu_FIEC && $FwdMu\_Val\_Any$
st17	Mu_FIEC && $zVtx\_small$
st28	$FwdMu\_Val\_Multi$

Table 7.2: *Subtriggers used for two forward going muons sample.*

7.1.1 Event Types.

The elastic event sample previously described was then split into two event types:

One Forward Going Muon

This sample covers the range 25 GeV< $W_{\gamma p}$ <40 GeV and was selected as follows:

- One identified muon must be found in the angular range $\theta < 20°$ and other in the range $\theta > 20°$.
- One or more of the subtriggers 16, 17, or 54 (see table 7.1) actively triggered the events.

Two Forward Going Muons

This sample covers the range 20 GeV < $W_{\gamma p}$ < 27 GeV and was selected as follows:

- Both identified muons must lie in the angular range $\theta < 20°$.
- One or more of the subtriggers 16, 17, or 28 (see table 7.2) actively triggered the events.

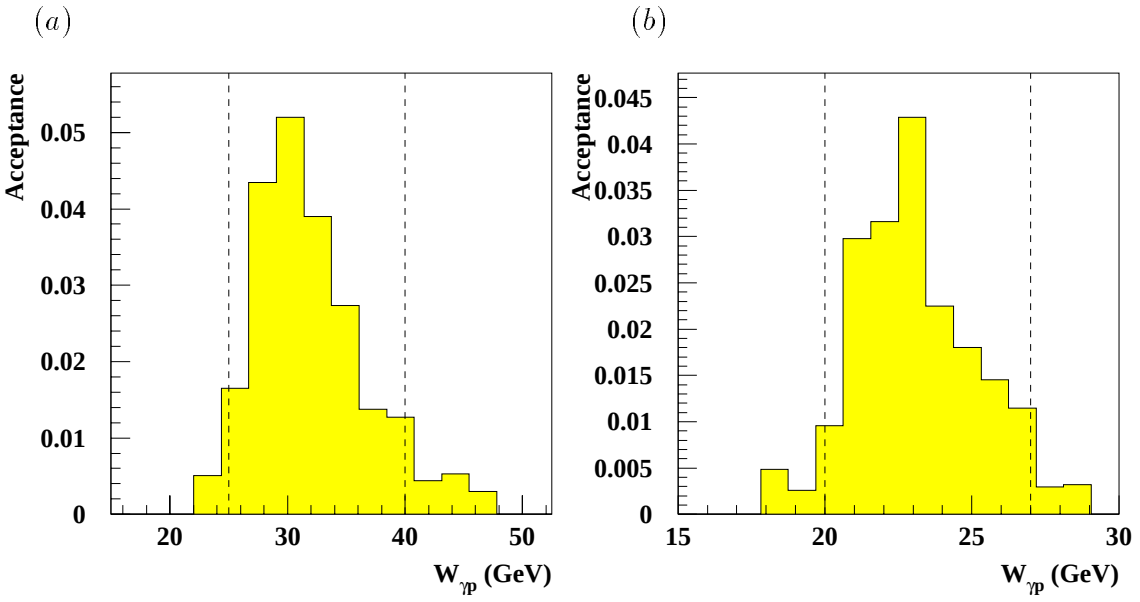

Figure 7.2: *The acceptance as a function of $W_{\gamma p}$ for (a) the one forward going muon event sample and (b) the two forward going muons event sample. The dashed lines give the boundaries of the chosen $W_{\gamma p}$ ranges for each sample.*

The appropriate ranges of $W_{\gamma p}$ for the analysis were chosen after examining the acceptance as a function of $W_{\gamma p}$ obtained using the elastic DIFFVM Monte Carlo [65] (described in section 7.2.1). Figure 7.2 shows the acceptance for (a) the one forward going muon event sample and (b) the two forward going muons event sample. The selected regions have been indicated by dashed lines at 25 GeV$<$ $W_{\gamma p}$ $<$40 GeV and 20 GeV$<$ $W_{\gamma p}$ $<$27 GeV for the one and two forward going muons samples respectively.

Example events which can typically be found in these two samples are displayed in figure 7.3. The preliminary elastic event sample has been separated into these two groups because the precision in the determination of the dimuon effective mass is very different for the two cases. Figure 5.32 showed that the invariant mass distribution reconstructed from two forward tracks has a broader peak than the invariant mass distribution reconstructed from one forward and one central muon. The separation of the non-resonant background contributions (discussed in section 7.4.1) is

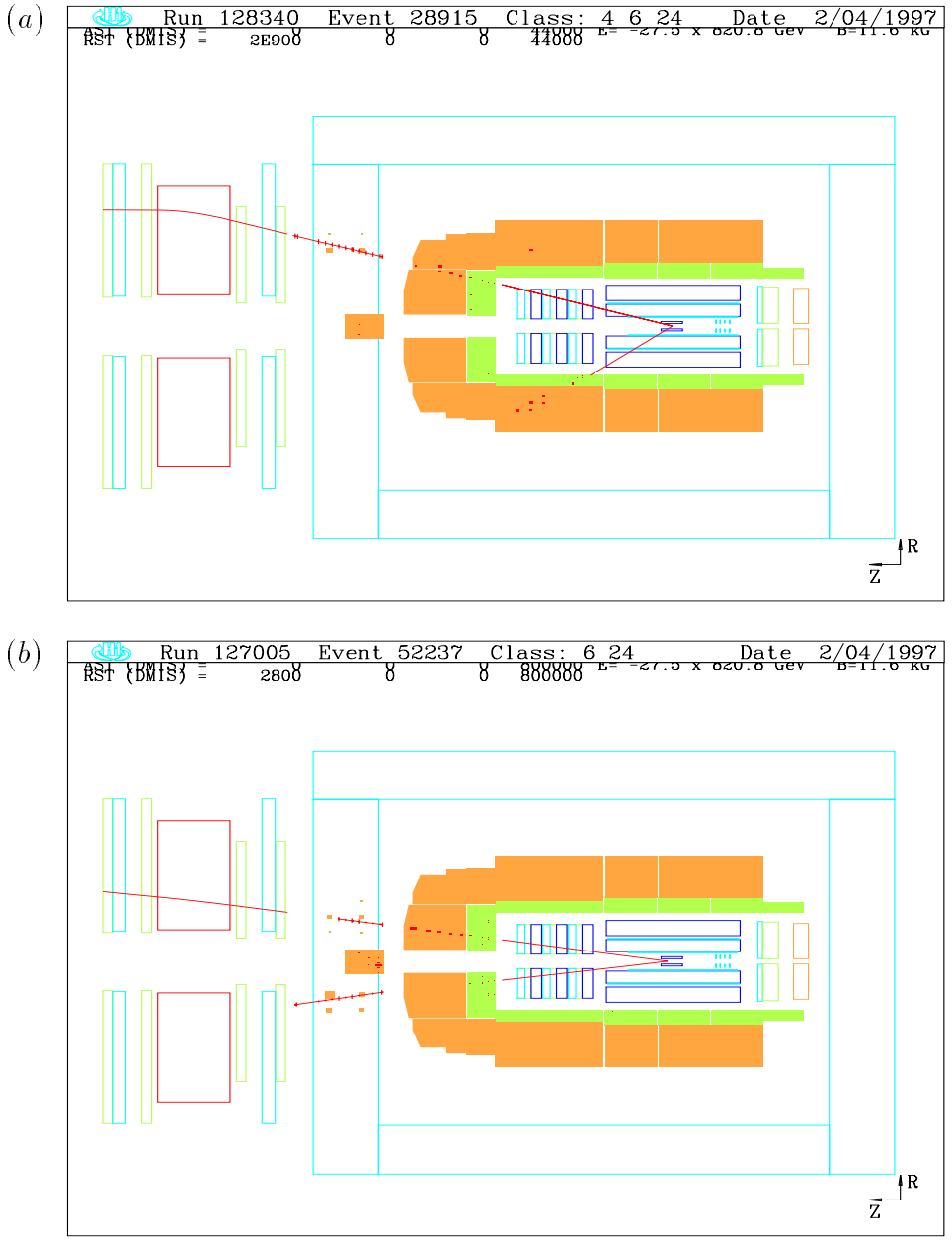

Figure 7.3: *Example events which are typical of the elastic event categories : (a) the one forward going muon and (b) the two forward going muons. The FMD has reconstructed a track for both events.*

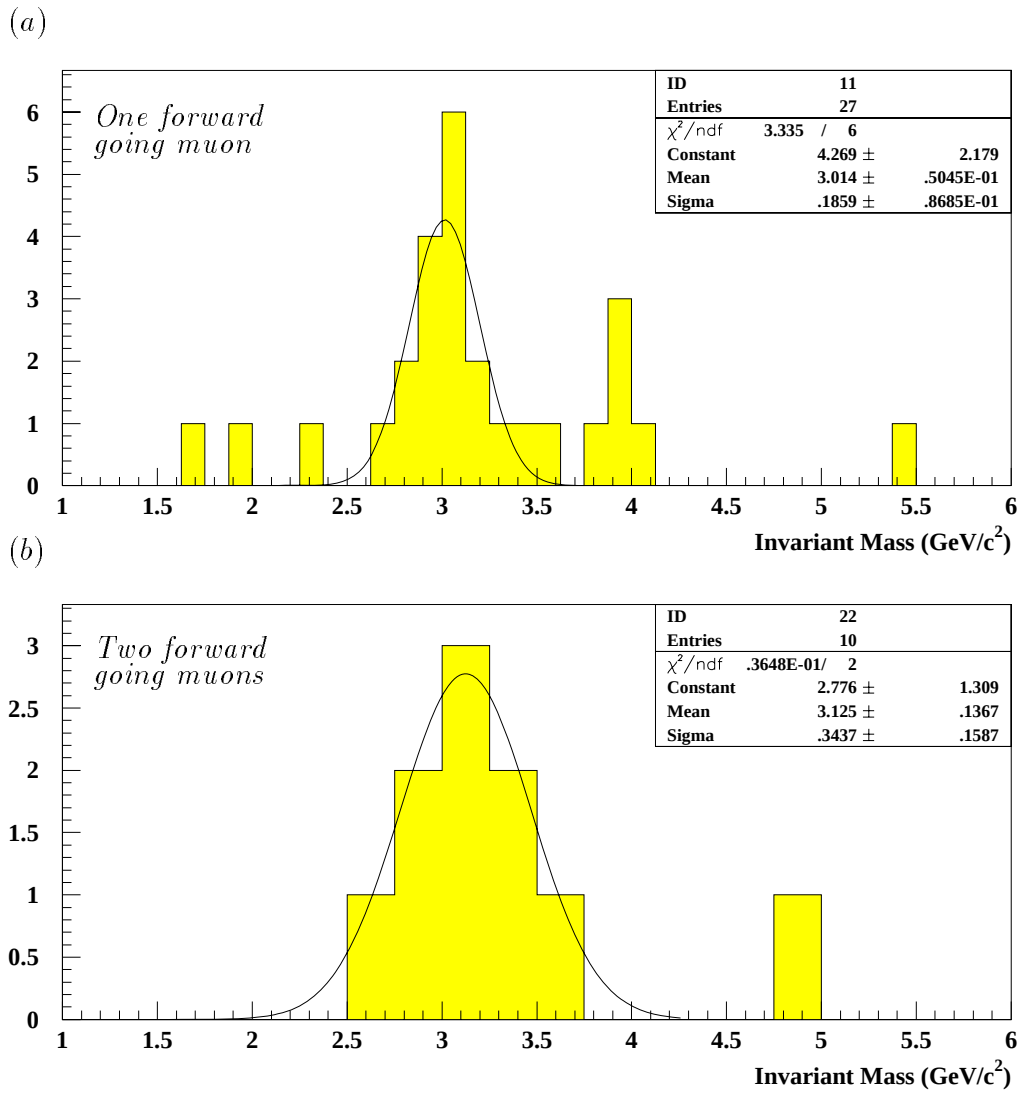

Figure 7.4: *The reconstructed invariant mass distributions for the $\mu^+\mu^-$ pairs passing the event selection described in section 7.1. Plot (a) shows the resulting mass distribution for the one forward going muon event sample and plot (b) shows the mass distribution for the two forward going muons event sample.*

difficult if the samples are combined because the J/ψ signal would then consist of two peaks with very different widths.

The invariant masses reconstructed for both event samples are displayed in figure 7.4. The momentum reconstructed by the FMD is used instead of the momentum measured by the FTD for events containing a FMD reconstructed track. The resonances have been fitted with a Gaussian shape for the peak. The mean and width of the fit is seen to agree well with the predicted values as quoted by [57]. Figure 7.4 (a) shows in addition to the J/ψ signal a second signal at approximately 3.9 GeV/c^2. This could be attributed to $\psi' \to \mu^+\mu^-$ decays[3]. However it is displaced by approximately 200 MeV/c^2 so it is more likely to be a statistical fluctuation.

7.2 Monte Carlo Generators

7.2.1 The DIFFVM Generator

The Monte Carlo generator that has been used through out this analysis is known as DIFFVM [65]. This generates proton dissociation ($\gamma p \to J/\psi X$) or elastic ($\gamma p \to J/\psi p$) diffractive events according to the Vector Dominance Model which was previously described in section 1.5.3. Figure 7.5 shows the Feynman diagram for the type of process that is generated in the case of an elastic event where the proton has remained intact. The generator assumes that the cross-sectional dependence on the center of mass energy, $W_{\gamma p}$, is that which was expressed by equation 1.29 and which is simply :

$$\sigma(\gamma p \to Vp) \propto W_{\gamma p}^{4\lambda}. \tag{7.1}$$

The parameter λ is set at the value of 0.225 and since $\alpha_{I\!P}(0) = 1 + \lambda$ this will correspond to a Regge trajectory with an intercept $\alpha_{I\!P}(0) \approx 1.225$. This is typical of the hard pomeron as described by the 'Ryskin Model' [25, 26]. The cross section is also dependent on t, the square of the four momentum transfer carried by the colourless object. This dependence has been previously given by equation 1.24 as

[3]The accepted ψ' mass, as quoted by [57], is 3.685 GeV/c^2

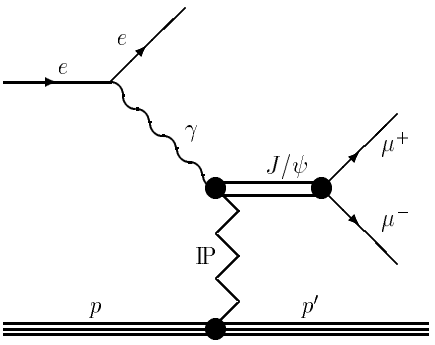

Figure 7.5: *Schematic diagram showing the VDM process responsible for the production of J/ψ via a colourless object called the pomeron (*$\mathbb{P}$*).*

simply :

$$\frac{d\sigma}{dt} \propto e^{b't}. \tag{7.2}$$

The b' parameter is given by the following expression:

$$b' = 2b_A + 2b_B + 2\alpha'_{\mathbb{P}} \ln\left(\frac{\mathrm{W}^2_{\gamma\mathrm{p}}}{\mathrm{W}^2_0}\right) \tag{7.3}$$

where b_A and b_B are shape parameters for the emerging particles. If the b' parameter is independent of energy then it is necessary to set $\alpha'_{\mathbb{P}}$ to zero and there would be no shrinkage. The parameter b' is set at the value 4.0 GeV^{-1} for the elastic processes and 1.6 GeV^{-1} for dissociative processes. The parameters, λ and b' have been adjusted to give results consistent with previously analysed J/ψ data [63].

For the proton dissociation events a further dependence on the effective mass of the proton fragments (M_x) appears. The cross-sectional dependence on this variable is taken to be [66] :

$$\frac{d\sigma_{pdiss}}{dM_x^2} \propto \left(\frac{1}{M_x^2}\right)^{\alpha_{\mathbb{P}}(0)} \tag{7.4}$$

where M_X is the mass of the proton remnant and $\alpha_{\mathbb{P}}(0)$ is Regge trajectory intercept of the pomeron which is found to be approximately 1.08 in accordance with measurements from pp scattering experiments [15].

7.2.2 The LPAIR Generator

The LPAIR Monte Carlo [67] is used to describe the non-resonant background contributing to the invariant mass peak. The generated events are generated according to the QED elastic and inelastic production process for lepton pairs via the two-photon process as is shown in figure 7.6. For this analysis the generator has been set up to model the production of μ^+ μ^- pairs.

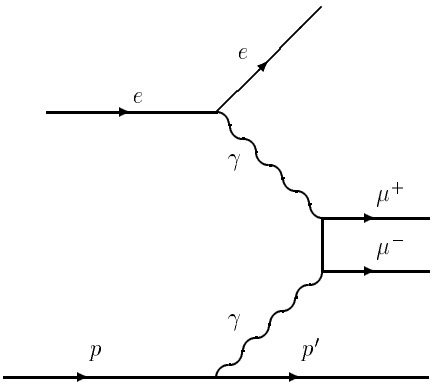

Figure 7.6: *Schematic diagram showing the QED process responsible for the production of* $\mu^+\mu^-$ *pairs.*

7.3 Monte Carlo Simulation

The events produced by the DIFFVM and the LPAIR generator programs provide particles emerging from the event vertex with definite 4-momenta and their decay products. These particle parameters are the input to the second stage of the Monte Carlo production which is the simulation of the detector response carried out by H1SIM [68]. This consists of three separate stages, namely the GEANT, DIGI and TRIGGER steps. GEANT uses a data base which contains all the information concerning the physical properties of the materials that make up the subdetectors of H1. This information allows GEANT to determine an accurate description of the path of the particles traversing through all parts of the H1 detector. The response from the subdetectors is then simulated by the DIGI program which converts the space points provided by GEANT into a set of parameters such as charge which can

be used by the reconstruction code of the various subdetectors. These parameters also suffer smearing in order to achieve the desired resolution of the individual subdetectors.

Individual subtrigger and trigger element responses are simulated[4] using information from the database at the TRIGGER stage. This database contains precise information about the running of the detector during the whole period of data taking. The output from simulation resembles the raw output from the detectors in the form of hits, energy depositions and timing. This simulated event information is then passed through the reconstruction program in the same way that the real data is reconstructed. The simulated Monte Carlo data should accurately resemble the data and hence may be used to determine the acceptances required to calculate the cross-section measurements discussed in the next section.

7.4 The Cross-Section Measurement

The ep cross-section can be calculated using the following relationship :

$$\sigma = \frac{\mathrm{N_{event}}}{\mathcal{L} \times \mathcal{A} \times \mathcal{B}.\mathcal{R}.} \tag{7.5}$$

Where $\mathcal{L}$ is the total integrated luminosity for 1995 which is calculated to be $5.09\,\mathrm{pb}^{-1}$ and $\mathcal{B}.\mathcal{R}.$ is the branching ratio of the decay as quoted in [57]. The determination of the number of $J/\psi \to \mu^+\mu^-$ elastic events ($\mathrm{N_{event}}$) and the acceptance ($\mathcal{A}$) are described in the following sections.

7.4.1 Determination of the Number of Elastic Events

In order to determine this quantity the background contributions due to the QED production of $\mu^+\mu^-$ pairs and events where the proton has dissociated must be determined since,

$$\mathrm{N_{event}} = \mathrm{N_{recon}} - (\mathrm{N_{lpair}} + \mathrm{N_{pdiss}}) \tag{7.6}$$

[4]Prescale factors are not simulated.

where the quantity N_{recon} is the total number of reconstructed data events contributing to the invariant mass elastic signal which have passed the elastic event selection described in section 7.1. The backgrounds have been dealt with separately as follows.

Removal of Non-Resonant Background (N_{lpair})

The contribution due to non-resonant background is calculated using the LPAIR Monte Carlo for the QED production of $\mu^+\mu^-$ pairs. The LPAIR Monte Carlo generator has been described in section 7.2.2. The shape of the background dimuon mass distribution agrees with that of the data. The magnitude of the background has been estimated by studying the central region where both muons lie in the angular range $\theta > 20°$ and $30\,\text{GeV} < W_{\gamma p} < 150\,\text{GeV}$. A similar event selection to that described in section 7.1 was made to select events containing a well measured $\mu^+\mu^-$ pair linked to good CTD tracks and where no other activity was detected in the detector. The same event selection was applied to the LPAIR Monte Carlo sample containing a combination of elastic and inelastic events[5]. Figure 7.7 shows the invariant mass peaks for the different event samples. Plot (a) shows the invariant mass for the central region where the shaded histogram represents the data and the points represent the normalised LPAIR Monte Carlo. The same normalisation factor calculated to be 0.88 ± 0.10 has been applied to the forward region. The plots (b) and (c) show the invariant mass distributions for the data for the one forward going muon sample and the two forward going muons sample respectively. It can be seen that the renormalised Monte Carlo appears to agree well with the background seen for the data for both event types.

[5]The ratio of elastic to inelastic events ($\approx$ 3:1) was estimated using the QED calculated total cross-section for each Monte Carlo sample

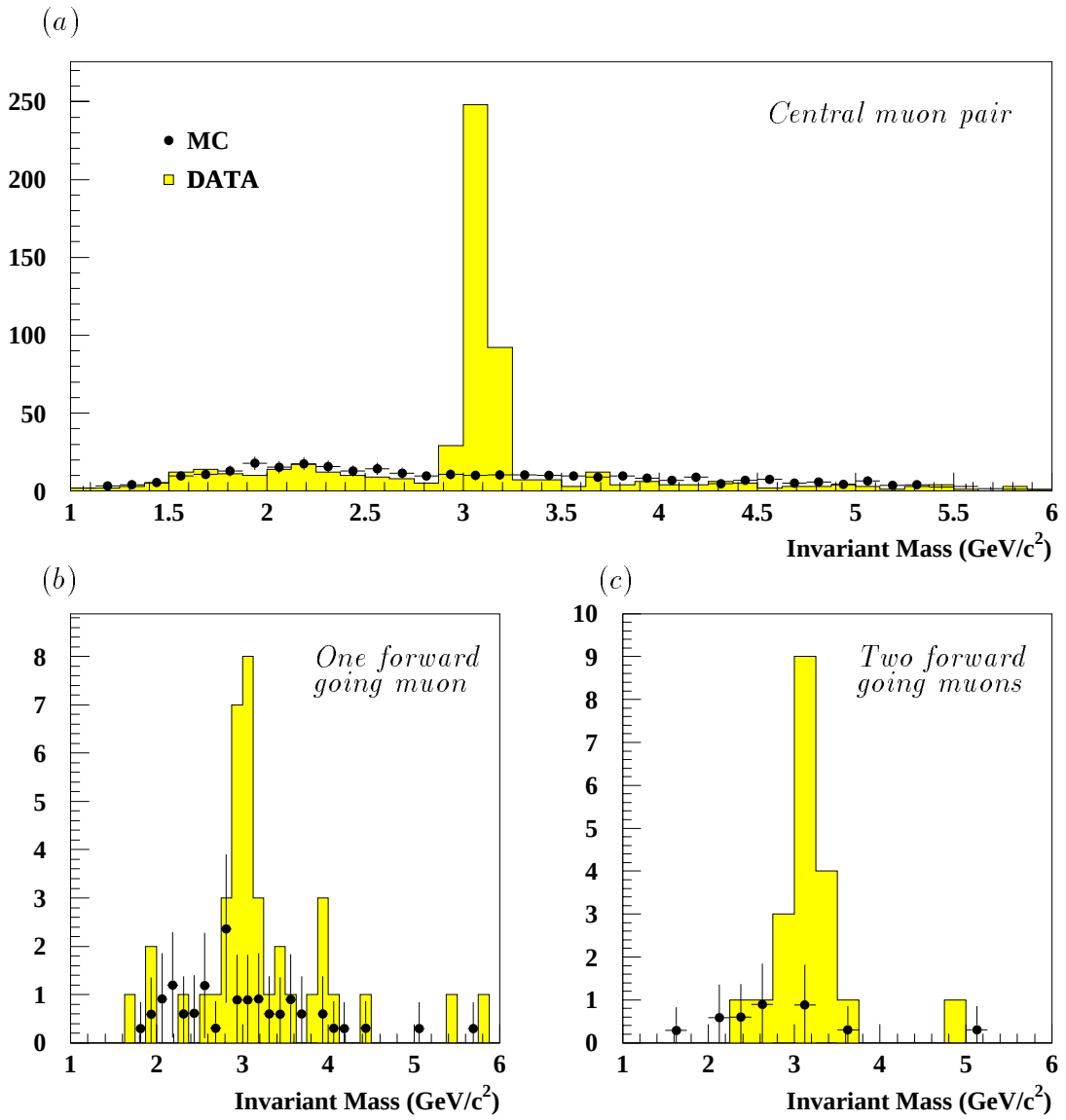

Figure 7.7: *Figure (a) is the invariant mass peak for central tracks. Figures (b) and (c) show the invariant mass peaks for one forward going muon and two forward going muons respectively. The renormalised LPAIR Monte Carlo is show as the closed points and the data is shown as the solid histogram.*

Sample	One forward going muon	Two Forward going muons
N_{recon}	9.0 ± 3.0	17.0 ± 4.1
N_{lpair}	2.1 ± 0.8	5.3 ± 1.3
N_{pdiss}	0.8 ± 0.1	2.7 ± 0.3
N_{event}	6.2 ± 3.1	9.0 ± 4.4

Table 7.3: *The values of the backgrounds contributing to the elastic samples for both event types.*

Removal of Proton Dissociation Background (N_{pdiss})

In order to calculate the number of proton dissociation events that are contaminating the elastic sample the following expression must be determined :

$$N_{pdiss} = \sigma(\gamma p \rightarrow J/\psi X) \times \mathcal{L} \times \mathcal{A} \times \mathcal{B}.\mathcal{R}. \tag{7.7}$$

The variables $\mathcal{L}$ and $\mathcal{B}.\mathcal{R}.$ have already been defined for equation 7.5 and will not be discussed here. The cross-section for proton dissociative events, $\sigma(\gamma p \rightarrow J/\psi X)$, has been estimated using the published measurements taken in the central region of H1 [69] ($\theta > 20^{\circ}$ for both muons) and which are shown in figure 7.8. A fit to the cross-section indicating the dependence on $W_{\gamma p}$ for proton-dissociation is shown as the solid line. This fit has been extrapolated to lower $W_{\gamma p}$ values and hence the cross-sections, at the $W_{\gamma p}$ values 23.5 GeV and 32.5 GeV are estimated to be 21.5 ± 8.3 nb and 15.2 ± 5.3 nb respectively.

The acceptance for detecting and reconstructing the events (N_{pdiss}) has been determined from the DIFFVM proton dissociation Monte Carlo. It is defined as the total number of reconstructed proton dissociation events passing the elastic event cuts divided by the total number of generated events in the appropriate kinematic range. The acceptance is calculated to be 0.8 % for one forward going muon and 0.5 % for two forward going muons.

The background contributions that have been described have been summarised in table 7.3.

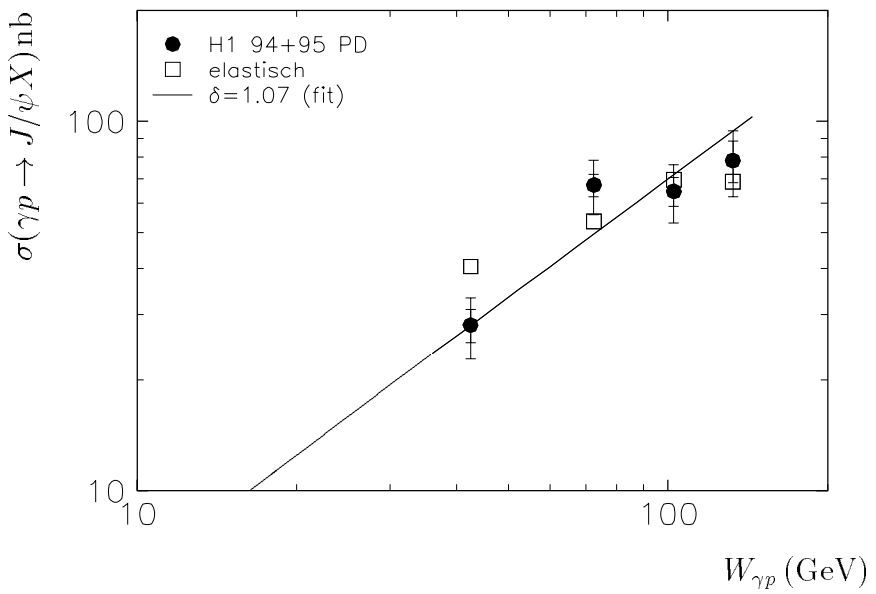

Figure 7.8: *The cross-sections $\sigma(\gamma p \to J/\psi X)$ measured at HERA for combined 1994 and 1995 data are given by the closed points. The inner error bar represent the statistical error and the outer error bar represents the systematic error. A straight line fit has been made to the points of the form $W_{\gamma p}^{\delta}$ where $\delta = 1.07 \pm 0.11$. The open square points are the corresponding elastic cross-sections, $\sigma(\gamma p \to J/\psi p)$, shown with no associated errors.*

7.4.2 The Acceptance ($\mathcal{A}$)

The acceptance for detecting and reconstructing the events is calculated using Monte Carlo and is defined as :

$$\mathcal{A} = \left(\frac{\mathrm{N_{recon}}}{\mathrm{N_{gen}}} \right) \tag{7.8}$$

The generated events ($\mathrm{N_{gen}}$) are only generated in the appropriate kinematic range. The reconstructed events ($\mathrm{N_{recon}}$) are those which pass all the elastic event selection cuts. Therefore, the acceptance includes the trigger efficiencies, the geometric detector acceptance and the acceptance of the event selection. If the Monte Carlo is used to calculate the acceptance then it must represent the data accurately. Figures 7.9 and 7.10 display data and Monte Carlo distributions where the Monte Carlo has been normalized to the number of events seen in data. These distributions show that the Monte Carlo describes the data satisfactorily. Further studies have been

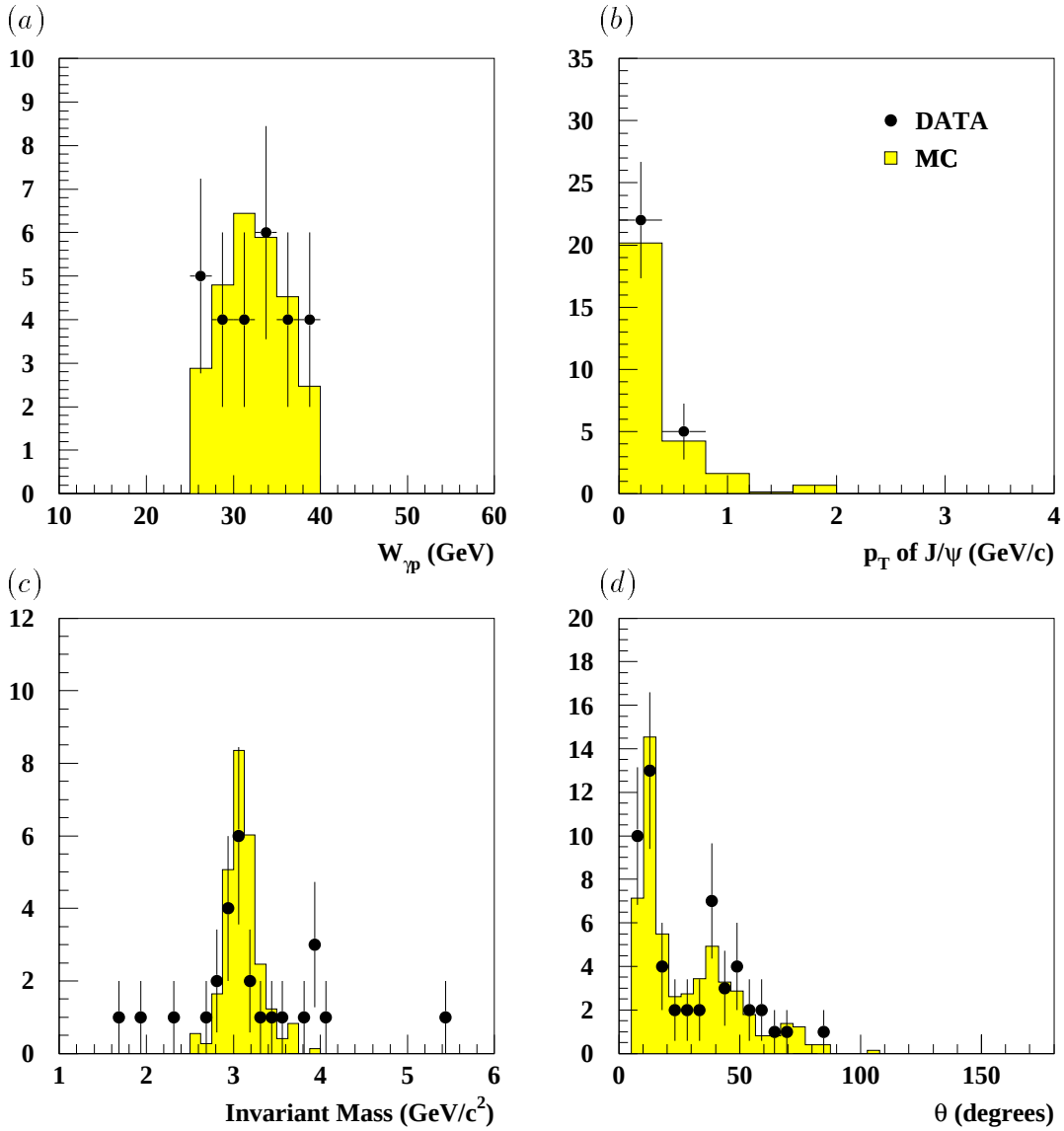

Figure 7.9: *Comparison between Monte Carlo and data for the one forward going muon sample. The plots show: (a) $W_{\gamma p}$, (b) the p_T of the J/ψ meson, (c) the invariant mass reconstructed from the muon pair and (d) the θ of the muons. The data is displayed as the solid histogram and the Monte Carlo, which has been normalised to the data is shown as the solid points.*

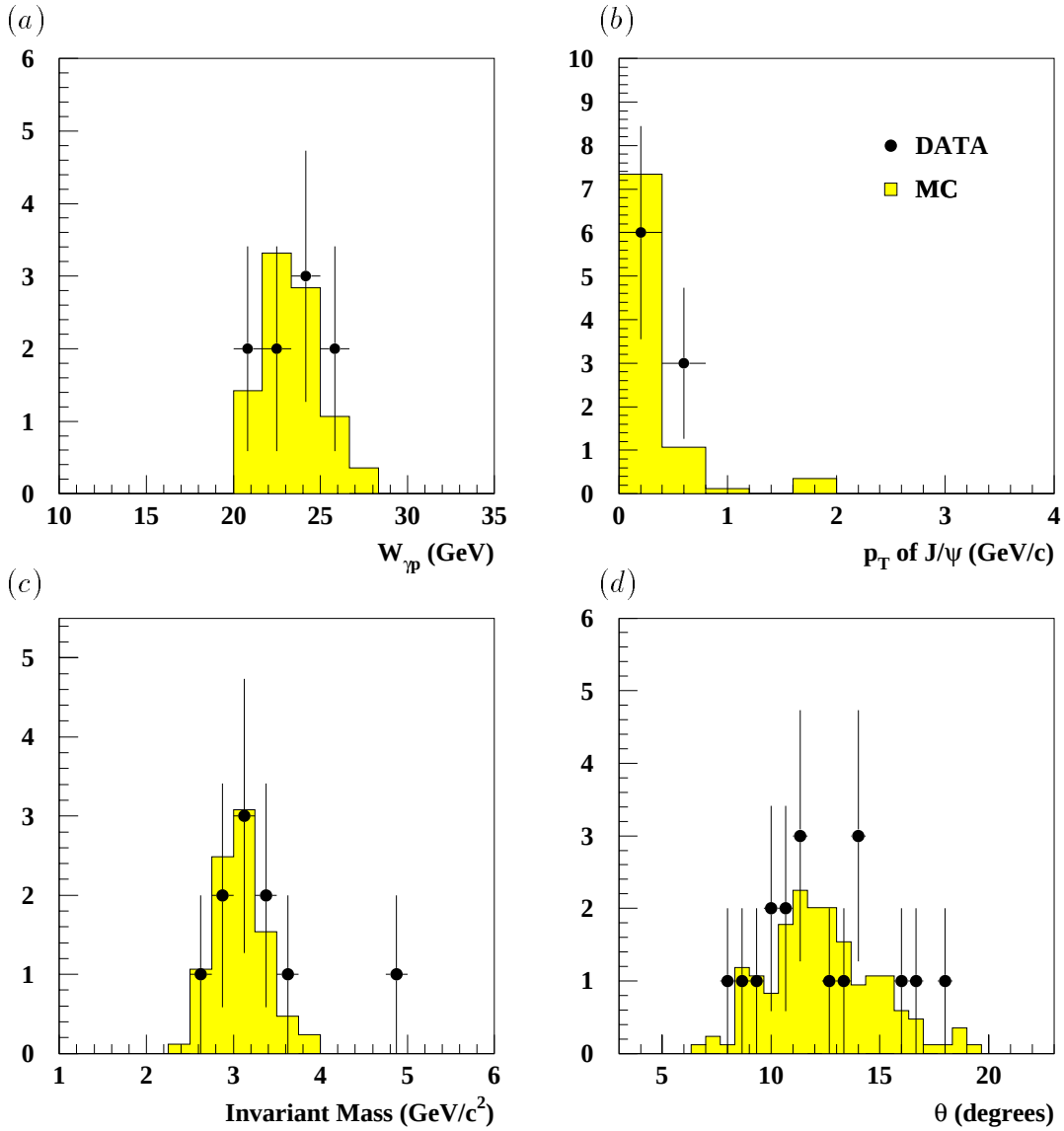

Figure 7.10: *Comparison between Monte Carlo and data for the two forward going muons sample. The plots show: (a) $W_{\gamma p}$, (b) the p_T of the J/ψ meson, (c) the invariant mass reconstructed from the muon pair and (d) the θ of the muons. The data is displayed as the solid histogram and the Monte Carlo, which has been normalised to the data is shown as the solid points.*

Acceptance (%)	One forward going muon	Two Forward going muons
Geometric cuts	61.7	53.4
Analysis cuts	29.3	18.4
Subtrigger selection	11.6	15.6
Total Acceptance ($\mathcal{A}$)	2.09	1.55

Table 7.4: *Table giving the values of the acceptance for triggering and reconstructing the elastic J/ψ events for both event samples.*

carried out to check the consistency of the Monte Carlo with the data. Detector and trigger efficiencies for the FMD, FMT, iron and relevant inner-track triggers were discussed in chapter 6. Using the elastic DIFFVM Monte Carlo the overall acceptance was calculated to be 2.09 % for the one forward muon sample and 1.55 % for the two forward muons sample. This acceptance has been broken down into the geometric and subtrigger acceptance and the acceptance resulting from the analysis cuts in table 7.4.

7.5 Systematic Errors

There is a systematic uncertainty on each of the measurement that contributes to the final calculation of the cross-section measurement. The systematic errors for the two event samples are summarised in table 7.6. The systematic uncertainties associated with the contribution from background sources are as follows:

- In section 6.3.1 is was observed that there was a discrepancy between the Monte Carlo and data track reconstruction efficiency determined for the FTD (5 %) and the CTD (3 %). Following the observation of dead regions in phi (illustrated in figure 5.15) the systematic error assigned to the CTD track reconstruction has been increased to 6 %. The difference between the efficiency measured using the Monte Carlo and the the efficiency measured by the data will be taken as the systematic error on the uncertainty of track reconstruction

Event Category	Data	Monte Carlo
FMD && FMT	0.51 ± 0.05	0.89 ± 0.02
FMD && !FMT	0.25 ± 0.05	0.07 ± 0.02
!FMD && FMT	0.07 ± 0.03	0.03 ± 0.01
!FMD && !FMT	0.17 ± 0.04	0.01 ± 0.01

Table 7.5: *Table listing the four possible event categories described by the FMD and the FMT and the efficiency for obtaining the event category.*

for the FTD.

- A study of the muon track and trigger efficiencies for the FMD and the instrumented iron used for this analysis was presented in sections 6.1 and 6.2. A large discrepancy between the data and Monte Carlo was observed for the efficiency of the FMD track reconstruction and the FMT trigger ($FwdMu\_Val\_Any$) efficiency. There was also some discrepancy observed between the data and Monte Carlo for the efficiency of the forward iron inner end-cap track reconstruction and trigger (Mu_FIEC) efficiency. The Monte Carlo efficiency was corrected to the level obtained from the data. In each case the correlation between the trigger and detector must be taken into account. The events can be categorised into four possible event types depending on whether a track has been reconstructed by the FMD and whether the FMT has triggered the event. The four different categories are listed in table 7.5 along with the efficiencies of obtaining the event category as determined by Monte Carlo and data. By comparing these values the Monte Carlo events may be reweighted to correct the efficiency including the correlation between the FMD and the FMT.

- Muon identification by the LAr is only relevant for the one forward going muon sample. Studies have shown [70] that discrepancies are observed between the efficiency measured for Monte Carlo and data. The Monte Carlo efficiency was corrected to the level obtained from the data.

- A study of the efficiencies of the inner-track trigger elements used for this analysis was presented in section 6.3. The resulting uncertainties in the acceptance for each trigger element are shown in table 6.1. A discrepancy between the data and Monte Carlo was observed for the efficiency of the z-vertex track trigger elements for the one forward going muon event sample. The systematic error associated with these measurements was taken as the difference between the efficiency observed for the data and the Monte Carlo.

- The removal of the proton dissociation background has been described in section 7.4.1. It requires extrapolating the fit made to the cross-section measurements in the central region (figure 7.8). The estimated cross-sections have an associated error which have been determined from the fit parameter error ($\delta = 1.07 \pm 0.11$). The systematic error resulting from the uncertainty of these estimated cross-sections are 11.3 % for the one forward muon sample and 5.4 % for the two forward muon sample.

- A further systematic error results from the elastic cuts that are applied to the quasi-elastic event sample described in section 7.1. These cuts were varied and the cross-section changes by 11.5 % for the one forward muon sample and 9.1 % for the two forward muons sample. These are taken as the systematic errors to obtain a pure sample of elastic events.

- When calculating the contribution due to the non-resonant background using the LPAIR Monte Carlo it has been assumed that the normalisation factor determined from the central region is independent of $W_{\gamma p}$. Studies were carried out for differing ranges in $W_{\gamma p}$ and it was found that the normalisation factor remained constant to within 20% of the mean value. Therefore, the calculated factor for 30 GeV$< W_{\gamma p} <$ 150 GeV has been extrapolated to lower $W_{\gamma p}$ ranges. The cross-section changes by 7.6 % for the one forward muon sample and 4.3 % for the two forward muons sample if the normalisation factor is changed by 20 %. These are taken as the systematic error on calculating the normalisation factor.

- A systematic error arises from the uncertainty of the total integrated luminosity measurement made for 1995 data. The error associated with the measurement was calculated to be 1.1 % [40].

- The branching ratio corresponding to $J/\psi \rightarrow \mu^+\mu^-$ has a 4.2 % error associated with the measured value, 5.97 % [57] .

- A systematic error arises from the Monte Carlo statistics used when calculating the acceptance. The Monte Carlo was generated so that a sufficient number of events (comparable to the luminosity of data studied) was available. The systematic error arising from the Monte Carlo was calculated to be 4.1 % for the one forward muon sample and 7.9 % for the two forward muon sample.

- When calculating the photoproduction cross-sections an additional error due to the uncertainties of the photon flux calculation must be included. This error was estimated by varying the value of λ, the $W_{\gamma p}$ dependence of the cross-section, from 0.15 to 0.225. The systematic error arising from the flux factor was calculated to be 0.5 % for the one forward muon sample and 0.2 % for the two forward muon sample.

7.6 Results

The ep cross-section can calculated by equation 7.5 where the values of $N_{\rm event}$ and $\mathcal{A}$ are listed in table 7.7. The ep cross-section for elastic J/ψ production for the channel in which the J/ψ decays to muons in the kinematic region defined by 25 GeV$<$ $W_{\gamma p}$ $<$40 GeV and $Q^2 < 1.2\,\mathrm{GeV}^2$ was calculated to be :

$$\sigma(ep \rightarrow J/\psi p) = 1.51 \pm 0.76\,(stat) \pm 0.34\,(syst)\,nb \tag{7.9}$$

and for the kinematic region defined by 20 GeV$<$ $W_{\gamma p}$ $<$27 GeV and $Q^2 < 1.2\,\mathrm{GeV}^2$ was calculated to be :

$$\sigma(ep \rightarrow J/\psi p) = 1.34 \pm 0.66\,(stat) \pm 0.32\,(syst)\,nb. \tag{7.10}$$

Systematic uncertainty (%)	Data Sample	
	One Forward Muon	Two Forward Muons
Track reconstruction efficiency	7.8	9.8
FMD track reconstruction and FMT trigger efficiency	8.1	16.2
Forward iron inner end-cap track reconstruction and trigger efficiency	2.3	3.3
Calorimeter muon identification	2.3	-
Inner trigger efficiency	1.5	0.9
Proton dissociation background (N_{pdiss})	11.3	5.4
Elastic Cuts	11.5	9.1
Lpair background normalisation (N_{lpair})	7.6	4.2
Monte Carlo statistics	4.1	7.9
Photon Flux ($\Phi_{\gamma/e}$)	0.5	0.2
Luminosity	1.1	1.1
$B.R.(J/\psi \rightarrow \mu^+\mu^-)$	4.2	4.2
Total Systematic Error	22.2	24.1

Table 7.6: *Systematic errors for the two data samples.*

As described in section 1.3, the ep cross-sections are related to the photoproduction cross-sections at $Q^2 = 0$ by equation 1.14. From this it was derived that the ep cross-section, $\sigma(ep \to J/\psi X)$, and the γp cross-section, $\sigma(\gamma p \to J/\psi X)$, are related by the following expression :

$$\sigma(ep \to J/\psi X) = \sigma(\gamma p \to J/\psi X)\Phi_{\gamma/e} \tag{7.11}$$

where the $\Phi_{\gamma/e}$ is the flux factor which was defined by equation 1.18. The flux factors were calculated over the different ranges of $W_{\gamma p}$ and Q^2 corresponding to the two event samples and have been listed in table 7.7. The photoproduction cross-section at $Q^2 = 0$ and $W_{\gamma p} = 32.5\,\mathrm{GeV}$ was calculated to be :

$$\sigma(\gamma p \to J/\psi p) = 30.9 \pm 10.5\,(stat) \pm 6.9\,(syst)\,nb \tag{7.12}$$

and the photoproduction cross-section at $Q^2 = 0$ and $W_{\gamma p} = 23.5\,\mathrm{GeV}$ was calculated to be :

$$\sigma(\gamma p \to J/\psi p) = 39.2 \pm 16.6\,(stat) \pm 9.4\,(syst)\,nb. \tag{7.13}$$

Wγp (GeV)	$20 < W_{\gamma p} < 27$	$25 < W_{\gamma p} < 40$
N_{event}	6.2	9.0
Acceptance (%)	1.5	2.0
Flux Factor ($\Phi_{\gamma/e}$)	0.0336	0.0489
$\sigma(ep \to J/\psi p)$ (nb)	1.34 $\pm$0.66 $\pm$0.32	1.51 $\pm$0.76 $\pm$0.34
$\sigma(\gamma p \to J/\psi p)$ (nb)	39.2 $\pm$19.2 $\pm$9.4	30.9 $\pm$15.5 $\pm$6.9

Table 7.7: *A summary of the elastic J/ψ photoproduction cross-sections for the two event samples studied in this analysis. The ranges over $W_{\gamma/e}$ and Q^2 over which the cross-sections are defined are shown. The photon flux ($\Phi_{\gamma p}$) values, which are integrated over $W_{\gamma/e}$ and Q^2, are shown and are used to convert σ_{ep} to $\sigma_{\gamma p}$. The first error shown is the statistical error and the second is the systematic error.*

7.6.1 Conclusions

A signal has been observed for the decay of the elastically produced J/ψ mesons for the $W_{\gamma p}$ ranges 20 GeV$<$ $W_{\gamma p}$ $<$27 GeV and 25 GeV$<$ $W_{\gamma p}$ $<$40 GeV. These photoproduction cross-sections have been plotted as a function of $W_{\gamma p}$ in figure 7.11. The previous published results taken at HERA by H1 [63] and ZEUS [64] and results from a sample of fixed target experiments, E516 [71] and E687 [72] have also been included. The fit given by the solid line has been made to the data points and and gives the relationship :

$$\sigma(\gamma p \rightarrow J/\psi p) \sim W_{\gamma p}^{0.78 \pm 0.16}. \tag{7.14}$$

This corresponds to a measured value of $\lambda = 0.19 \pm 0.08$. The value of b' that has been used for the fit was taken to be 4 GeV^{-1} [63]. The dashed line in figure 7.11 shows the relationship :

$$\sigma(\gamma p \rightarrow J/\psi p) \sim W_{\gamma p}^{0.32}. \tag{7.15}$$

This describes the soft-pomeron exchange which would require $\lambda = 0.08$. A strong physics statement about the cross-sectional dependence on $W_{\gamma p}$ from the results calculated here cannot be made because the statistical error associated with the measurements is large. However it is clear that the overall results do not support soft pomeron exchange and favour the exchange of a 'hard' object such as that predicted by the 'Ryskin Model' [25, 26] (see section 1.5.6)

In making this measurement, a new kinematic range had to be understood in detail. In doing so many problems have been encountered which have been resolved and will help to make an important contribution to future analysis of data detected in the forward region of H1. The final cross-section measurement is a good indication of the validity of the work that has gone into achieving this result. Increased luminosity[6] will give a measurement that will not be dominated by statistical error and may help to confirm the cross-sections dependence on $W_{\gamma p}$. It will also increase the statistics needed to make more accurate measurements of the detector and trigger

[6]The total integrated luminosity collected in 1996 and 1997 was approximately 9 pb^{-1} and 27 pb^{-1} respectively.

efficiencies in the forward direction.

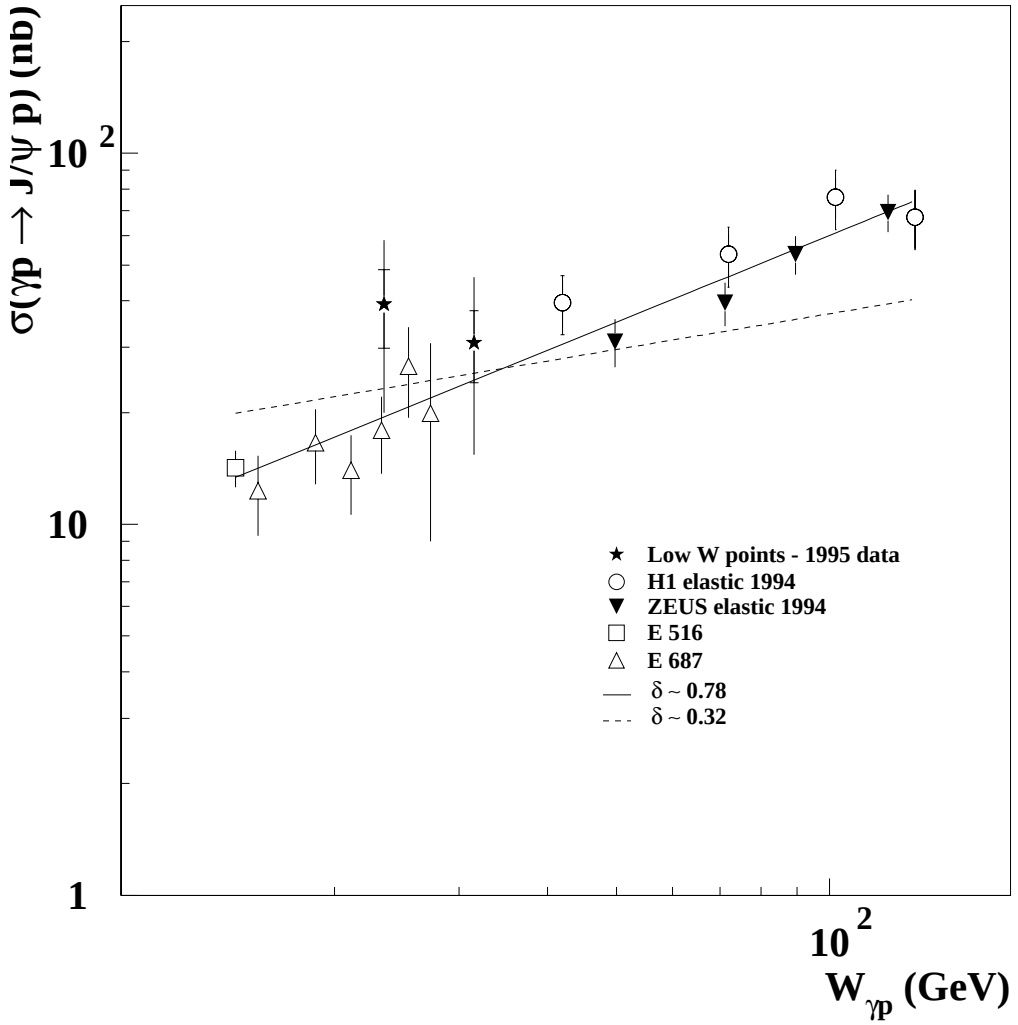

Figure 7.11: *The elastic J/ψ photoproduction cross-section shown as a function of $W_{\gamma p}$. Results from previous experiments have also been included on the plot. The closed circles are the published 1994 data points measured at H1 [63] and the closed triangles are the published 1994 data points measured at Zeus [64]. The prediction which described the nature of the exchange object as a soft pomeron ($\delta = 0.32$) has been plotted as the dashed line. The fit to the data points shown as the solid line gives a value of $\delta = 0.78$ which is consistent with the hard pomeron prediction ($\delta \approx 0.8$).*

Bibliography

[1] R.G. Roberts, *The strucure of the proton*, Cambridge University Press, 1990.

[2] H1 collab., I.Abt et al., Phys. Lett. **B324** (1994) 241.

[3] H1 collab., I.Abt et al., Phys. Lett. **B299** (1993) 374.

[4] H1 collab., C.Adloff et al., Z. Phys. **C74** (1997) 191.

[5] J.D.Bjorken, Phys. Rev. **163** (1967) 1767.

[6] B.R.Martin and G.Shaw, *Particle Physics*, John Wiley & Sons Inc. (1992).

[7] F.Halzen and A.Martin, *Quarks and Leptons: An Introductory Course in Modern Particle Physics*, John Wiley & Sons Inc. (1984).

[8] A.Blondel and F.Jacquet, *Proceed. of the Study for an ep Facility for Europe*, ed. U.Amaldi, DESY 79/48 (1979) 391.

[9] C.F.Weizacker, Z. Phys. **88** (1934) 612;
E.J.Williams, Phys. Rev. **45** (1934) 729.

[10] V.M.Budnev et al., Phys. Rep. **C15** (1975) 181.

[11] ZEUS Collab., M. Derrick et al., Phys. Lett. **B297** (1992) 404.

[12] H1 Collab., T. Ahmed et al., Phys. Lett. **B297** (1992) 205.

[13] K. Goulianos, Phys. Rep. **C101** (1983) 169, (and references therein).

[14] T.Regge, Nuovo Cim. **14** (1959) 951;
T.Regge, Nuovo Cim. **18** (1960) 947.

[15] A.Donnachie and P.V.Landshoff, Nucl. Phys. **B244** (1984) 322.

[16] H1 Collab., C. Adloff et al., Z. Phys. **C74** (1997) 221.

[17] J.J Aubert et al., Phys. Rev. Lett. **33** (1974) 1404.

[18] J.E Augustin et al., Phys. Rev. Lett. **33** (1974) 1406.

[19] J.J.Sakurai, Ann. Phys. **11** (1960) 1;
M.Gell-Mann and F.Zachariasen, Phys. Rev. **124** (1961) 953.

[20] G.Wolf and P.Soding, in *Eletromagnetic Interactions of Hadrons*;
Vol.2,p.1; Eds. Donnachie and Shaw, 1978.

[21] H1 Collab., S.Aid et al., Phys. Lett. **B358** (1995) 412.

[22] T.Bauer et al., Rev. Mod. Phys. **50** (1978) 261.

[23] J.J.Sakurai, D.Schildknecht, Phys. Lett. **B40** (1972) 121.

[24] J.Nemchik et al., Phys. Lett. **B374** (1996) 199.

[25] M.G.Ryskin, Z. Phys. **C57** 89.

[26] M.G.Ryskin et al., Z. Phys. **C76** (1997) 231-239.

[27] A.Levy, DESY report 95-204 (hep-ex/9511006), November 1995.

[28] A.D.Martin, W.J.Stirling and R.G.Roberts, Phys.Lett. **B354** (1995) 155.

[29] M.Gluck, E.Reya and A.Vogt, Phys.Rev. **D45** (1992) 3986.

[30] H1 collab., I.Abt et al., *The H1 detector at HERA*, (updated version) DESY 96-01 (1996), to be submitted to Nucl. Instr. and Meth.

[31] Nucl. Instr. and Meth. 196:293-297, 1982.

[32] J.Burger et al., Nucl Instr. and Meth. **A279** (1989) 217.

[33] B. Andrieu et al., Nucl. Instr. and Meth. **A336** (1993) 460.

[34] H1 collab., T. Nicholls et al., DESY Red Report 95-165 (1995)

[35] H1 collab., R.-D Appuhn et al., DESY Red Report 096-013 (1996)

[36] M. Ruffer *Implementierung des Silizium-instrumentierten PLUG-Kalorimeters in den H1-Detektor*, Ph.D. Thesis, The University of Hamburg (1992).

[37] H. Bergstein et al., *Beam calibration of the H1 tail catcher at CERN*, H1 report 10/91-197, DESY, Hamburg (1991).

[38] I.Kenyon et al., *The H1 Forward Muon Spectrometer*, Nucl. Instr. and Meth. **A340** (1994) 304-308.

[39] The H1 Collab., Paper pa17-025, 28th International Conference on High Energy Physics, Warsaw, Poland, July 1996.

[40] H1 Collab., *Luminosity Measurement in the H1 experiment at HERA*, submitted to XXVIII ICHEP, Warsaw, 1996.

[41] F.Sefkow et al., *The First Level Trigger of H1*, H1 report 11/94-407, DESY, Hamburg (1994).

[42] S.Burke et al., *Track Finding and Fitting in the H1 Forward Track Detector*, Nucl. Instr. and Meth. A373:227-260,1996.

[43] J.P. Sutton, Private Communication.

[44] L.West, *How to use the Reconstruction Code MTREC*, software note 48-06/94 (1994).

[45] T.Ahmed et al., NIM. **A364** (1995) 456.

[46] C.Niebuhr, Private Communication.

[47] L.West, internal note, *How to use the Heavy Flavour Working Group Track, Muon and Electron Selection Code*, (1997).

[48] B.Naroska, S.Schiek and G.Schmidt, *Lepton Identification in the H1 Detector at Low Momenta*, (H1-05/97-518)

[49] K.L.Hewitt, *The Detection and Triggering of Forward Muons using the H1 Detector*, M.Phil, The University of Birmingham (1996).

[50] G.D. Patel, Private Communication.

[51] J.V.Morris, Private Communication.

[52] C.D.Hilton, *Forward Muon Detection in H1 and Hadronic Energy Flow in Deep Inelastic Scattering*, Ph.D. Thesis, The University of Manchester (1993).

[53] W. Buchmüller and G. Ingelman, *The Lund Monte Carlo for Deep Inelastic Lepton-Nucleon Scattering*, Proceed. of the Hamburg Workshop, Volume 3, October 1991. Hamburg (DESY) 1366.

[54] W. Buchmüller and G. Ingelman, *Django: the interface for the event generators HERACLES and LEPTO*, Proceed. of the Hamburg Workshop, Volume 3, October 1991. Hamburg (DESY) 1419.

[55] W. Buchmüller and G. Ingelman, *A Monte Carlo Generator for Heavy Flavour Events in ep Collisions*, Proceed. of the Hamburg Workshop, Volume 3, October 1991. Hamburg (DESY) 1346.

[56] S.Burke, Private Communication.

[57] Particle Data Book.

[58] L.R.West, Private Communication.

[59] J.P.Sutton, Private Communication.

[60] W. Erdmann, *Untersuchung der Photoproduktion von D^* Mesonen am ep-Speichering HERA*, Doctoral Thesis, Institut f. Teilchenphysik, ETH Zürich (1996).

[61] U.Langenegger, Private Communication.

[62] V.L Hudgson, *Measurement of the Cross Section for the Quasi-elastic Photoproduction of $\psi(2S)$ at HERA.*, Ph.D. Thesis, The University of Birmingham (1997).

[63] H1 Collab, S. Aid et al., Nucl. Phys. **B472** (1996) 3.

[64] Zeus Collab, J.Breitweg et al., Z. Phys. **C75** (1997) 215-228.

[65] B. List, *Diffractive J/ψ-Produktion in Elektron-Proton-Stoessen am Speicherring HERA*. Diploma Thesis, Tech. The University of Berlin, 1993.

[66] CHLM Collaboration, Nucl. Phys. **B108** (1976) 1.

[67] W. Buchmüller and G. Ingelman, *A Generator for Lepton Pair Production*, Proceed. of the Hamburg Workshop, Volume 3, October 1991. Hamburg (DESY) 1478.

[68] S.Egli et al.,H1 collab., H1SIM manual,

[69] G.Schmidt, *Untersuchung der diffraktiven Photoproduktion von J/ψ-Mesonen im H1-Detektor bei HERA*. The University of Hamburg (1996).

[70] M.Anderson, Private Communication.

[71] B.H. Denby et al., Phys. Rev. Lett., **52** (1984) 795.

[72] P.L. Frabetti et al., Phys. Lett., **B316** (1993) 197.